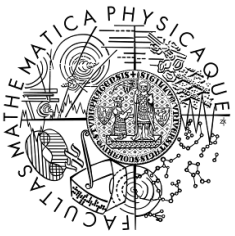

FACULTY
OF MATHEMATICS
AND PHYSICS
Charles University

DOCTORAL THESIS

Monika Krupová

Theory and Applications of Optical Activity of Biomolecules

Faculty of Mathematics and Physics
Charles University
and
Institute of Organic Chemistry and Biochemistry
Academy of Sciences of the Czech Republic

Supervisor of the doctoral thesis: Prof. RNDr. Petr Bouř, DSc.
Consultant: Dr. Valery Andrushchenko

Study program: Physics
Specialization: Biophysics, Chemical and Macromolecular Physics

Prague 2021

I declare that I carried out this doctoral thesis independently, and only with the cited sources, literature and other professional sources.

I understand that my work relates to the rights and obligations under the Act No. 121/2000 Coll., the Copyright Act, as amended, in particular the fact that the Charles University has the right to conclude a license agreement on the use of this work as a school work pursuant to Section 60 paragraph 1 of the Copyright Act.

In Prague 10th April 2021

Acknowledgements

First and foremost, I would like to express my deep and sincere gratitude to my supervisor, prof. RNDr. Petr Bouř, DSc. for encouragement and support throughout the course of my work. His patience, endless effort and help motivated me to work in this area and I am very grateful for the opportunity to work and learn in such a stimulating environment.

Next, I would like to thank Dr. Valery Andrushchenko, who helped me mainly with the experimental aspects of chiroptical spectroscopy. Throughout the years, Valery has become not only my teacher, but also my friend – something I am very grateful for.

Next, I would like to thank Josef Kapitán (Palacký University, Olomouc) for letting us use his custom-built ROA instrument in Olomouc and for a lot of advice concerning optical phenomena. I also thank Romana Hadravová (IOCB) for electron microscopy imaging and Blanka Klepetářová (IOCB) for X-ray diffraction studies. I thank Jakub Chalupský for advanced lanthanide calculations and discussions about the secrets of lanthanide electronic structure.

I would also like to thank other members of Molecular spectroscopy laboratory at IOCB. They all have been a great inspiration and they made my work very enjoyable. Notably, I thank Jana Hudecová for help in navigating „MatFyz waters“, Jirka Kessler for all computer and calculations-related advice, and Andrii Kurochka for all of those times he took me for an excursion into his molecular biology kingdom. I thank Jarek Šebestík for a lot of advice on organic chemistry and Radek Pelc (Stentor Institute) for help with microscopes. And mainly, I thank Mohamed, Věra, Greg and Petr N. for the coffee breaks and lunches and for becoming great friends to me.

Last but not least, my personal thanks belongs to my family for their endless support throughout my studies. A special thanks goes to my sister Zuzana, who always supported my goals and dreams and made my studies in Prague possible. I also want to thank Sima, a great friend who made my life in Prague much more fun.

Title: Theory and Applications of Optical Activity of Biomolecules

Author: Monika Krupová

Supervisor: prof. RNDr. Petr Bouř, DSc.

Institutions: Faculty of Mathematics and Physics, Charles University, and Institute of Organic Chemistry and Biochemistry, Academy of Sciences of the Czech Republic

Abstract:

This thesis describes how we used several chiroptical spectroscopic methods to study chiral molecules: vibrational circular dichroism (VCD), circularly polarized luminescence (CPL) and magnetic circular dichroism (MCD). VCD and induced lanthanide CPL were used to study the structure of amyloid protein fibrils. We found out that VCD is very sensitive to their structure and supramolecular chirality. It could be used to distinguish between various polymorphic fibrils. On the other hand, induced lanthanide CPL provided information on the local structure. VCD was also used to study the hydration polymorphism of nucleoside crystals. Due to the crystal packing, the VCD signal was strong and specific for different types of crystals. Finally, electronic structure of hydrated Ln^{3+} ions was studied by MCD. Molecular dynamics simulations together with crystal field theory (CFT) and multistate complete active space calculations with second order perturbation correction (MS-CASPT2) were used to interpret the spectra. CFT provided better electronic transition energies, while MS-CASPT2 method gave better spectral shapes.

Keywords: optical activity, chiroptical spectroscopy, vibrational circular dichroism, circularly polarized luminescence, lanthanides, amyloid fibrils, proteins, magnetic circular dichroism, quantum-chemical calculations

Název: Teorie a aplikace optické aktivity biomolekul

Autor: Monika Krupová

Vedoucí: prof. RNDr. Petr Bouř, DSc.

Pracoviště: Matematicko-fyzikální fakulta Univerzity Karlovy a Ústav organické chemie a biochemie, Akademie věd České republiky

Abstrakt:

Tato práce popisuje naše aplikace tří metod chiroptické spektroskopie při studiu chirálních molekul: vibračního cirkulárního dichroismu (VCD), cirkulárně polarizované luminiscence (CPL) a magnetického cirkulárního dichroismu (MCD). VCD a indukovanou CPL lanthanoidů jsme použili ke studiu struktury amyloidních fibril vybraných proteinů. Zjistili jsme, že VCD je velmi vhodnou technikou k detekci proteinových fibril a jejich supramolekulární chirality. Je schopná rozlišit i různé polymorfické typy fibril. Na druhou stranu, indukovaná CPL lanthanoidů reflektuje spíše lokální strukturu. VCD jsme použili i ke studiu hydratace a polymorfismu krystalů nukleosidů. Díky uspořádání krystalu jsme naměřili silný VCD signál specifický pro hydratovanou a suchou formu. Poslední část práce je věnována MCD a elektronové struktuře trivalentních Ln^{3+} iontů. Experimentální spektra byla interpretována pomocí kombinace molekulové dynamiky, teorie krystalového pole (CFT) a výpočtů využívajících konfigurační interakci v úplném aktivním prostoru pro více stavů s poruchovou teorii druhého řádu (MS-CASPT2). Bylo zjištěno, že CFT poskytuje lepší shodu s experimentálními energiemi elektronových přechodů, zatímco metoda MS-CASPT2 poskytuje lepší spektrální intenzity.

Klíčová slova: optická aktivita, chiroptická spektroskopie, vibrační cirkulární dichroismus, cirkulárně polarizovaná luminiscence, lanthanoidy, amyloidní fibrily proteinů, magnetický cirkulární dichroismus, kvantově-chemické výpočty

Contents

Preface: The Twists and Turns of Life

The concept of chirality in biological world has puzzled scientists for almost 200 years. In the first half of the 19th century, the "handedness" of crystalline natural quartz was connected to the ability of the material to rotate the plane of polarized light.[1, 2] Later, molecular chirality was discovered by Louis Pasteur in 1848.[3] During his work on tartaric acid, he noticed that there are two types of sodium ammonium tartrate crystals, which are mirror images of each other. He realized that the chirality of crystals originates in the chirality of tartaric acid molecules, and that the non-optically active paratartaric acid is a racemic mixture of two tartaric acid enantiomers. He also proposed that in the living world only one enantiomer of chiral molecules prevails and this biomolecular homochirality is a result of some dissymmetric forces in nature.[4]

Nowadays, we know that the chirality is very common in carbon and coordination chemistry. However, a bias towards one handedness is characteristic only for the living world. Complex molecules making up the cells and bodies of living organisms such as constituents of DNA and proteins or sugars exist only in one enantiomeric form. In contrast, roughly equal numbers of left- and right-handed molecules can be found in the non-biological world. This "lack of mirror symmetry" in life can be encountered also on the cellular and macroscopic levels, e.g. as spiral shells of snails, positions of organs in the human and animal bodies, etc. Also, the chirality is a key concept in molecular recognition. As a lock can be opened only with a specific key, also enzymes can process only one enantiomer of the substrate. The receptors on the cell surface are triggered only by a certain handedness of a signaling molecule, a wrong enantiomer of a drug may be ineffective or even harmful, etc. No wonder this biological homochirality is to this day one of the greatest mysteries of nature.

In mid-1980s, a "breaking the mirror" hypothesis has emerged.[5] It assumed that before life appeared something had to crack the symmetry between the left- and right-handed molecules. The origin of homochirality in life may therefore be found in the prebiotic world before the first self-replicating molecules emerged. The origin of biomolecular homochirality may be connected to "chiral matrices" in the solid phase.

In the solid state, the molecules are densely packed with relatively fixed orientations, therefore their chiral discrimination energy is larger than in the liquid phase. Such solid surfaces could serve as templates for synthetic reactions on primordial Earth.[6] Although some asymmetric autocatalytic reactions have already been identified,[7] explorations into the origin of life and biological homochirality still have a long way to go.[8]

The chirality in biological world does not lie only in the handedness of basic organic molecules such as amino acids or sugars, but is also reflected in three-dimensional structure of larger molecules and molecular aggregates. Various turns, helices, and spirals are common structural motives in nucleic acids, polysaccharides and proteins. Biomolecular condensation also results in ordered chiral structures. In the recent decades, such supramolecular chirality was found to be quite common in biological supramolecular aggregates. In this work, we focused on the interaction of light with chiral matter. Light has an intrinsic handedness, and its chiral forms (right- and left-handed circularly polarized light) have the ability to interact differently with chiral molecules. Such differences can be further linked to electronic or geometric structure through the language of quantum mechanics.

I present three projects in this thesis. The first one uses chiroptical spectroscopic methods to study pathogenic protein aggregates. Crystal structure and supramolecular chirality associated with chiral organization of chromophores in crystals is discussed in the second project. Finally, the electronic structure of Ln^{3+} ions is studied by the means of induced circular dichroism in the static magnetic field.

1. Introduction to Chiroptical Spectroscopy

Chiroptical spectroscopic methods have an important role in absolute configuration determination, and provide an insight into the conformation and structure of larger aggregates and biopolymers. The optical spectroscopy does not provide the atomic resolution of X-ray diffraction, but its advantages lie in the simplicity and flexibility of the experiment and broad applicability to different systems. The advances in computational chemistry have been very important; they made it easier to analyze the spectra and provided additional information on the properties of studied chiral molecular systems.

1.1. Symmetry of Molecules and Optical Activity

Chirality is an important concept in chemistry. A molecule is said to be chiral if it cannot be superimposed to its mirror image by any combination of translations and rotations. This reflects the symmetry – if a molecule has an axis of improper rotation S_n it is not chiral. Improper rotation consists of a rotation by $360°/n$ ($n = 1, 2, 3, ...$) followed by a reflection in a plane perpendicular to the rotation axis. That means that molecules with a centre of inversion ($i = S_2$) or a symmetry plane ($\sigma_h = S_1$) are not chiral.[9]

Chiral molecules exist in two forms called enantiomers. The chirality can be achieved in several ways. In organic chemistry, we often encounter point (or configurational) chirality. The most common source of it is an asymmetric carbon (a carbon atom with sp^3 hybridization and four different substituents).[10] In inorganic chemistry, metal centers of symmetric non-planar complexes can serve as a source of point chirality as well.[11] **Figure 1** illustrates the concept of point chirality. Chirality can be also linked to spacial arrangement of polymers and aggregates. For example, any helical structure is chiral. In polymers and biological materials, this type of conformational chirality is encountered quite often, e.g. in nucleic acids and proteins. Also, aggregation and crystallization of chiral and sometimes even achiral molecules can lead to supramolecular chirality.

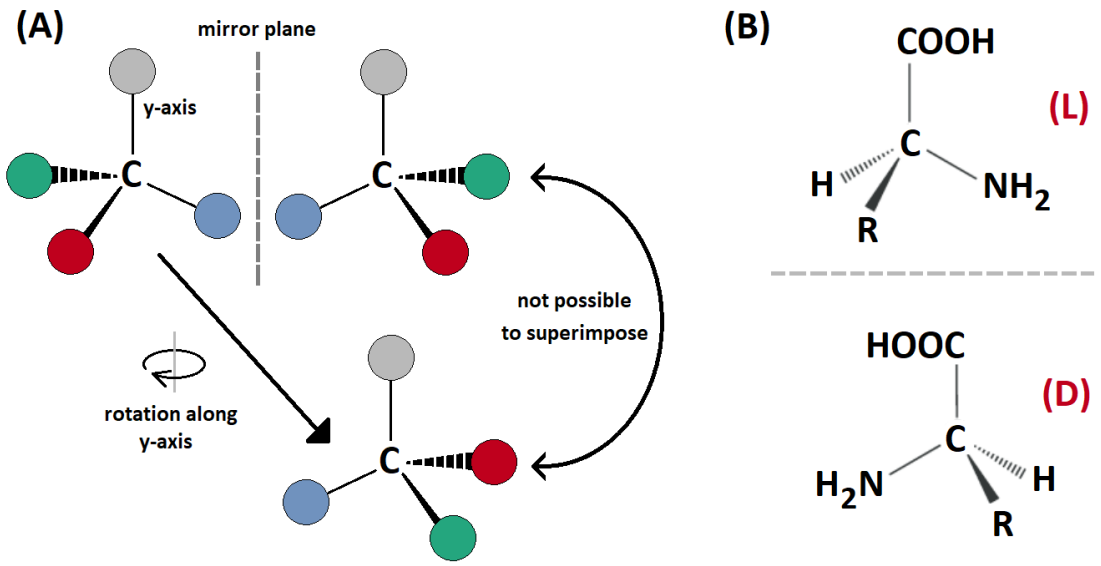

Figure 1. Chirality of organic molecules with asymmetric carbon. **(A)** Enantiomers are molecules with the same formula and bond structure that are mirror images of each other. They cannot be superimposed by any combination of rotations and translations. **(B)** Many organic molecules such as sugars or amino acids are chiral and only one enantiomer is preferred in living organisms. For example, the *L*-amino acids are found in proteins and peptides almost exclusively.

Chiral molecules are optically active. If molecules are optically active without an external influence (e.g. magnetic field), they exhibit natural chirality. Optical activity of a molecule may be manifested as the ability to rotate the plane of linearly polarized light measured as optical rotatory dispersion (ORD). A more general definition would involve any differential response of chiral molecular system to the left- and right-circularly polarized light. Since circularly polarized light possesses an intrinsic handedness, it interacts differently with chiral molecules. Enantiomeric species rotate the plane of polarized light by the same magnitude but in opposite direction. A racemic (50:50) mixture of enantiomers does not exhibit natural chirality. Different light wave polarizations are illustrated in **Figure 2**.

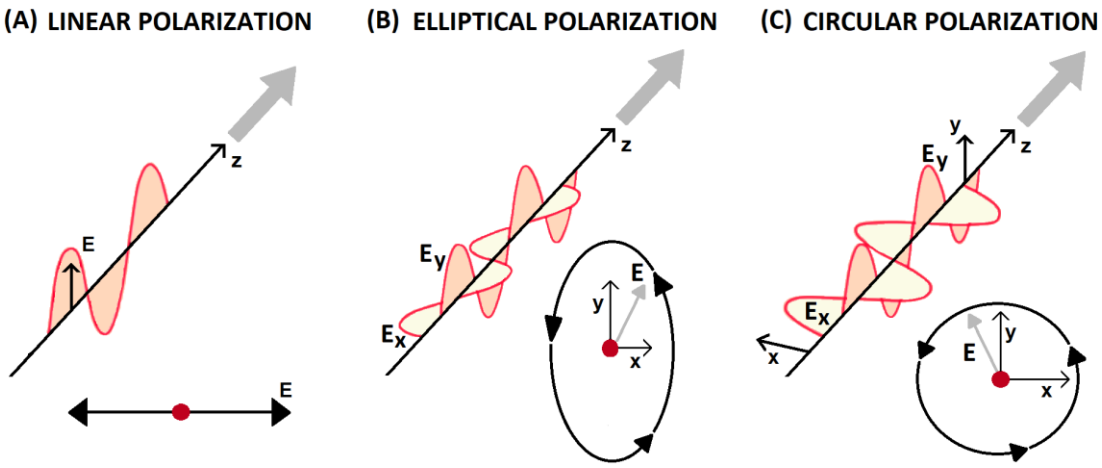

Figure 2. Different polarizations of a light wave. **(A)** In the linearly polarized light, vector of the electric intensity **E** oscillates in a plane perpendicular to the direction of propagation. **(B)** The elliptically polarized wave can be regarded as a superposition of two mutually orthogonal plane polarized waves with different amplitudes and phases. In this case, the **E** vector will rotate and change its amplitude. **(C)** Circular polarization is a special case of elliptically polarized light that arises when two plane waves have equal amplitudes and a phase difference of $\pi/2$. If the resultant electric field vector **E** rotates clockwise then the light is right-circularly polarized. The **E** vector rotates by 360° as the wave advances by one wavelength.[12]

We can use the electromagnetic theory to describe the differential interaction of circularly polarized light with a chiral molecule. Besides the electric dipole moment induced by the electric field of the light, the electric dipole induced by the oscillating magnetic field, electric field gradient, oscillating magnetic dipole and electric quadrupole moments need to be considered. The electric dipole (μ_α), magnetic dipole (m_α) and electric quadrupole ($\Theta_{\alpha\beta}$) operators are listed in equations 1 – 3, where a particle i at r_i has charge e_i, mass m_i and linear momentum p_i.[13]

$$\mu_\alpha = \sum_i e_i r_{i\alpha} \tag{1}$$

$$m_\alpha = \sum_i \frac{e_i}{2m_i} \varepsilon_{\alpha\beta\gamma} r_{i\beta} p_i \tag{2}$$

$$\Theta_{\alpha\beta} = \frac{1}{2} \sum_i e_i \left(3 r_{i\alpha} r_{i\beta} - r_i^2 \delta_{\alpha\beta}\right) \tag{3}$$

For example, electric field of a planar wave (eq. 4) induces oscillating electric and magnetic dipole and electric quadrupole moments given by the dynamic molecular property tensors: the electric dipole-electric dipole tensor also known as polarizability responsible for light scattering ($\alpha_{\alpha\beta}$), the electric dipole-magnetic dipole tensor ($G'_{\alpha\beta}$) and electric dipole-electric quadrupole tensor ($A_{\alpha\beta\gamma}$) responsible for Raman optical activity (eqs. 5 – 7). Equation 4 describes the electric field vector of a plane wave of angular frequency $\omega = 2\pi c/\lambda$ traveling in the direction of a unit vector $\boldsymbol{n}$ with velocity c, t is time and r is position. In eq. 5 – 7, n and j denote the ground and excited states of a molecule, $\omega_{jn} = \omega_j - \omega_n$ is the difference of their angular frequencies, ω is the frequency of the radiation.[13]

$$\boldsymbol{E} = \boldsymbol{E}^0 exp\left[-i\omega\left(t - \frac{\boldsymbol{n.r}}{c}\right)\right] \tag{4}$$

$$\alpha_{\alpha\beta} = \frac{2}{\hbar}\sum_{j\neq n}\frac{\omega_{jn}}{\omega_{jn}^2-\omega^2}\,Re\left(\langle n|\mu_\alpha|j\rangle\langle j|\mu_\beta|n\rangle\right) \tag{5}$$

$$G'_{\alpha\beta} = -\frac{2}{\hbar}\sum_{j\neq n}\frac{\omega}{\omega_{jn}^2-\omega^2}\,Im\left(\langle n|\mu_\alpha|j\rangle\langle j|m_\beta|n\rangle\right) \tag{6}$$

$$A_{\alpha\beta\gamma} = \frac{2}{\hbar}\sum_{j\neq n}\frac{\omega_{jn}}{\omega_{jn}^2-\omega^2}\,Re\left(\langle n|\mu_\alpha|j\rangle\langle j|\Theta_{\beta\gamma}|n\rangle\right) \tag{7}$$

Chiroptical spectroscopy can be used for absolute configuration determination and chirality sensing in organic synthesis,[14, 15] asymmetric catalysis,[16, 17] structural biology, medicine, and material sciences.[18] In pharmacology, the chirality of drugs and their metabolites may determine their efficiency and side effects.[19, 20]

1.2. Chirality Determination by Chiroptical Spectroscopy

Chiroptical spectroscopy exploits different electronic and vibrational states of a chiral molecule. The most common methods are listed in **Table 1**. Optical rotatory dispersion based on the rotation of the plane of linearly polarized light by a chiral molecule was predominantly used in the past. It is now mostly replaced by electronic circular dichroism (ECD). Among methods that sample electronic transitions,

circularly polarized luminescence (CPL) is also advantageous. In lanthanide complexes, we used it to study chirality of the environment around the metal. Vibrational optical activity (VOA) methods proved to be very valuable in conformational analysis. An advantage of VOA with respect to electronic methods is that studied molecules do not need to possess a special chromophore. VOA basically samples the structure through the geometry of the chemical bonds. There are two VOA methods: vibrational circular dichroism (VCD) and Raman optical activity (ROA).

Table 1. Common chiroptical spectroscopic methods.[21]

Natural Chirality:	**Electronic Transitions**	**Vibrational Transitions**
Optical Rotatory Dispersion	standard method, often replaced by ECD	possible, not much used at the moment
Circular Dichroism	electronic CD, standard analytical method	vibrational circular dichroism, firstly observed in 1970s,[22] commercialized in 1997
Circularly Polarized Luminescence	starting to be commercially available	unknown
Raman Optical Activity	unexplored	observed in 1973,[23] commercialized in 2005[24]
Magnetic analogues:		
Magnetic ORD	the Faraday effect	not used
Magnetic Circular Dichroism	MCD, fairly standard method	MVCD, observed in 1984[25] and explained in 2018,[26] rather rare
Magnetic CPL	fairly available but rather rare	unknown
Magnetic ROA	possible in resonance[27]	possible in resonance[28]

Besides the methods exploiting natural chirality of molecules, magnetic analogues can be used to study chiral responses of both chiral or non-chiral molecules in the magnetic field. These methods also lead to the differential response to the left- and right-circularly polarized light and they allow to obtain extended information about the studied systems. Some of them are rather unexplored or used very rarely; magnetic circular dichroism (MCD) is probably used most often, e.g. to study aromatic molecules or inorganic complexes with complex electronic structure.

The most common chiroptical spectroscopic methods and those used in this thesis are discussed in more details in the following chapters. Electronic circular dichroism spectroscopy is explained in Chapter 1.2.1. Chapters 1.2.2. and 1.2.3. describe VOA methods of vibrational circular dichroism and Raman optical activity. Circularly polarized luminescence is discussed in Chapter 1.2.4., and some magnetic methods, mainly magnetic circular dichroism, are explained in Chapter 1.2.5.

1.2.1. Electronic Circular Dichroism

Circular dichroism was discovered in the first half of the 19th century and its potential was fully developed in the 20th century. Circular dichroism is defined as a differential absorption of left- and right-circularly polarized light by a chiral molecule. In the Lambert-Beer's law, a molar extinction coefficient is defined as:

$$\varepsilon = \frac{A}{c \cdot l} \tag{8}$$

where c is the concentration of the absorbing species, usually in mol/L, A is the absorbance and l is the pathlength expressed in centimeters. For chiral molecules, the absorbance and the molar extinction coefficient for right- and left-circularly polarized light (ε^L and ε^R, respectively) differ (eq. 9 and 10). A dissymmetry factor g (eq. 11) is also a very important characteristic as a quantitative measure of chiral response, it is independent of the concentration and pathlength.[29, 30]

$$\Delta\varepsilon = \varepsilon^L - \varepsilon^R = \frac{\Delta A}{c \cdot l} \tag{9}$$

$$\Delta A = A^L - A^R \tag{10}$$

$$g = \frac{\Delta\varepsilon}{\varepsilon} = \frac{A^L - A^R}{A} \tag{11}$$

Electronic circular dichroism can be also expressed as ellipticity θ of the light. We can suppose that the intensities of incident left- and right-circularly polarized light (I_{L0} and I_{R0}, respectively) interacting with the sample are the same, i.e. we irradiate the sample with a light polarized in a plane. After the absorption, the intensities of the outgoing left- and right-circularly polarized light (I^L and I^R) differ (eq. 12 and 13) and the electric field intensity vector no longer oscillates along one line (seen along the beam), but follows an ellipse. The ellipse is determined by an angle θ connected to the major (a) and minor (b) axes of the ellipse by equation 14. A schematic representation of discussed events is shown in **Figure 3**. Equation 15 allows to convert the molar ellipticity to the differential molar extinction coefficient.[30]

$$I_{L0} = I_{R0} \tag{12}$$

$$I^L \neq I^R \tag{13}$$

$$\theta = \arctan\frac{b}{a} \tag{14}$$

$$\theta = 3300\Delta\varepsilon \tag{15}$$

Clearly, circular dichroism can be measured only in the presence of absorption. To be active in UV-Vis CD, a molecule must contain a chromophore absorbing ultraviolet or visible light. For example, extended π-electron systems usually act as strong chromophores.[29] Selected organic chromophores with UV electronic transitions are illustrated in **Figure 4**.

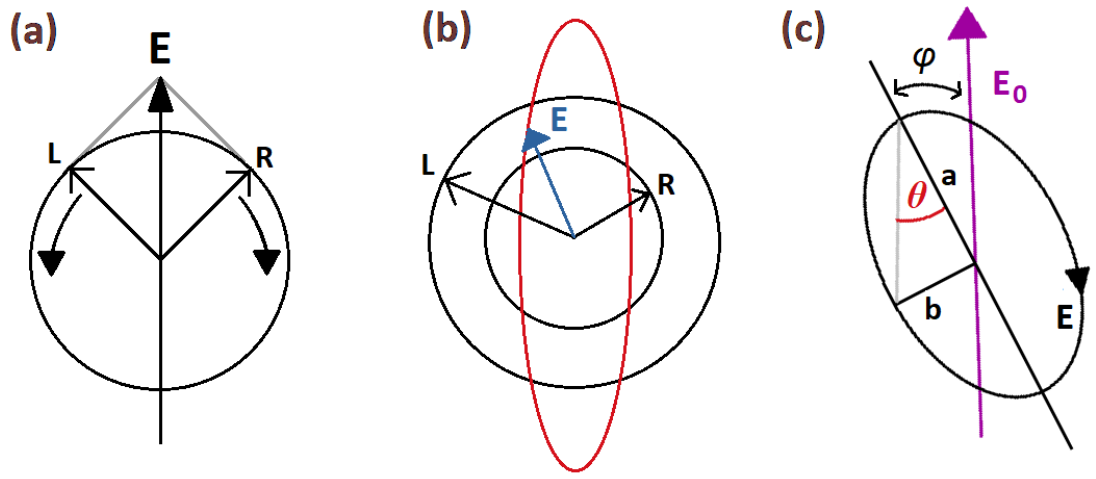

Figure 3. Diagram illustrating how the electric intensity vectors of the left- (*L*) and right- (*R*) circularly polarized light combine. **(a)** If the amplitudes are the same, we obtain plane polarized light; **(b)** a difference in the amplitudes of E_L and E_R results in the elliptically polarized light; **(c)** the major (*a*) and minor (*b*) axes form a triangle and the angle θ is ellipticity. The angle φ between the major axis of the ellipse and $\mathbf{E_0}$ corresponds to the optical rotation.[30]

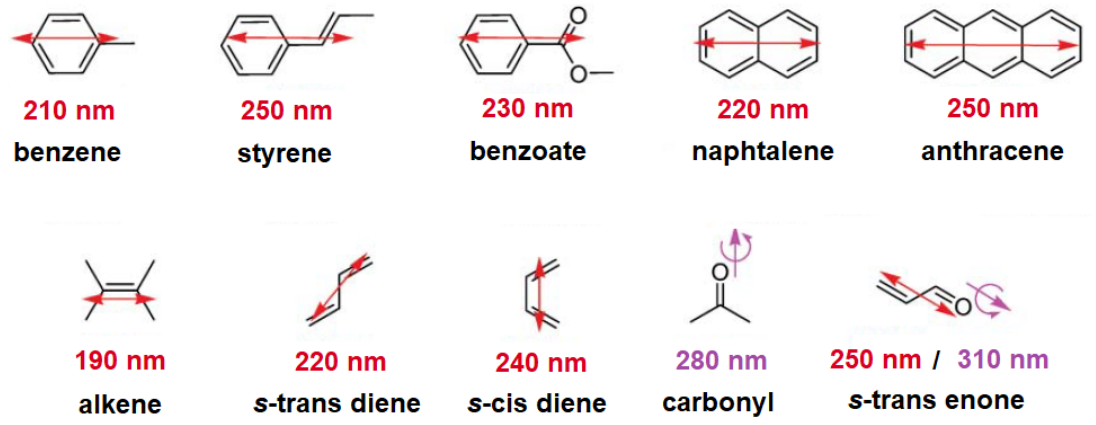

Figure 4. Examples of organic chromophores active in UV. The strongest electric transition dipoles are shown as red double arrows, magnetic dipoles as pink single arrows.[29]

In rigid molecules, the sign of electronic circular dichroism is indicative of the absolute configuration (AC). With help of quantum chemistry methods, AC can be determined from ECD. In biopolymers and aggregates, the sign and shape of ECD indicates also the conformation. In the past, ECD studies of protein conformation brought a lot of insight into the secondary structure and dynamic processes involved

in protein folding and denaturation. Several chromophores contribute to protein absorption and ECD spectra. The peptide bond (CONH) absorbs in the UV region below 240 nm. Side chains of aromatic amino acids (e.g. tyrosine, histidine, tryptophane and phenylalanine) are responsible for the absorption within 260 – 320 nm. The disulphide bridges of cysteine provide weak and broad absorption band around 260 nm. ECD intensities associated with the so called $n \rightarrow \pi^*$ (~ 220 nm) and $\pi \rightarrow \pi^*$ (190 nm) transitions of the peptide bond are strongly indicative of the secondary structure of polypeptide chain. **Figure 5** illustrates typical ECD spectral patterns for three protein secondary structures.[31-33]

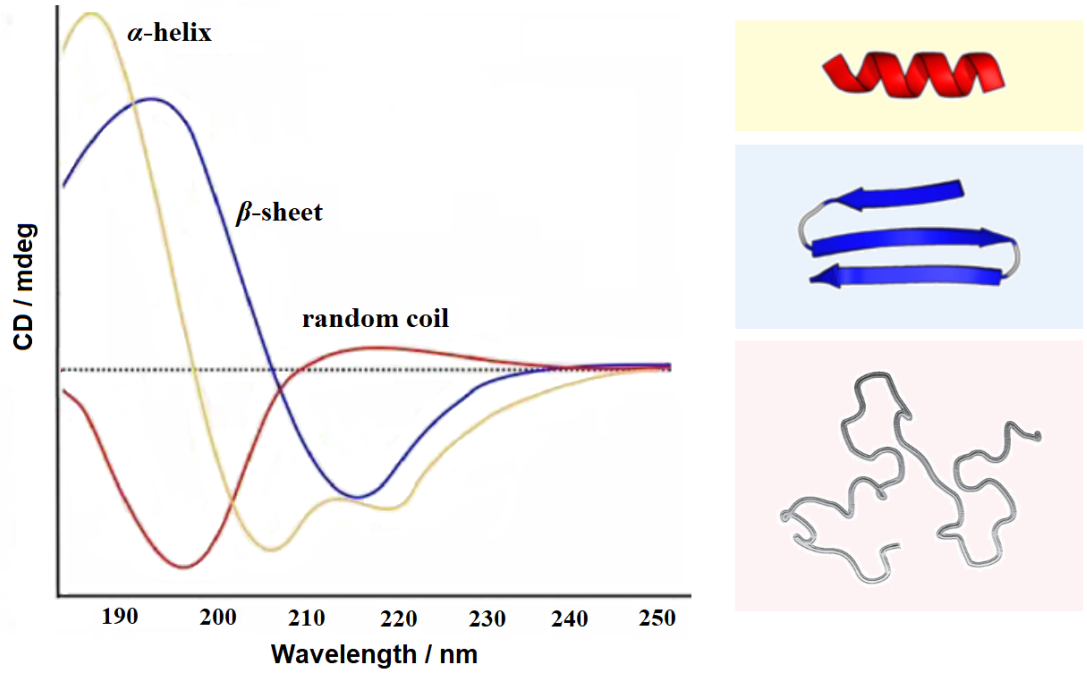

Figure 5. ECD spectra of three most prevalent secondary structures of proteins: *α*-helix (yellow), *β*-sheet (blue) and random coil (red).[31]

We can consider protein ECD spectrum as a linear combination of all contributing secondary structures (e.g. *α*-helix, *β*-sheet and random coil). By a deconvolution, we get the ratios of the secondary structures in a protein. This method is simple, but one needs to be aware of the limitations. For example, secondary structures and their spectra can differ in various proteins. Currently, a number of

software packages or online services can be used to analyze protein electronic circular dichroism spectra.[34-36]

1.2.2. Vibrational Circular Dichroism

Vibrational circular dichroism (VCD) also allows for a chirality discrimination in molecules.[37] It can be viewed as an extension of electronic circular dichroism to the infrared region. However, vibrational spectra in general consist of more bands, the information provided is richer and can be more directly correlated to the structure. The presence of chromophores active in UV-Vis is not necessary and spectral interpretation is easier.[38] The theoretical basis for VCD was developed around 50 years ago,[39-43] soon followed by the first experiments.[44-47] In the following decades, VCD became an important technique for studies of the structure of biopolymers such as proteins and peptides[48-55] or nucleic acids.[56-62]

The intensity of absorption is proportional to the dipole strength (*D*). The intensity of both ECD and VCD is proportional to rotational strength (*R*). For a transition $n \rightarrow k$, the equations for dipole and rotational strengths are:

$$D_{kn} = Re\,\{\langle n|\mu|k\rangle \cdot \langle k|\mu|n\rangle\} \tag{16}$$

$$R_{kn} = Im\,\{\langle n|\mu|k\rangle \cdot \langle k|m|n\rangle\} \tag{17}$$

where μ corresponds to the operator of electric dipole moment and *m* to the operator of magnetic dipole moment. For vibrational transitions, $|n\rangle$ and $|k\rangle$ refer to ground and excited vibrational states of the same ground electronic state.

A drawback of VCD is a low intensity of the measured signal. Sample concentrations, optical pathlength and accumulation times need to be optimized to achieve high signal-to-noise ratio. Similarly as for ECD, the dissymmetry *g*-factor can be defined. It is related to dipole and rotational strengths in eq. 18.[28] Usually, VCD *g*-factor ranges between 10^{-4} and 10^{-5} for most molecules. Only in special cases, e.g. for molecular condensation, *g*-factors as high as 10^{-3} or 10^{-2} can sometimes be measured.[63]

$$g = \frac{\Delta A}{A} = \frac{4R_{kn}}{D_{kn}} \tag{18}$$

Infrared absorption is not sensitive to enantiomers, while VCD provides "mirror-image" spectra. Racemic mixture of enantiomers does not provide any VCD. This is shown in **Figure 6** for (+) and (-) enantiomers of α-pinene.

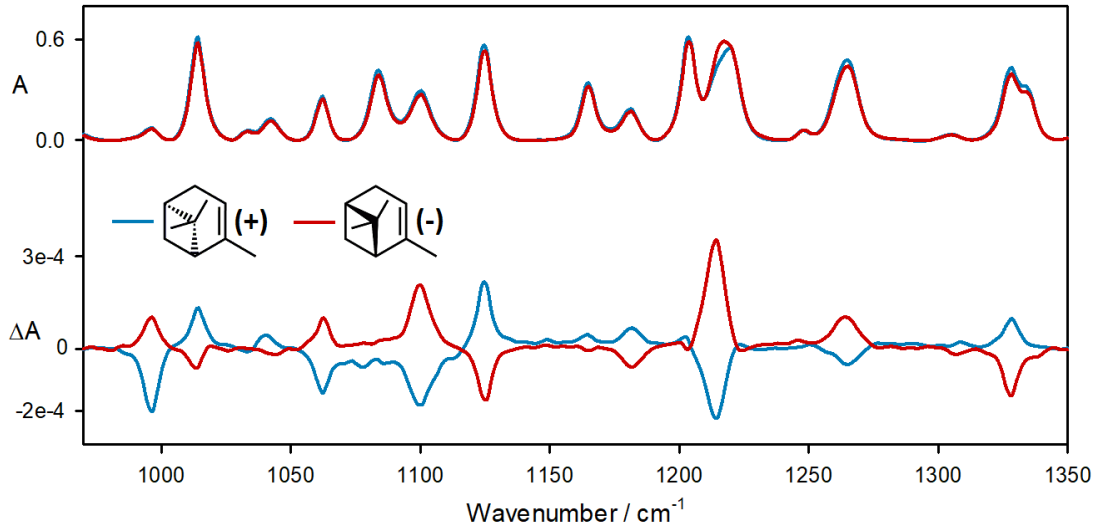

Figure 6. Infrared absorption (top) and VCD (bottom) spectrum of (+) and (-) enantiomer of α-pinene. The spectrum for neat α-pinene was measured in BaF_2 cell with 50 μm pathlength for 1 hour (*Chiral IR-2X* instrument, *BioTools, Inc.*).

As for ECD, VCD is frequently used to elucidate the structure of biopolymers. For proteins, absorption and VCD spectra are usually comprised of so called amide I (1600 – 1700 cm^{-1}, mainly C=O stretching and out-of-phase C-N stretching) and amide II (~1550 cm^{-1} in H_2O and 1450 cm^{-1} in D_2O, C-N stretching and N-H bending) vibrations.[64] VCD spectra in the amide I region characteristic for three protein secondary structures are illustrated in **Figure 7**. VCD is also used to unravel the structure of supramolecular protein aggregates, such as amyloid fibrils. According to accepted theories, the strong (VCD) chirality of aggregates is caused by a coherent coupling of chromophores in a regular structure. A detailed discussion of this phenomenon can be found in Chapter 2.2.2.

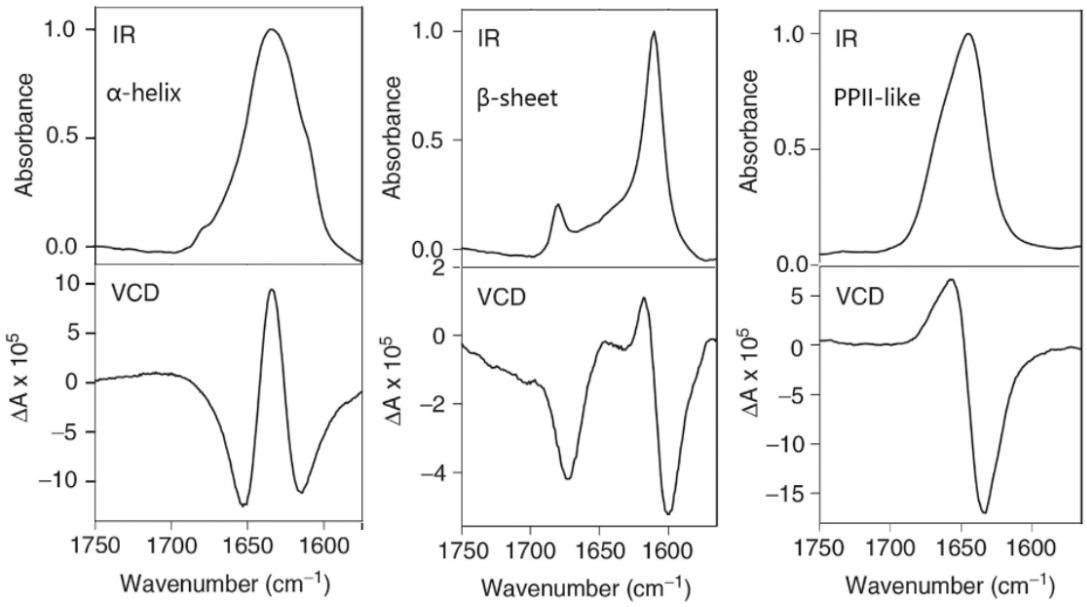

Figure 7. Infrared absorption and VCD spectra of poly-*L*-lysine in D_2O in the amide I region for three conformations: *α*-helix (left), *β*-sheet (middle) and polyproline-II (right).[64]

VCD can be measured on dispersive or Fourier transform (FT) spectrometers. In the dispersive instrument, a grating enables to scan through the wavenumbers and sequentially record the spectrum, while Fourier one uses the Michelson interferometer and Fourier transformation to convert the mirror positions to wavenumber representation. The entire mid-IR region is measured simultaneously on FT-VCD instrument, which is advantageous for the absolute configuration determination and other studies of small and medium sized organic molecules. On the other hand, dispersive instruments may provide better signal to noise ratio in narrow frequency regions, which can be advantageous for amide I and II measurements of proteins and peptides,[65] or for the hydrogen/deuterium stretching region between 3500 and 2000 cm^{-1}.[66] Only FT-VCD instruments are commercially available; dispersive VCD instruments up to date have been built for research purposes only.[67-69] In this work, we used a *Chiral IR-2X* FT-VCD instrument from *BioTools, Inc*. In this instrument, two photoelastic modulators (PEM) are used to suppress the artifacts and straighten the baseline.[70] A schematic diagram of this instrument is shown in **Figure 8**.

Special materials such as calcium or barium fluoride (CaF_2 and BaF_2) are used for construction of sample cell windows due to their low absorption in the mid-infrared

region. Both liquid and solid samples can be measured. Rotation of the samples during spectra acquisition is sometimes necessary to minimize the artifacts in solid or other samples. Also, deuteration and D_2O as a solvent are often used for biomolecules due to the strong absorption of H_2O in the regions of interest.

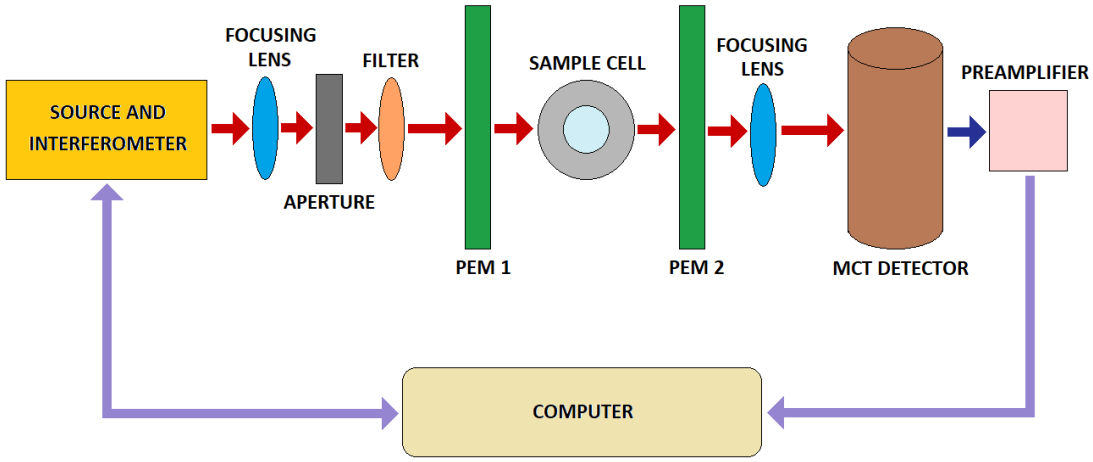

Figure 8. A diagram of a *Chiral IR-2X* FT-VCD instrument from *BioTools, Inc.*[71]

The interpretation of VCD spectra is often dependent on quantum chemistry calculations. Firstly, only empirical and semiempirical models, such as a coupled oscillator model, were available for VCD interpretation,[41, 57, 72, 73] providing only a limited accuracy. After the development of corresponding theory,[74] *ab initio* calculations of VCD intensities were implemented in a number of quantum chemistry software packages.[75-77] For simulation of VCD spectra within the harmonic approximation, several molecular property tensors such as Hessian ($f_{i\alpha,j\beta}$; force constants, second derivatives of energy with respect to the positions of atoms *i* and *j*), atomic polar tensor ($P_{\alpha,i\beta}$; electric dipole derivatives) and atomic axial tensor ($A_{\alpha,i\beta}$; magnetic dipole derivatives with respect to nuclear momenta) must be calculated. The tensors are summarized in eq. 19 to 21.[78]

$$f_{i\alpha,j\beta} = \frac{\partial^2 E}{\partial r_{i\alpha} \partial r_{j\beta}} \tag{19}$$

$$P_{\alpha,i\beta} = \frac{\partial \mu_\alpha}{\partial r_{i\beta}} \tag{20}$$

$$A_{\alpha,i\beta} = \frac{\partial m_\alpha}{\partial p_{i\beta}} \tag{21}$$

These calculations are very straightforward and give good results for small molecules.[79-81] Applications to bigger flexible systems, such as biopolymers, are more limited. For this purpose, several fragment-based methods such as Cartesian coordinate transfer (CCT)[82-84] or molecules-in-molecules (MIM)[85-87] were developed. They allow for the transfer of molecular property tensors from smaller fragments to big molecules, thus allowing for a relatively precise calculation of sizable systems. Since interaction of a molecule with a solvent also influences VCD spectra,[88-91] the correct description of the solvation *in silico* is important. This can be achieved by different approaches such as explicit solvation, implicit solvation models, or combinations of both.[92-95]

1.2.3. Raman Optical Activity

First successful ROA experiments were conducted in 1973.[23] The original incident circular polarization (ICP) experiment, which measured the differential Raman scattering of incoming right- and left-circularly polarized light, was followed in 1988[96] by a scattered circular polarization setup (SCP) in which a small circularly polarized component in the scattered light is measured. Aside from the ICP and SCP setups, two other dual circular polarization modes, the in-phase (DCP_I) and out-of-phase (DCP_{II}) Raman optical activity, are used.[97-99] These polarization modes are schematically described in **Figure 9**.

Aside from polarization setup, the scattering angle can be varied from forward (0°), right-angle (90°) to backward (180°) scattering. A useful measure of ROA is a circular intensity difference (CID), which is defined as a ratio of ROA to Raman scattering intensities (I^L and I^R represent the intensities of left- and right-circularly polarized light, respectively):

$$CID = \frac{I^R - I^L}{I^R + I^L} \tag{22}$$

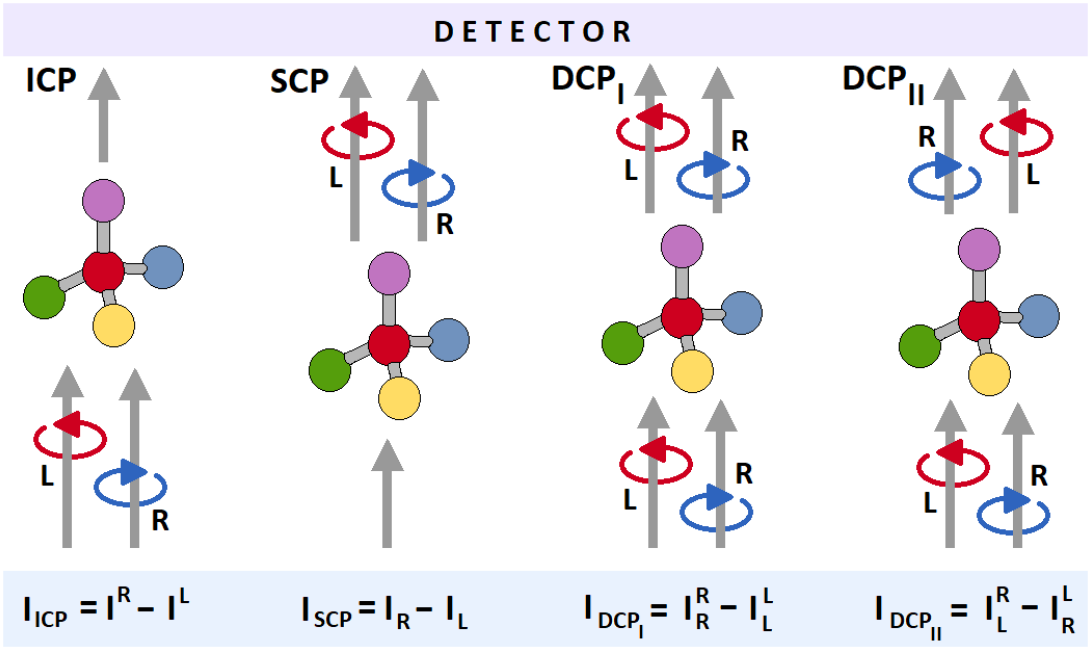

Figure 9. Different ROA polarization modes. ICP polarization mode measures the difference in scattering of circularly polarized incident radiation, SCP measures a small circularly polarized component in scattered light. In dual circular polarization modes, both the incident and scattered lights are circularly polarized.

The ROA intensity is determined by the $\alpha_{\alpha\beta}$, $G'_{\alpha\beta}$ and $A_{\alpha\beta\gamma}$ tensors defined in the Chapter 1.1. As can be seen in equations 23 to 26, for liquids and solutions CID for different scattering angles is a function of rotational invariants of these tensors.[13, 100]

$$CID_{180^\circ} = \frac{24\left[\beta(G')^2 + \frac{1}{3}\beta(A)^2\right]}{c[45\alpha^2 + 7\beta(\alpha)^2]} \tag{23}$$

$$CID_{x,90^\circ} = \frac{12\left[45\alpha G' + 7\beta(G')^2 + \beta(A)^2\right]}{c[45\alpha^2 + 7\beta(\alpha)^2]} \tag{24}$$

$$CID_{y,90^\circ} = \frac{2\left[\beta(G')^2 - \frac{1}{3}\beta(A)^2\right]}{c\beta(\alpha)^2} \tag{25}$$

$$CID_{0^\circ} = \frac{4\left[45\alpha G' + \beta(G')^2 - \beta(A)^2\right]}{c[45\alpha^2 + 7\beta(\alpha)^2]} \quad (26)$$

The invariants α, G', $\beta(\alpha)^2$, $\beta(G')^2$ and $\beta(A)^2$ (eq. 27 – 31) are not dependent on the choice of origin, and are measurable.[13]

$$\alpha = \frac{1}{3}\alpha_{\alpha\alpha} = \frac{1}{3}\left(\alpha_{xx} + \alpha_{yy} + \alpha_{zz}\right) \quad (27)$$

$$G' = \frac{1}{3}G'_{\alpha\alpha} = \frac{1}{3}\left(G'_{xx} + G'_{yy} + G'_{zz}\right) \quad (28)$$

$$\beta(\alpha)^2 = \frac{1}{2}\left(3\alpha_{\alpha\beta}\alpha_{\alpha\beta} - \alpha_{\alpha\alpha}\alpha_{\beta\beta}\right) \quad (29)$$

$$\beta(G')^2 = \frac{1}{2}\left(3\alpha_{\alpha\beta}G'_{\alpha\beta} - \alpha_{\alpha\alpha}G'_{\beta\beta}\right) \quad (30)$$

$$\beta(A)^2 = \frac{1}{2}\omega\alpha_{\alpha\beta}\varepsilon_{\alpha\gamma\delta}A_{\gamma\delta\beta} \quad (31)$$

If a molecule is axially symmetric, then $\beta(G')^2 = \beta(A)^2$ and $\alpha G' = 0$. In this case, ROA is generated only by an anisotropic scattering and CID expressions for 0° and 180° scattering configurations reduce to:[28]

$$CID_{0^\circ} = 0 \quad (32)$$

$$CID_{180^\circ} = \frac{32\beta(G')^2}{c[45\alpha^2 + 7\beta(\alpha)^2]} \quad (33)$$

Raman optical activity is zero in 0° and maximal in the 180° scattering configuration. Since the backscattering geometry boosts CID, it allows to lower the artifacts and improve the signal to noise ratio.[101, 102] Most of current ROA instruments therefore use the backscattering configuration either in ICP mode (mainly instruments built in-house)[103-107] or SCP mode (commercial instrument).[24] Most experiments presented in this thesis were conducted with the *ChiralRaman-2X* instrument from *BioTools, Inc.* The simplified design of this instrument is shown in **Figure 10**.

The incident light at 532 nm is produced by a frequency-doubled Nd:YAG laser, its initial linear polarization is scrambled by optical elements and then it is deflected by a prism into the sample compartment. The backscattered light is conducted to the large circularity converter which converts circularly polarized states to linear polarization states, and to the notch filter that filters out the intense Rayleigh line. The beam splitter then separates the right- and left-circularly polarized components of light into the fiber optics where they are dispersed onto a CCD detector. The final subtraction of intensities is handled by an instrumental software.[24, 100, 108]

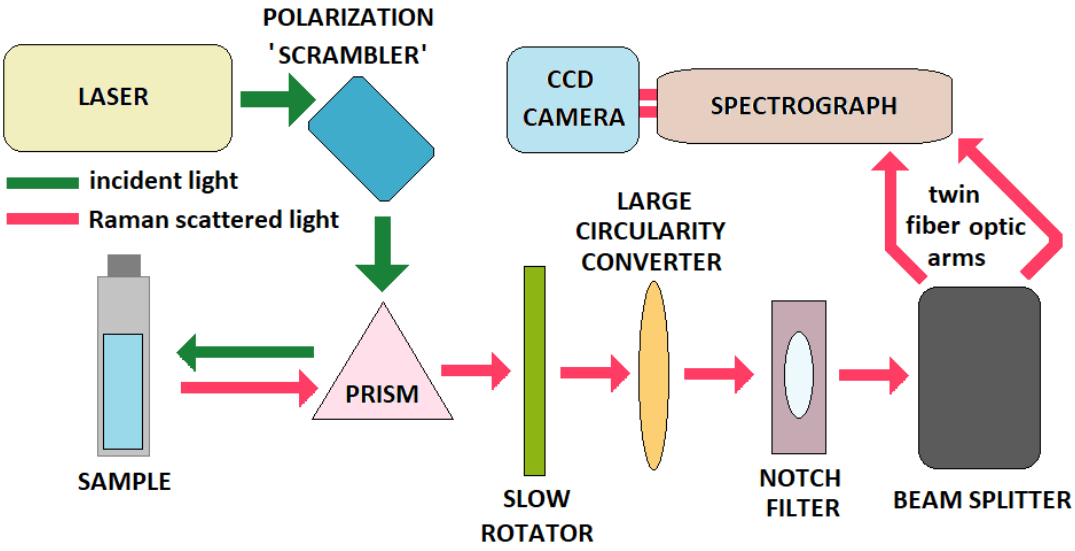

Figure 10. A simplified diagram of the *ChiralRaman-2X* instrument by *BioTools, Inc.*[71, 100, 109] Linearly polarized light at 532 nm is produced by a laser and led through the optical elements to the sample compartment. Raman backscattered beam is then collected by a beam splitter and separated to the right- and left-circularly polarized components which are then detected by a CCD camera.

ROA found applications in organic synthesis and analysis,[71, 110] chemistry of natural products[111] or pharmaceutical industry.[112] It can monitor conformations of small organic molecules as well as large biological systems such as polysaccharides, nucleic acids and proteins. While Raman scattering spectra of proteins are dominated by signals from side chains of amino acids, ROA samples more the peptide backbone. ROA is therefore more sensitive to the protein secondary structure. Moreover, it allows for the measurements in water in the whole region of fundamental vibrations. The

Raman scattering is a very rapid process (10^{-12} to 10^{-13} s) when compared to e.g. molecular motions (10^{-1} to 10^{-9} s). ROA spectrum is therefore a superposition of all conformations in the sample, and it allows for the analysis of the dynamics and conformational mobility.[100]

1.2.4. Circularly Polarized Luminescence

Circularly polarized luminescence is a differential emission of left- and right-circularly polarized light. It is somewhat analogous to electronic circular dichroism in the sense that ECD describes the absorption of a photon by a chiral molecule and CPL studies the emission process. ECD samples structure of the ground electronic state, CPL reflects the emitting state.

During luminescence, the molecule participates in several distinct events (**Figure 11**). At room temperature, the majority of molecules populate the lowest vibrational level of the ground state (for closed shell molecules usually S_0). Upon absorption of a photon, the molecule is excited to one of the singlet excited states (S_n). A molecule can undergo an internal non-radiative conversion. Upon intersystem crossing, a transition between excited singlet and energetically close triplet states occurs. This process is generally forbidden due to the conservation of spin angular momentum, although spin-orbit coupling weakly allows it. If a molecule emits a photon from say vibrational level of S_1 to S_0 without the multiplicity change, we call this process a fluorescence ($\Delta S = 0$). Phosphorescence usually refers to a radiative transition between triplet excited and singlet ground state ($\Delta S \neq 0$). Phosphorescence is generally a forbidden transition, slightly allowed through spin-orbit coupling, therefore it is much slower when compared to fluorescence. While fluorescence usually occurs on the timescale of 10^{-9} to 10^{-7} s, phosphorescence lifetimes are in the range of 10^{-6} to 10 s.[113]

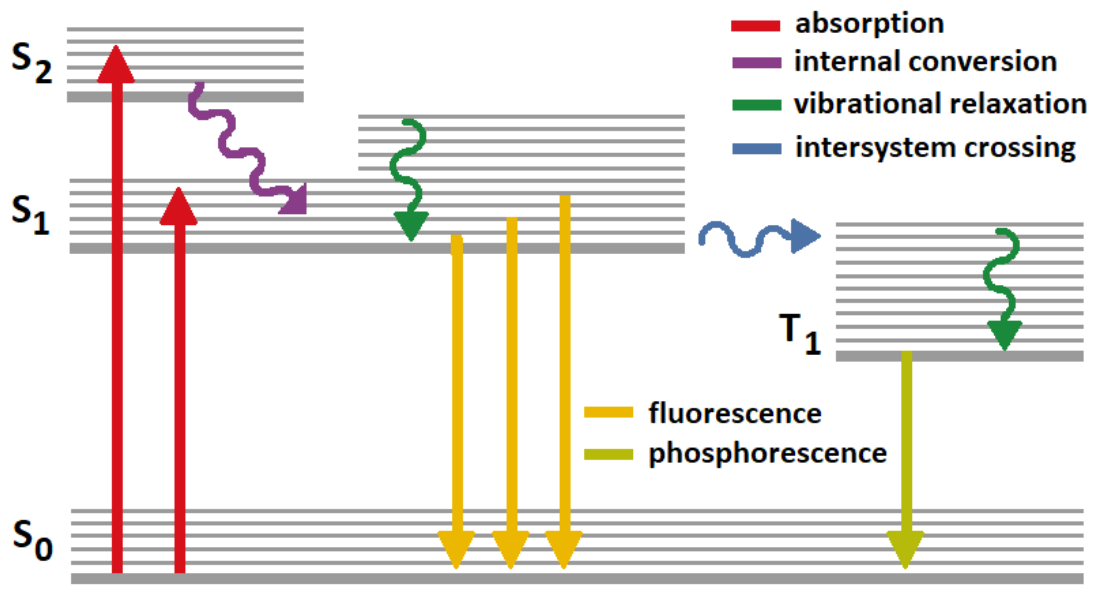

Figure 11. Jablonski diagram of radiative and non-radiative transitions involved in the process of luminescence. S_0 refers to the singlet ground state of the molecule, S_n to the n^{th} excited singlet state and T_1 to the first excited triplet state.

Similarly as for ECD and VCD, relative intensity of circularly polarized luminescence may be described by a dissymmetry factor g_{lum} (eq. 34). For a transition at ω, it is defined as a ratio between the intensity of CPL ($\Delta I = I_L - I_R$) and total luminescence ($I = I_L + I_R$) multiplied by a factor of 2.[114] For most of chiral organic molecules, values for g_{lum} from 10^{-2} to 10^{-3} are measured. Even bigger dissymmetry factors with $g_{lum} \sim 1$ can be observed for some lanthanide complexes.[115]

$$g_{lum}(\omega) = \frac{2\Delta I(\omega)}{I(\omega)} \tag{34}$$

Similarly as for UV absorption and ECD, intensities of total and circularly polarized luminescence can be related to the dipole (D_{0m}) and rotational (R_{0m}) strengths by equations 35 and 36, where c is the speed of light, $\hbar$ is the reduced Planck's constant and $\rho(E)$ is related to band shape. The dissymmetry factor can be expressed using the rotational and dipole strengths as in eq. 37.[116, 117]

$$I = \frac{4E^3\rho(E)}{3\hbar^4c^3}D_{0m} \quad (35)$$

$$\Delta I = \frac{16E^3\rho(E)}{3\hbar^4c^3}R_{0m} \quad (36)$$

$$g_{lum} = \frac{4R_{0m}}{D_{0m}} \quad (37)$$

Circularly polarized luminescence was also applied to many molecular systems. Lanthanides with unique luminescent properties are discussed in the next chapter. In organic molecules, CPL can be applied to chiral ketones and helicenes,[118-120] even though the experiment is challenging due to their relatively low dissymmetry factors (10^{-3} – 10^{-2}). Chiral organometallic complexes with transition metals (mainly Ir^{3+}, Ru^{2+}, Pt^{2+} and others) also provide relatively strong CPL from $\pi \rightarrow \pi^*$ and charge transfer transitions. Metal $d \rightarrow d$ transitions are observed for highly symmetric Cr^{3+} complexes with ligands inducing strong crystal fields. These find their application for example in light-emitting diodes.[121-124]

1.2.4.1. Lanthanides and Their Complexes

Chemical elements with atomic numbers 57 – 71 starting with lanthanum up to lutetium are called lanthanides. Electrons in lanthanides fill up the *4f* shell. Typically, these metals form ions with 3+ oxidation state; 2+ and 4+ ions are also known. Due to the lanthanide contraction, the size of the Ln^{3+} ion decreases with increasing atomic number. Due to the fairly large size of the central ion, high coordination numbers of 6 to 12 are typical for Ln-complexes. Small monovalent ligands usually result in high-symmetry complexes (D_{3h} or C_{3v}), while bulky polydentate ligands form low symmetry configurations (D_3 and lower).[125, 126] By tailoring of the ligands, it is therefore possible to prepare a variety of Ln-complexes with specific geometries and photophysical properties.

Due to their $[Xe]4f^n$ (n = 0 – 14) electronic configuration, lanthanides are quite interesting. The *4f* electrons support many electronic levels. For *n* electrons in the *4f* shell, number of electronic states *N* is:

$$N = \frac{14!}{n!(14-n)!} \tag{38}$$

For Gd^{3+} with 7 electrons in the *4f* shell, this makes 3432 electronic levels, while Eu^{3+} with six *4f* electrons possesses 3003 electronic levels.[127] Lanthanide ions with a few or many *4f* electrons have fewer electronic levels; Ce^{3+} (one *4f* electron) has 14 and Tm^{3+} with twelve *4f* electrons has 91 electronic levels. A simplified energy diagram of several Ln^{3+} ions is illustrated in **Figure 12**.

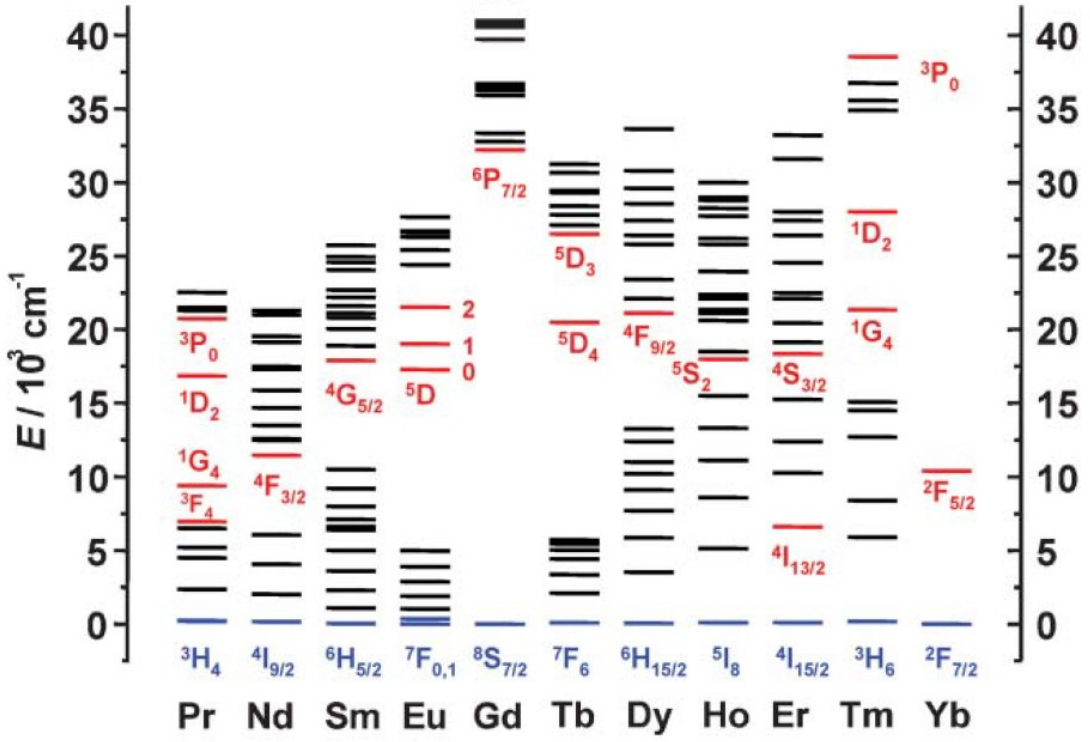

Figure 12. Energy diagrams of several Ln^{3+} ions. The ground states are in blue, the main luminescent levels are in red. In spectroscopic symbols ${}^{M}L_{J}$, the *M* corresponds to the spin multiplicity (*M = 2S + 1*, where *S* is the total spin quantum number), *L* is the total orbital quantum number in spectroscopic notation (0 = S, 1 = P, 2 = D, 3 = F, …) and *J* represents the total angular momentum.[128]

Absorption of a photon by an atom is possible, for example, by the electric dipole (ED), magnetic dipole (MD) and electric quadrupole (EQ) operators. Transitions within the *4f* shell are usually sharp and numerous, somewhat broader are $4f \rightarrow 5d$ transitions and charge transfer transitions.[129] Charge transfer states are generally not emissive, however, they participate in boosting or quenching of $f \rightarrow f$ and $f \rightarrow d$ luminescence.[130] Within the non-relativistic crystal field theory, the transitions are governed by selection rules for *S*, *L* and *J* quantum numbers listed in **Table 2**.

Table 2. Selection rules for transitions within the *4f* shell of lanthanides.[127]

Operator	Parity	ΔS	ΔL	ΔJ
ED	Opposite	0	≤6	≤6
MD	Same	0	0	0, ±1
EQ	Same	0	0, ±1, ±2	0, ±1, ±2

Since electronic states with the same parity can not participate in electric dipole transitions (Laporte's rule), the $f \rightarrow f$ transitions are forbidden. However, under the influence of environment (ligand field), mixing of electronic states of different parity makes $f \rightarrow f$ transitions possible. In lanthanides, magnetic dipole transitions are quite intense and comparable in magnitude to electric dipole transitions. On the other hand, electric quadrupole transitions are very weak and usually not observed. From the absorption or emission spectra, the symmetry of the chemical environment around the Ln^{3+} ion can sometimes be determined due to the splitting of *2J+1* degenerate *J*-levels in the ligand field.[129]

Almost all Ln^{3+} ions are luminescent with $f \rightarrow f$ emission lines covering the entire spectrum from UV (Gd^{3+}) through visible (Pr^{3+}, Sm^{3+}, Eu^{3+}, Tb^{3+}, Dy^{3+} and Tm^{3+}) to near-infrared region (Pr^{3+}, Nd^{3+} or Yb^{3+}). Lanthanide ions can be fluorescent ($\Delta S = 0$), phosphorescent ($\Delta S \neq 0$), or both. The emission lines are usually sharp, with large Stokes shifts and microsecond to millisecond lifetimes.[129] **Table 3** lists the main transitions observed in the luminescence spectra of several Ln^{3+} ions. Lanthanide

luminescent complexes are sometimes designed to benefit from the antenna effect. In this case, the metal center is surrounded by a chelate that stabilizes the complex, prevents the vibrational dissipation of energy, and funnels the energy to the lanthanide. This may be beneficial for biological applications where intense light needed for luminescence can damage the sample.[131, 132]

Table 3. Main luminescent transitions of Ln^{3+} ions.[128]

Ln	Excited State[A]	End State[B]	Type[C]	λ / nm	Emission Color
Pr	$^1G_4$	^3H_J 4-6	P	1300	NIR
	$^1D_2$	^3F_J 2-4	P	890, 1060	NIR
	$^3P_0$	^3H_J 4-6	F	525 - 680	Orange
Nd	$^4F_{3/2}$	^4I_J 9/2-15/2	F	1060	NIR
Sm	$^4G_{5/2}$	^6H_J 5/2-15/2	P	590	Orange
Eu	$^5D_0$	^7F_J 0-6	P	620	Red
Gd	$^6P_{7/2}$	$^8S_{7/2}$	P	312	UV
Tb	$^5D_4$	^7F_J 6-0	P	550	Green
Dy	$^4F_{9/2}$	^6H_J 15/2-5/2	P	570	Yellow-orange
Ho	$^5F_5$	^5I_J 8-4	F	970, 1450	NIR
	$^5S_2$	^5I_J 8-4	F	540	Green
Er	$^4S_{3/2}$	^4I_J 15/2-9/2	F		
	$^4I_{13/2}$	$^4I_{15/2}$	F	1530	NIR
Tm	$^1G_4$	^3H_J 6-4	P		
Yb	$^2F_{5/2}$	$^2F_{7/2}$	F	980	NIR

A Excited state refers to the most luminescent excited state. **B** Possible range of *J*-values corresponding to the transition is indicated on the right. **C** Type of luminescence: P – phosphorescence, F – fluorescence.

As dopants, Ln^{3+} ions are used in lasers (Nd:YAG laser),[133] fiber optics, luminescence sensors, light-emitting diodes, high-temperature superconductors and many more.[134] In medicine and biological sciences, lanthanide compounds are used as biomarkers in magnetic resonance imaging, Förster resonance energy transfer probes, or in the time-resolved luminescence bioassays.[135, 136] Induced lanthanide chirality helps to sense chiral molecules through circular dichroism or circularly polarized luminescence.[137-140]

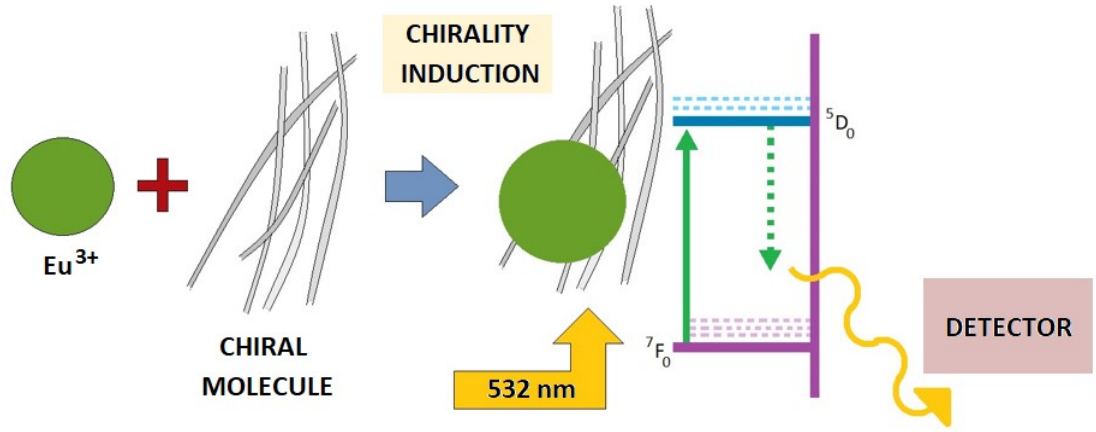

Figure 13. Circularly polarized luminescence spectra of Eu^{3+}/chiral molecule complex.

In our group at IOCB, we have developed a methodology of measuring lanthanide CPL with ROA instrument.[141] The instrument uses 532 nm laser resonant with the $^7F_0 \rightarrow {}^5D_0$ electronic transition in Eu^{3+} ion. The strong laser excitation allows to measure very weak circularly polarized luminescence induced by the environment around the metal (**Figure 13)**. The chirality is induced in the Eu^{3+} ion by a chiral molecule, while the Eu^{3+} ion provides absorbing and emitting electronic states. This method was already applied to sugars,[142, 143] DNA[144] and proteins.[145, 146]

1.2.5. Magnetic Analogues of Natural Chirality

In both chiral and achiral systems, additional chiral response can be induced by application of a static magnetic field along the direction of light propagation. An overview of such methods was shown in **Table 1**, p. 7. For example, the Faraday effect is based on the rotation of the plane of polarized light in different media when magnetic field is applied (magnetic ORD), and is used in astrophysics and optics.[147, 148] Even though magnetic vibrational circular dichroism was first observed more than 35 years ago,[25] the effect was explained only recently[26] and its standard use is complicated by the necessity of strong static magnetic fields needed for spectra measurement. The magnetic circularly polarized luminescence can be used to probe the electronic structure (symmetry, degeneracy, etc.) of emitting states. It is fairly available and mostly used to study the electronic structure of highly luminescent metal ions.[149-151]

Magnetic circular dichroism is defined as a differential absorption of left- and right-circularly polarized light by a system in a static magnetic field oriented parallel to the direction of light propagation. Commercial electronic circular dichroism instruments equipped with a permanent magnet (up to 1.5 T) are used for collection of MCD spectra. Unlike natural circular dichroism, magnetic circular dichroism is a universal property of all matter. The magnetic field perturbs states involved in electronic transitions responsible for the light absorption.[152] MCD can be for example used to distinguish between the overlapping electronic transitions.

The origin of magnetic circular dichroism can be linked to three terms A, B and C (eq. 39; $\Delta\varepsilon$ is difference of molar absorption coefficients for left- and right-circularly polarized light, γ is constant, B is intensity of the applied magnetic field, E is energy of the incident radiation, T is temperature and $f(E)$ is bandshape function).[153]

$$\frac{\Delta\varepsilon}{E} = \gamma \mathrm{B}\left\{-A\frac{\partial f(E)}{\partial E} + \left(B + \frac{C}{T}\right) f(E)\right\} \tag{39}$$

The A term arises from the splitting of otherwise degenerate excited state levels in the presence of magnetic field. The C term is connected to the magnetic field induced splitting in originally degenerate energy levels of the ground state. The C term is temperature dependent because of the different ground state populations at different

temperatures. The *B* term arises from the field induced mixing of electronic states.[154] If the ground state is non-degenerate, the *C* term is zero. Without degeneracy of the excited state, the *A* term is zero as well. The *B* term is always present. **Figure 14** illustrates the typical shapes of individual Faraday terms.

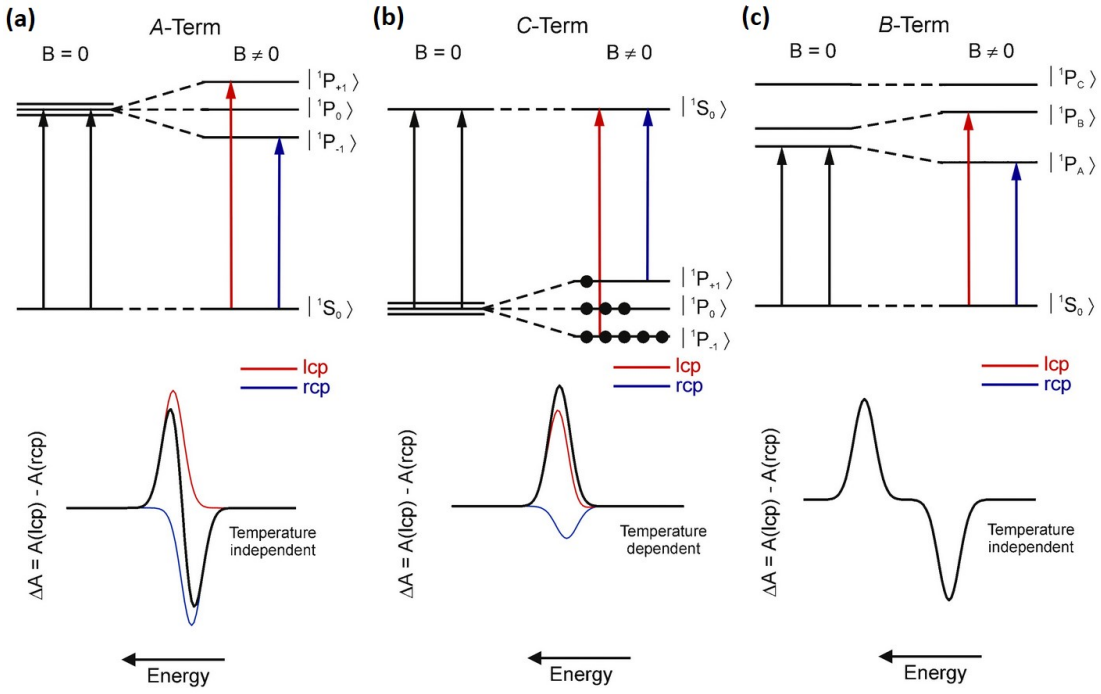

Figure 14. Diagrams of energy levels giving rise to Faraday's *A*, *B* and *C* terms in MCD.[154] One can distinguish them based on the temperature dependence. The *A* term **(a)** is temperature independent and provides a couplet signal. Both *B* **(c)** and *C* **(b)** terms give a single band, however, the *C* term is temperature dependent.

Computations of magnetic circular dichroism spectra are complicated by an origin-dependence of calculated intensities and imaginary wavefunction needed for the magnetic perturbation. Available approaches are based on the magnetically perturbed time-dependent density functional theory,[155] the complex polarization propagation method,[156] or real-time propagation of wavefunction.[157, 158] Also, a sum-over-states (SOS) approach was shown to be usable.[159, 160] More recently, MCD was implemented for correlated multiconfigurational wave functions. With relativity, they can treat the spin-orbit and spin-spin coupling, and allow for simultaneous calculation

of all the *A*, *B* and *C* terms.[161] However, the computational cost of such multireference calculations is significant.

1.3. Future Prospects of Chiroptical Spectroscopy

Chiroptical spectroscopy is very versatile. Measurements in the liquid phase are the most common, applications to solids and gases are also possible. A wide range of solvents can be used. In this section, some of the current trends will be discussed. A more detailed analysis can be found in the review *Recent Trends in Chiroptical Spectroscopy: Theory and Applications of Vibrational Circular Dichroism and Raman Optical Activity* (Krupová, M.; Kessler, J.; Bouř, P.: ChemPlusChem 2020, 85(3), p. 561-575) attached in **Attachment A**.

While the application of electronic circular dichroism to the structural studies of biopolymers such as nucleic acids and proteins is well established, the interpretation is often based on empirical rules. Vibrational optical activity methods are more dependent on computational tools able to simulate the properties of large molecular systems. Fragmentation methods provide VOA spectra of sizable molecules, for which a direct quantum-chemical approach is ineffective or unavailable.[85, 162, 163] In more realistic simulations, the spectra calculations may include averaging of spectra for many solute-solvent clusters obtained from molecular dynamics. This can be further improved by *ab initio* molecular dynamics simulations, in which the nuclei of atoms follow the Newtonian mechanics, but the forces are determined by DFT.[164, 165]

One of the most interesting chiroptical spectroscopy phenomena is connected to the enhancement of spectra intensities by molecular condensation. This phenomenon was first discovered in the 1970s in electronic circular dichroism spectra of condensed DNA,[166] later observed also for VCD.[63] Also, a significant enhancement of VCD signal in amide I region in amyloid fibrils sometimes occurs.[167, 168] A high enhancement of VCD signal can be also achieved for chiral crystals,[169, 170] or for several transition metal and lanthanide complexes.[171, 172]

Another interesting concept is based on the induction of chiral response in achiral materials, e.g. polymers doped with small organic molecules. The achiral

monomeric units form a chiral polymeric (often helical) structure upon interaction with the chiral dopant. This chirality of the polymer often persists even after the removal of the chiral dopant, i.e. the system remembers the chiral perturbation.[173, 174]

Raman optical activity is used in protein and nucleic acid science relatively often, even though the interpretation of the experimental spectra based on calculations is complicated by their molecular size. Currently, DFT calculations are available even for sizable proteins,[175, 176] however, theoretical studies of nucleic acids are so far rather rare.[177] Another interesting concept is the resonance phenomenon in Raman optical activity, which occurs when the frequency of incident radiation in ROA experiment ω is close to the energy of electronic transition ω_{jn} (see eq. 5, 6 and 7 at p. 6 for different polarizabilities). In this case, the difference $\omega^2_{jn} - \omega^2$ approaches zero and all of the polarizabilities, and consequently Raman and ROA intensities, significantly grow. This was observed for some metal complexes,[178, 179] or for carotenoid dyes.[180] From an instrumental point of view, Raman optical activity offers a number of different setups, and only some of them are regularly used today. For example, not only UV and visible light can be used for excitation, but also red and near-infrared.[181] Also, the extension of the usable range for Stokes shifts up to 4000 cm^{-1} can bring new challenges both in experiment and in theory.[182]

2. Chiroptical Spectroscopy of Amyloid Fibrils

Protein misfolding and aggregation into amyloid fibrils is implicated in a variety of diseases, e.g. prion-induced or neurodegenerative brain disorders (Alzheimer's or Parkinson's), or in systemic amyloidoses (**Table 4**). Amyloid fibrils can arise from many different proteins. They are characterized by a high β-sheet content and long fibrillar threads. They can be recognized by a characteristic green birefringence when stained with Congo red under polarized light.[183, 184]

Table 4. Several of human diseases associated with formation of amyloid fibrils.[183]

Disease	Involved Protein	Residues	Tissue
Alzheimer's Disease	amyloid β	40 or 42	brain
Spongiform Encephalopathy	prion	253	brain
Parkinson's Disease	α-synuclein	140	brain
Amyotrophic Lateral Sclerosis	superoxide dismutase 1	153	motor neurons
AL Amyloidosis	immunoglobulin light chain	90	systemic
Lysozyme Amyloidosis	lysozyme	130	systemic
Fibrinogen Amyloidosis	fibrinogen	27-81	kidneys
Type II Diabetes	amylin	37	pancreas
Thyroid Carcinoma	calcitonin	32	thyroid gland
Cataract	γ-crystallins	variable	eye
Aortic Amyloidoses	medin	50	aorta
Atrial Amyloidosis	atrial natriuretic factor	28	heart
Cutaneous Lichen Amyloidosis	keratins	variable	skin

Amyloid fibrils damage living organisms by several distinct mechanisms. They can physically disrupt tissues, cause organ damage and inflammatory responses, and deplete key components of the protein homeostasis. Recent studies show that already the oligomeric species generated in the process of aggregation are responsible for most of the cytotoxicity. These "smaller fibrils" can cause mitochondrial damage, trigger the production of reactive oxygen species, activate the apoptotic pathways, or interact with cell surface receptors.[185, 186] However, amyloids can also carry out normal physiological functions. For example, they mediate the movement and interactions of prokaryotes with inert surfaces,[187, 188] or they can participate in melanin production in mammalian cells.[189] Their controlled macromolecular assembly can be utilized in nanobiotechnology and advanced nanomaterials.[190, 191]

Amyloid fibrils are usually 7 – 13 nm thick and several microns long. Mature fibrils consist of several protofilaments that can twist around each other. The core structure is often similar even for different proteins. So called cross-β structure comprises of β-strands oriented perpendicular to, and β-sheets oriented in parallel to the fibril axis. The X-ray diffraction is characterized by an intense meridional reflection at 4.7 Å giving the mean separation of the hydrogen bonded β-strands, a less intense meridional reflection at 2 Å, and an equatorial reflection at 10 Å representing the spacing of β-sheets (**Figure 15**).[192]

Partial misfolding of amyloidogenic proteins into fibril precursors can be facilitated by protein mutations, post-translational or chemical modifications, or environmental conditions.[193] In most cases, these pathological aggregates are recognized and eliminated by organism's own reparatory mechanisms. A disease occurs if the aggregation rate is higher than the reparatory rate. This is frequent in hereditary diseases where a specific protein mutation increases its aggregation propensity. In prion diseases, the growth of amyloids is speeded up by pre-formed aggregates. In other cases it was connected to age-related decline of chaperone and ubiquitin/proteasome activity.[183]

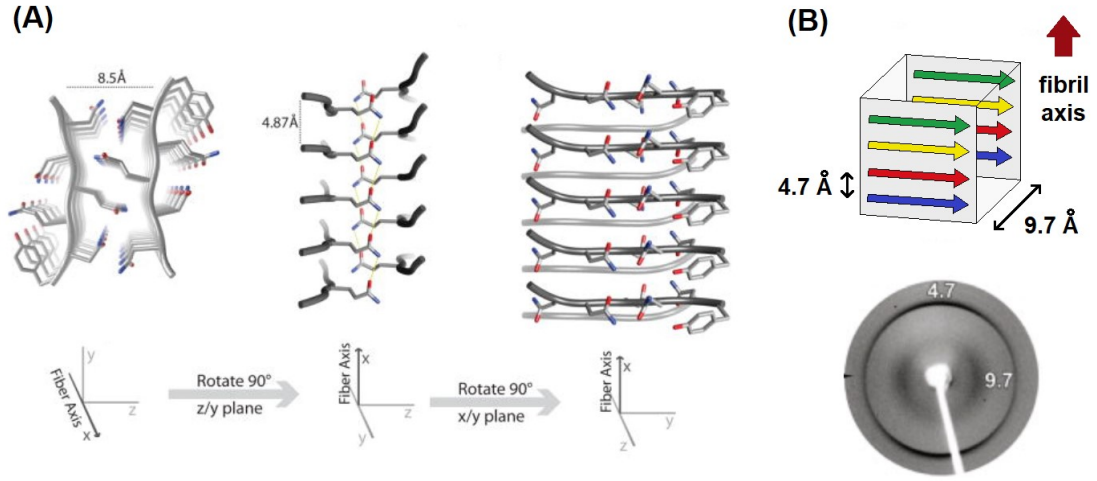

Figure 15. Amyloid fibrils: **(A)** An X-ray structure of GNQQNY peptide fibrils. An interdigitation of the side chains from neighboring β-sheet strands is visible, stabilized by hydrophobic interactions and hydrogen bonds.[194] **(B)** A fiber diffraction pattern showing a meridional reflection at 4.7 Å and an equatorial reflection at ~10 Å, and its connection to the structure.[195]

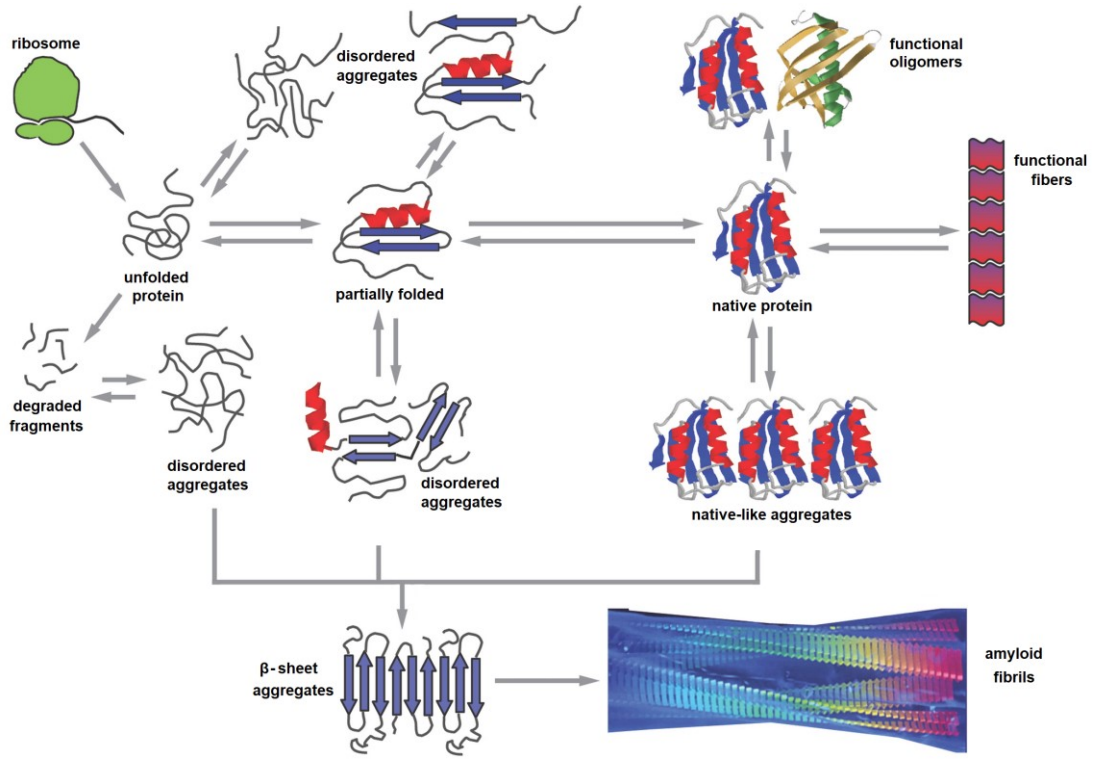

Figure 16. Conformational states adopted by a polypeptide chain.[183] A protein after its synthesis acquires its native state through a partially folded intermediate. Many "unwanted" aggregates can be formed, including amyloid fibrils characterized by a high β-sheet content.

Protein aggregation into amyloid fibrils usually starts with a partially folded intermediate (**Figure 16**). Hydrophobic protein surface facilitates the process. The *β*-sheet structure can also be stabilized by hydrogen bonds between polar amino acid residues, such as glutamine or asparagine (a polar zipper). When the oligomeric intermediates are formed (typically within hours), further fibril growth is rather fast (minutes), followed by a maturation which can last several days. **Figure 17** shows transmission electron microscopy (TEM) images of amyloid fibrils grown *in vitro* from the amyloid-*β* peptide after different incubation periods. The formation of oligomeric species clearly precedes the aggregation to fibrils. Of course, *in vivo* processes are much more complicated.

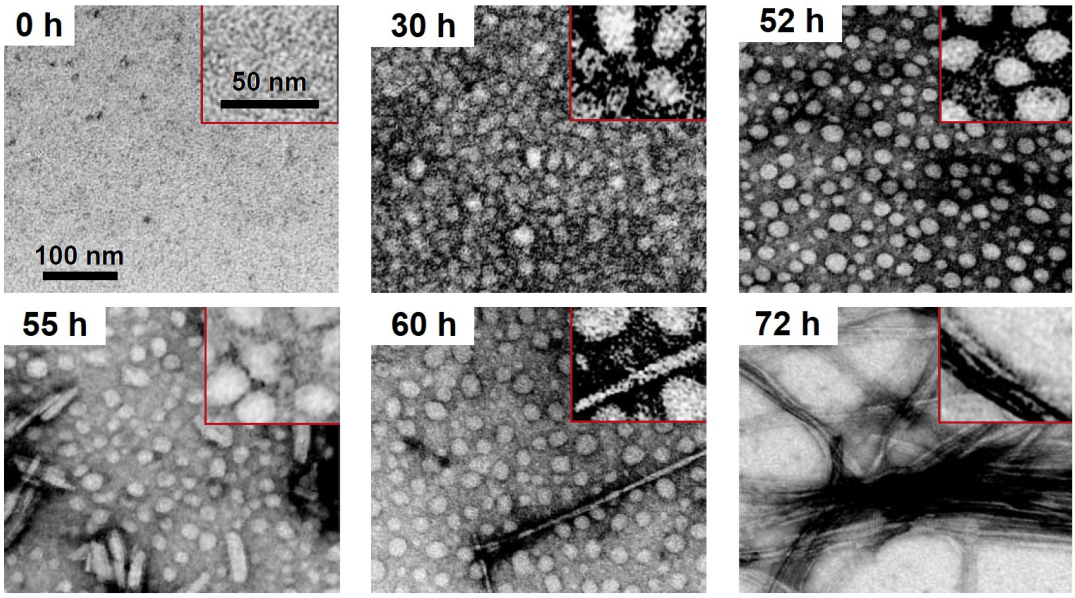

Figure 17. Morphology of amyloid-*β* fibrils grown *in vitro* after different incubation periods. At 30 hours we see spherical intermediates, at 60 hours first protofibrils can be observed. After the formation of protofilaments, mature amyloid fibrils grow within ~10 hours.[196]

The *in vitro* kinetics of amyloid fibril formation is described by a sigmoidal curve with a lag phase, an elongation and a saturation phases (**Figure 18**). In the first phase, proteins change conformation and form oligomeric nuclei. This is a stochastic process depending on experimental conditions. It can take anything from several minutes to several hours. The oligomers act as seeds for protofibril formation; this process is characterized by a fast elongation. At the end, protofibrils assemble to

mature amyloid fibrils.[197, 198] The fibril growth can be made faster by so called seeding procedures,[199-201] in which pre-formed fibrils are added to native protein solutions. This significantly reduces the preparation time. Protocols for *in vitro* fibril formation usually involve a mild denaturation of proteins by high temperatures, pH change, addition of salts or metals, etc. After that, the preparation usually includes a prolonged incubation of proteins at high temperatures. Fibril growth *in vitro* is generally dependent on protein concentration, pH, ionic strength, presence of various additives, and temperature of incubation, and these experimental conditions need to be optimized for each protein.

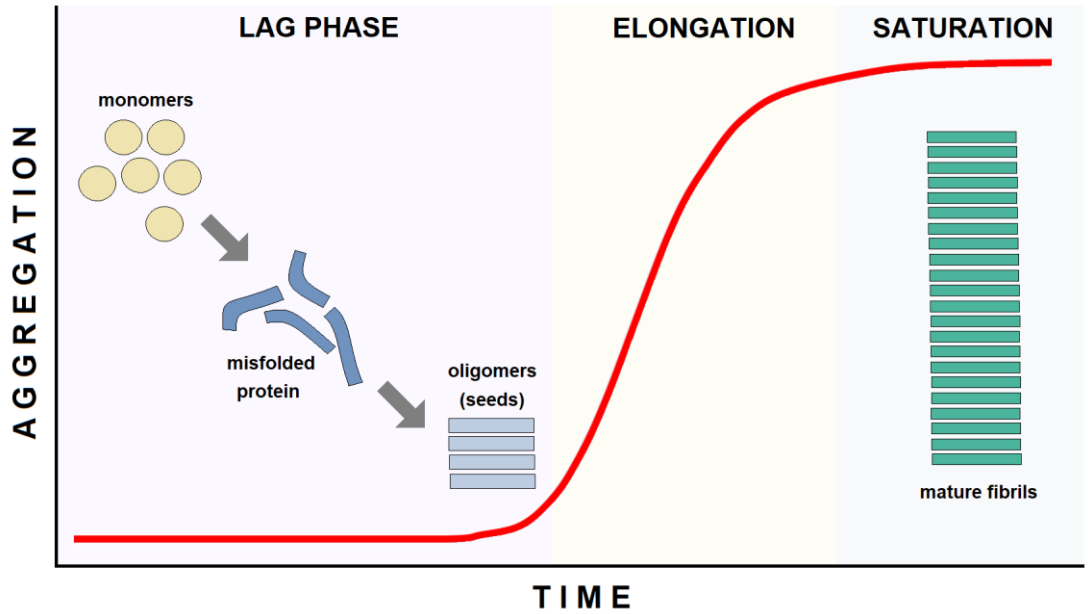

Figure 18. Nucleation mechanism of the fibril growth characterized by a sigmoidal kinetic curve with three distinct stages – a stochastic lag phase, a rapid elongation phase and a saturation phase corresponding to the maturation of amyloid fibrils.

Due to fibril chirality, chiroptical spectroscopic techniques provide unique insight into the fibril properties. In our work, we employed vibrational circular dichroism and induced lanthanide circularly polarized luminescence since both methods are sensitive to the amyloid structure. However, while VCD also reflects the supramolecular arrangement, the CPL senses the structure more locally. The results presented in this section were published in two original papers: *Induced Lanthanide*

Circularly Polarized Luminescence as a Probe of Protein Fibrils (Krupová, M.; Kapitán, J.; Bouř, P.: ACS Omega 2019, 4(1), p. 1265-1271), and *Polymorphism of Amyloid Fibrils Induced by Calatytic Seeding: A Vibrational Circular Dichroism Study* (Krupová, M.; Kessler, J.; Bouř, P.: ChemPhysChem 2021, 22(1), p. 83-91), attached in **Attachments B** and **C**.

2.1. Methods

2.1.1. Preparation of fibrils

In our experiments, we grew amyloid fibrils from *L*- and *D*-enantiomers of polyglutamic acid (PGA; MW 15 – 50 kDa), hen egg-white lysozyme (HEWL) and human recombinant insulin (INS). All of the proteins were purchased from *Sigma-Aldrich*. To avoid the interference of water signal in the frequency region of interest (1500 – 1800 cm^{-1}) in IR and VCD measurements, the proteins were repeatedly dissolved in D_2O and lyophilized. For IR and VCD, D_2O was used as a solvent, pD (used without a correction to pH) was adjusted by NaOD and DCl. For other experiments H_2O, HCl and NaOH were used.

Table 5. Experimental conditions used to grow amyloid fibrils from three proteins.

Exp. Condition	PGA	HEWL	INS
Protein concentration (mg/mL)	10 or 15	100	40
pH[A]	4.3	2.0	2.0
Incubation temperature (°C)	65	60	60
Incubation time (h)	48	48	24
Solvent	H_2O / D_2O	H_2O / D_2O	H_2O / D_2O

A HCl and NaOH (DCl and NaOD in D_2O) were used for pH adjustment.

For lysozyme, the protein was dissolved in H_2O at 100 mg/mL concentration and acidified with 1M HCl to pH 2. After that, the solutions were incubated at 60 °C for 48 hours. For insulin, the aqueous solution of the protein at concentration 40 mg/mL was also acidified by 1M HCl to pH 2, and incubated at 65 °C for 24 hours. For PGA, the concentration was 15 mg/mL (10 mg/mL for some experiments) and pH 4.3. The acidified solutions were then incubated at 65 °C for 48 hours. The overview of the conditions used for all of the proteins is listed in **Table 5**. The seeds were prepared by ultrasonication of mature fibril solutions for 1 hour, and then added to the starting protein solutions in the 1 : 9 seed to protein ratio.

2.1.2. Transmission Electron Microscopy Imaging

For verification of fibril growth, we used transmission electron microscopy imaging. The solutions with mature amyloid fibrils were diluted by water 10× (PGA, INS) or 100× (HEWL) while maintaining the pH at 2 (HEWL, INS) or 4.3 (PGA), then 10 μL of the solution were deposited on a carbon-coated grid and stained with 4 % (w/w) phosphotungstic acid. The TEM imaging was performed with a *JEOL JEM-1200EX* microscope.

2.1.3. Fluorescence Measurements

A fluorescence assay with thioflavin-T (ThT) is often used for detection and kinetics of amyloidal fibril growth. For ThT fluorescence assay, 5 μL of the native protein or fibrils solution were mixed with 1 mL of 50μM ThT solution and put into a quartz fluorescence cell. The spectra were measured on *FluoroMax-4* spectrometer (*Horiba*) with 440 nm excitation wavelength, with slit width 5 nm for both the excitation and emission, and 0.2 nm increments. Kinetics of fibril formation was monitored using a *Spark* microplate reader (*Tecan*). The acidified protein solutions were mixed with a small volume of ThT (final concentration of ThT 30 μM) and put to a 384-well plate with transparent bottom ("Nunc", *Thermo Fisher Scientific*, ref# 242764). The amount of fibrillated protein was monitored by ThT fluorescence using 440 nm excitation (slit 5 nm) and 480 emission (slit 20 nm). The intensity of

fluorescence was measured every 5 min over 70 hours, preceded by a 15s shaking (90 rpm). During the measurement, the sample compartment was heated to 42 °C.

2.1.4. Vibrational spectra

IR absorption and VCD spectra were measured with *Chiral IR-2X* instrument (*BioTools, Inc.*). The concentration of individual protein solutions was specified in **Table 5**. Either a BaF_2 or CaF_2 cell was used (specified in the text) with 50 μm (PGA) or 15 μm (INS and HEWL) pathlength, 4 cm diameter, teflon spacer and 8 cm^{-1} resolution. For fibrils, usually 6 blocks of 2048 scans were collected (2 h of total accumulation time) and the cell was rotated during the measurement. Spectra of D_2O were subtracted as a baseline.

For non-aggregated proteins, the concentration of PGA was 45 mg/mL to increase VCD signal to noise ratio. The concentration of HEWL and INS was kept the same as for fibrils; the pathlength was 25 μm. Lysozyme and PGA were dissolved in D_2O and measured. For insulin, pD was changed prior to the measurements to 2 to increase its solubility. The spectra for the non-aggregated proteins were accumulated for 16 h. The experiments involving seeding were performed at least three times and the average is reported. Fibrils in each of the triplicates were prepared and measured separately.

2.1.5. Induced CPL spectra

For induced CPL measurements, 100 μL of protein solutions were mixed with 10 μL of 10mM $EuCl_3$ or $Na_3[Eu(DPA)_3]$ (DPA = pyridine-2,6-dicarboxylic acid), so that the final concentration of the europium compounds was 1 mM. The TL and CPL spectra were measured with *ChiralRaman-2X* instrument (*BioTools, Inc.*) with 532 nm laser excitation, 200 mW laser power and about 20 min acquisition. Normalization of the TL/Raman signal to the same conditions was done for better spectra comparison. Measurements in the broader range with different polarization setups were done with an ROA instrument built in Palacký University (Olomouc) according to the design of Hug[24, 108] and Nafie.[202]

Conventionally, ROA is defined as $I_R - I_L$ while CPL is defined as $I_L - I_R$ (where I_L and I_R refers to left- and right-circularly polarized light, respectively). Since we used Raman optical activity instrument to record the CPL spectra, we use the definition $I_R - I_L$ even for CPL. In CPL, a dissymmetry factor $g = 2(I_L - I_R)/(I_R + I_L)$ is usually used as a measure of relative CPL intensity. Instead, we use $CID = (I_R - I_L)/(I_R + I_L)$ which is conventional for ROA. In this case, the relation between *CID* and *g* is: $CID = -g/2$. Moreover, we measure the Raman shifts in ROA / CPL experiment in wavenumbers. This can be converted to emission wavelength by eq. 40 ($\Delta\tilde{\nu}$ is Raman shift in cm^{-1}, λ_0 is excitation wavelength (λ_0 = 532 nm) and λ_1 is emission wavelength in nm).

$$\Delta\tilde{\nu}(cm^{-1}) = \left(\frac{1}{\lambda_0\,(nm)} - \frac{1}{\lambda_1\,(nm)}\right) \cdot 10^7 \tag{40}$$

2.2. Results and Discussion

In this work, we prepared amyloid fibrils from four proteins: hen egg-white lysozyme, human recombinant insulin, and *L*- and *D*-enantiomer of polyglutamic acid. The fibrils formed by these proteins are shown in **Figure 19**.

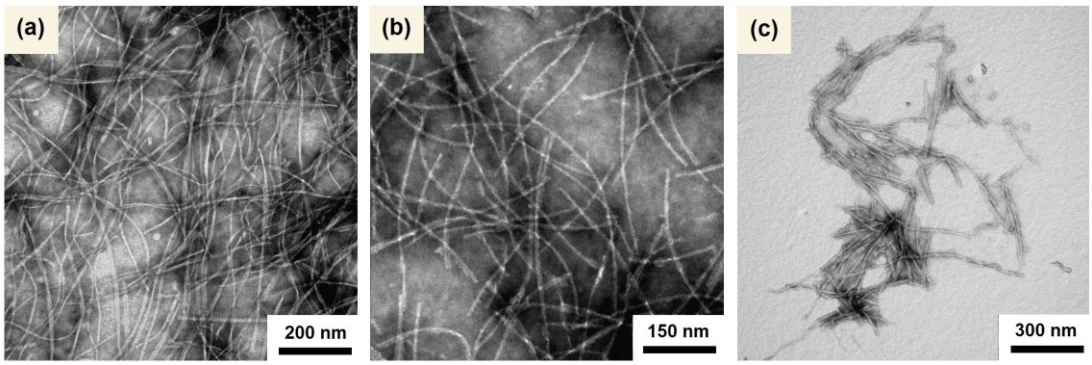

Figure 19. TEM images of selected fibril types. **(a)** INS fibrils; quite long and well formed filaments occasionally forming a ribbon-like structures. **(b)** HEWL fibrils; long and thick single filaments. **(c)** PLGA fibrils; shorter filaments.

Even though the spectroscopic methods can not provide atomic resolution, they are simple and versatile, and provide a valuable insight into the properties of amyloid fibrils. They include electronic spectroscopy, such as fluorescence assays based on the interaction between fibrils and fluorescent dye thioflavin-T. Also, the vibrational spectroscopy such as IR absorption and Raman scattering provides information on the secondary structure.[203] However, they are not sensitive to supramolecular geometry, which can be overcome by using the chiroptical methods, such as vibrational circular dichroism or circularly polarized luminescence.

2.2.1. Thioflavin-T Fluorescence Assay

Thioflavin-T is a benzothiazole used as a fluorescent dye for the detection of amyloid fibrils (**Figure 20**). Upon binding to the fibrils, ThT exhibits a shift of the excitation maximum from 385 nm to 450 nm. Similarly, the emission maximum changes from 445 nm to 482 nm. These shifts are accompanied by a several orders of magnitude increase of the fluorescence intensity.

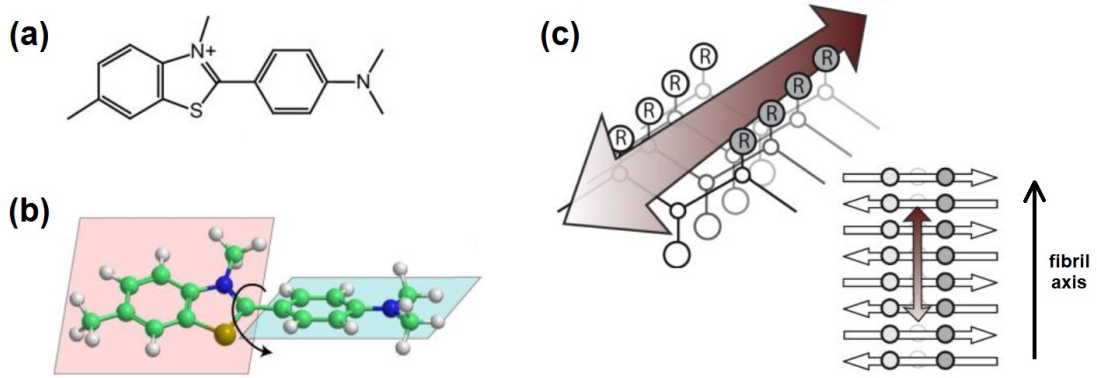

Figure 20. Structure of thioflavin-T **(a, b)**, and a model of its binding to the fibrils (**c**, ThT molecule is depicted as a brown arrow)**.**[204]

Thioflavin-T is a highly specific and easy to use probe for the presence of fibrils in solutions.[205] Rotation of ThT along the bond connecting the benzylamine and benzathiole rings quenches the excited states. When bound to amyloid fibrils, the rotation stops, leading to a high quantum yield of the fluorescence.[204] The interaction

between ThT and protein depends on the experimental conditions. Highly charged fibrils in low pH generally exhibit the lowest affinity to the dye.[206]

Fluorescence spectra of lysozyme monomer and fibrils are reported in **Figure 21a**. When ThT binds to fibrils, its fluorescence intensity with maximum at 483 nm grows by about 8 times when compared to monomer spectra. ThT kinetics assay (**Figure 21b**) shows that fibrils begin to appear in the solution on average after 25 hours, even though as long as 50 h lag phase can be sometimes observed. This is in agreement with the stochastic nucleation mechanism preceding the fast-growing stage of amyloid formation.

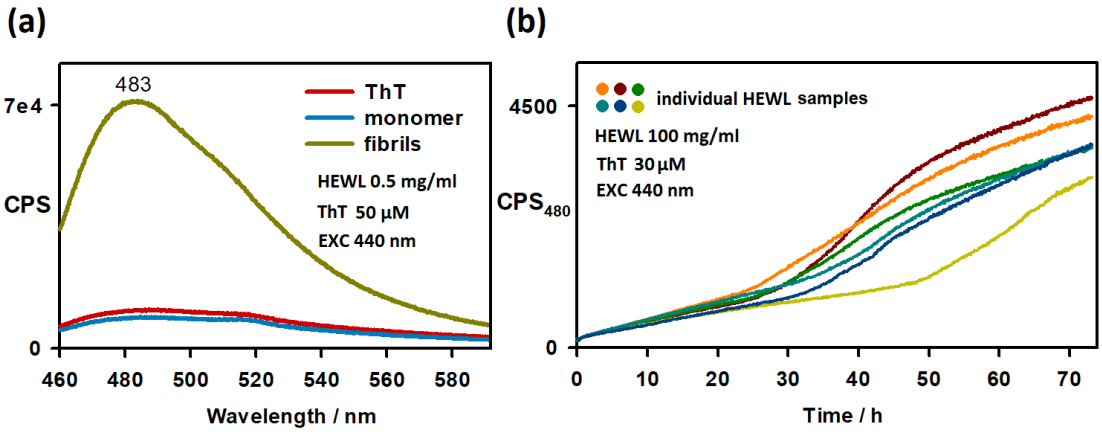

Figure 21. (a) Fluorescence spectra of ThT, HEWL monomer and HEWL fibrils. **(b)** ThT kinetics assay showing the dependence of ThT fluorescence at 480 nm on time of incubation. The fluorescence intensity is expressed in CPS (counts per second).

2.2.2. Vibrational Circular Dichroism

The potential of VCD for fibril research was recognized in mid-2000s.[207] Some amyloid fibrils provided a signal in the amide I region up to 100× bigger that other proteins.[167] Moreover, the signal was dependent on the experimental conditions and reflected macroscopic fibril morphology.[208-210] VCD spectra of monomeric and fibrillated hen egg-white lysozyme and insulin (**Figure 22** and **23**) both show a remarkable sensitivity to fibril formation. Monomeric VCD spectra suggest that the secondary structure of HEWL has significant content of α-helix, while large content

of random coil / β-sheet is seen for INS. The experimental g-factors are within the usual range: ~2×10^{-5} for HEWL and ~4×10^{-5} for INS.

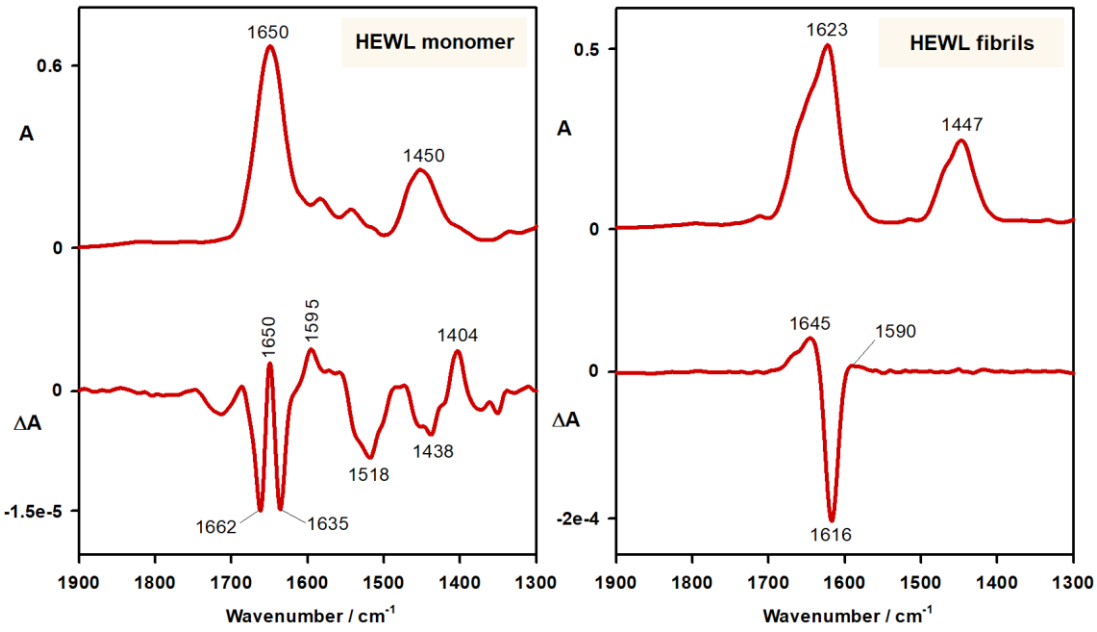

Figure 22. IR absorption and VCD spectra of monomeric (left) and fibrillar (right) HEWL in D_2O (CaF_2 cell) .

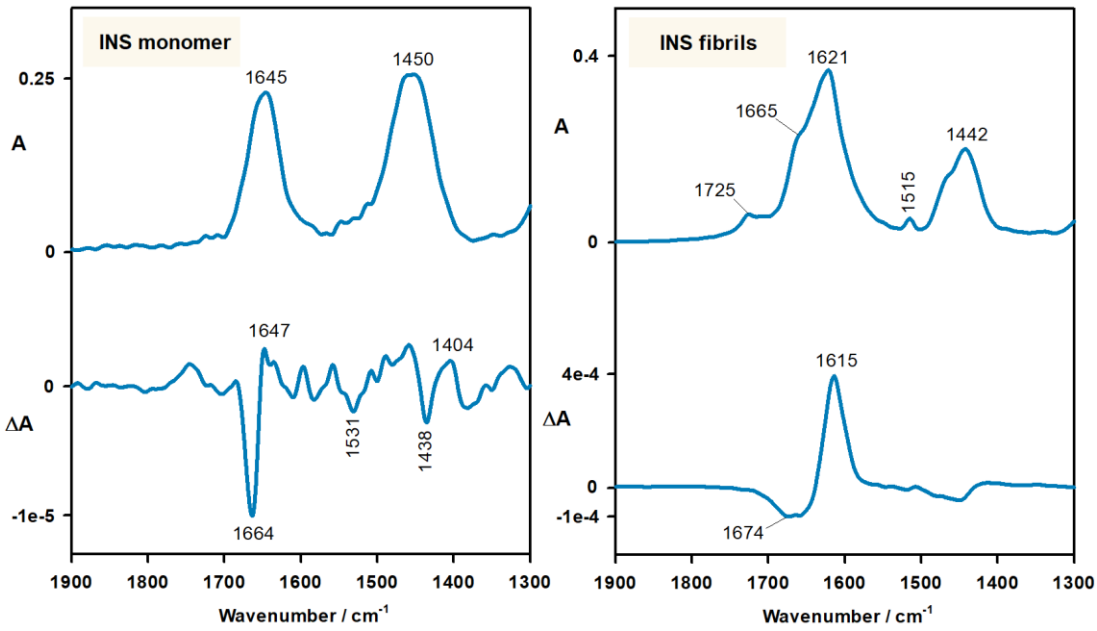

Figure 23. IR absorption and VCD spectra of monomeric (left) and fibrillar (right) insulin in D_2O (CaF_2 cell).

After the fibrils are formed, IR spectra of both proteins show a splitting of amide I' band (the apostrophe in amide I' etc. indicates a deuterated sample) into a maximum at ~1623 cm^{-1} and a shoulder at ~1665 cm^{-1}, which indicates a high β-sheet content. VCD spectra are changed more. For HEWL, a (+/-/+) VCD with a negative maximum at 1616 cm^{-1} can be observed. Insulin fibril VCD is dominated by a broader positive signal at 1615 cm^{-1} with a prominent negative shoulder at 1674 cm^{-1}. The *g*-factors are much higher, 4×10^{-4} for HEWL and 11×10^{-4} for insulin.

VCD of non-isotropic samples, e.g. in some cases fibrils, is prone to artifacts. Therefore, one needs to assess the reliability of the observed signals. Several criteria should be considered: (a) two enantiomeric molecules should provide "mirror-image" VCD spectra; (b) racemic mixture of enantiomers should not produce a VCD signal; (c) linear dichroism should be measured simultaneously to estimate its contribution the to measured signal; (d) the effect of sample orientational artifacts can be estimated by cell rotation; and (e) a VCD peak should be accompanied by an absorption peak in the IR spectrum at the same / close wavenumbers.[211] The (a) and (b) criteria usually can not be applied due to the absence of other protein enantiomer. However, for some simple polypeptides such as polyglutamic acid, it is possible.

VCD spectra of monomeric and fibrillar *L*- and *D*-polyglutamic acids are plotted in **Figure 24**. In IR spectra of monomers (left), two C=O stretching bands are present: the amide I' vibration at 1648 cm^{-1} and an out-of-phase vibration of the COO^- at 1566 cm^{-1}. The two other bands belong to amide II' vibration (1447 cm^{-1}) and in phase COO^- C=O stretching (1407 cm^{-1}). In VCD spectra, a prominent couplet centered at ~1655 cm^{-1} has an opposite sign for two enantiomers; (+/–) for PLGA and (–/+) for PDGA. The IR and VCD shapes indicate that the monomers exist in a disordered conformation, partially adopting a polyproline-II helix.[212] In the fibril spectra, the C=O stretching vibration in COOD of the side chains produces an IR band at 1730 cm^{-1} connected to the VCD couplet at 1740(-)/1725(+) cm^{-1} (for PLGA). This band is present only in the spectra of fibrils due to the protonation of carboxylic groups in lower pH.

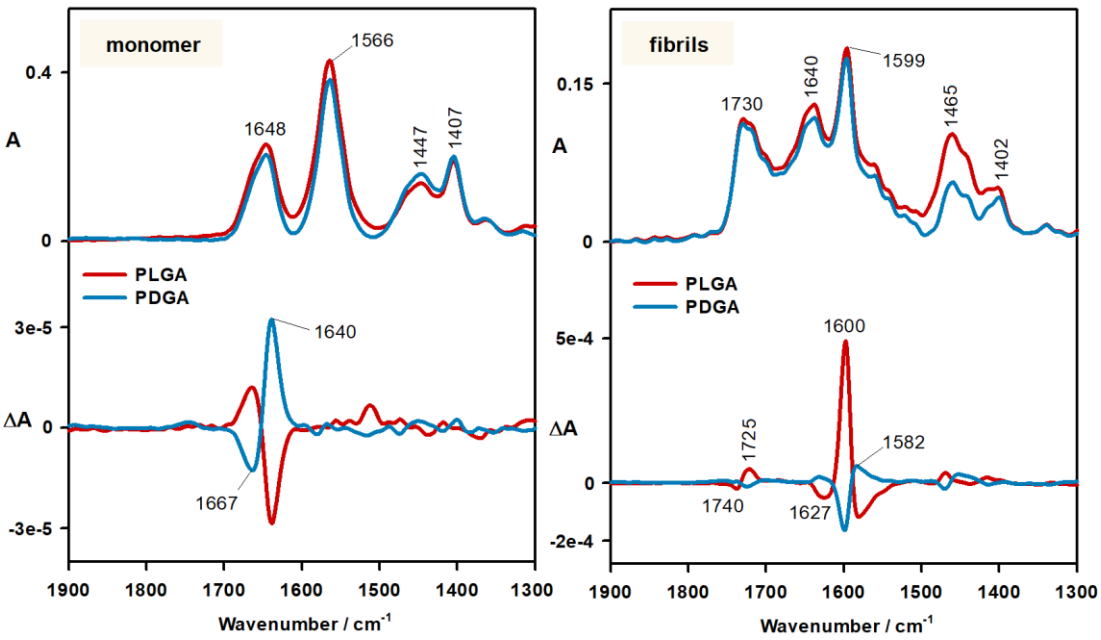

Figure 24. IR absorption and VCD spectra of monomeric *L*- and *D*-polyglutamic acid (15 mg/mL, CaF_2 cell).

The amide I' vibration produces two IR bands at 1640 and 1599 cm^{-1} that are coming from variously polarized β-sheet modes.[213-215] The strongest VCD band is located at 1600 cm^{-1} and is positive for PLGA and negative for PDGA. The amide II' vibration produces several IR bands (1465 cm^{-1} with a shoulder at 1450 cm^{-1}, and 1402 cm^{-1}) with relatively weak VCD. In comparison with PLGA fibrils (*g*-factor ~30×10^{-4}), the intensity of PDGA fibrils ($g = 10\times10^{-4}$) VCD is about 3x lower, which may be caused by differences in molecular weight distribution in commercial samples.[216]

Due to high intensities of amyloid fibrils' VCD, lower measurement times are sufficient. This also enables to follow the kinetics of amyloid fibril formation as shown in **Figure 25** for the PLGA fibrils grown in the BaF_2 cell catalyzed by a spatial confinement[217] and monitored by increasing intensity of the main VCD band at 1600 cm^{-1}. The origin of enhanced VCD in amyloid fibrils is believed to be connected to the long-range coupling of chromophores in the periodic structure. Various computational approaches were used in the past to connect the VCD spectral pattern to the structure of fibrils. One of the most promising is a transition dipole coupling (TDC) model, in which the amide chromophores are represented by point dipoles.[214, 215, 218] All-atomic

ab initio calculations based on the density functional theory (DFT) are practical only for systems with up to several hundreds of atoms,[219-221] therefore fragmentation methods such as Cartesian-coordinate based tensor transfer (CCT)[162, 213] or CCT combined with TDC[222] are needed to calculate extensive fibril structures with DFT computations.

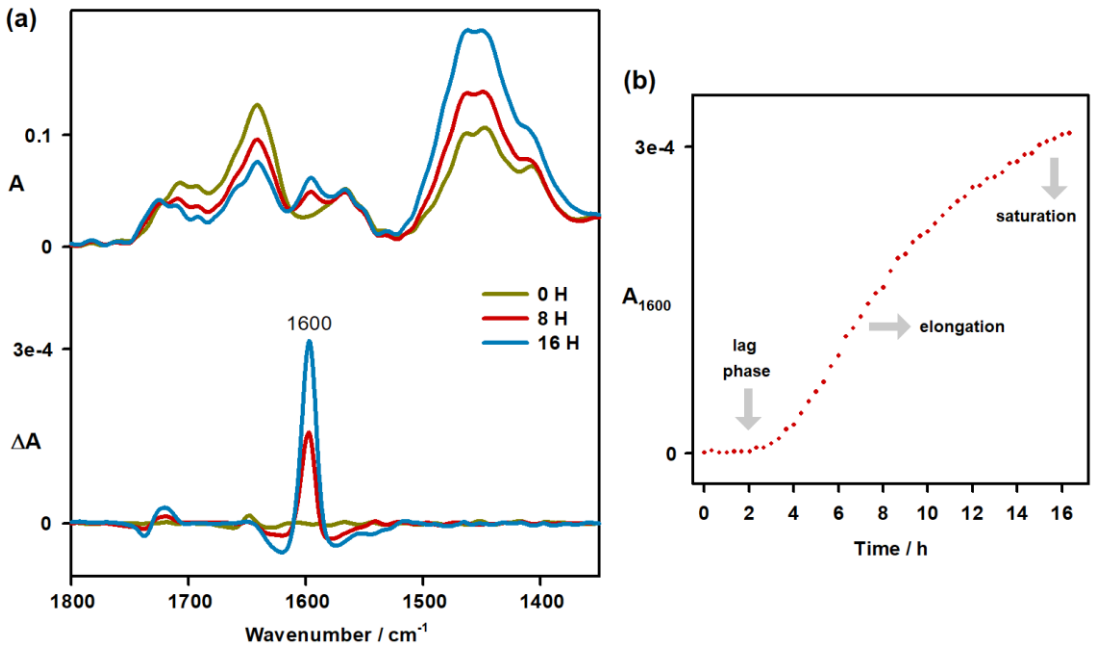

Figure 25. Kinetics of PLGA fibril growth monitored by VCD. **(a)** IR and VCD spectra of PLGA fibrils (10 mg/mL) grown directly in a BaF_2 IR cell at 0, 8 and 16 hours. **(b)** Kinetic curve illustrating growth of PLGA fibrils catalyzed by a spacial confinement in the BaF_2 cell plotted as a VCD intensity at 1600 cm^{-1} over time of the spectra acquisition.

To understand the relation of VCD signal to the fibril structure, we used a combined DFT/TDC approach. A model fibril based on the polyglutamic acid crystal β_2 structure[216, 223, 224] consisted of four amino acid chains in the three parallel β-sheets, which were then stacked. The repeating elementary unit comprised of 24 amino acid residues. A dependence of VCD spectra on the twist (**Figure 26**) and length (**Figure 27**) of a model fibril is shown.

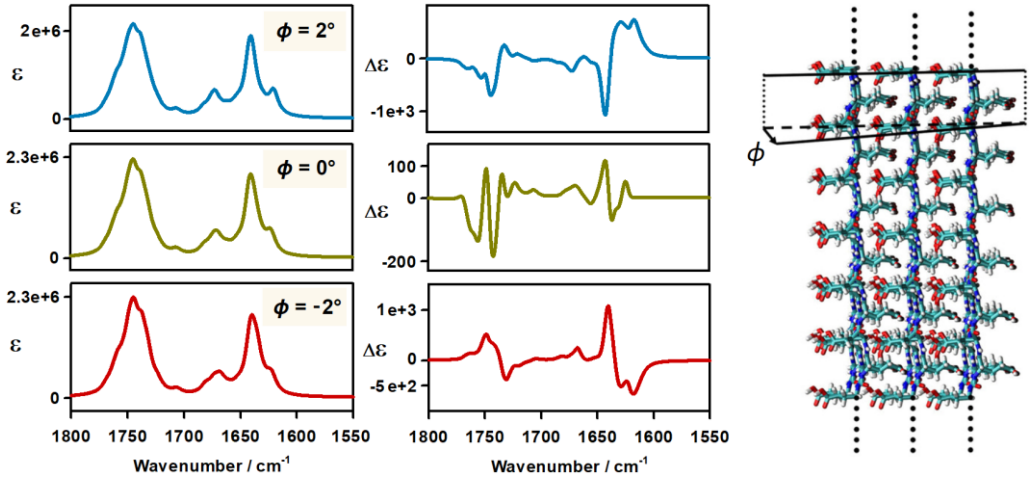

Figure 26. IR absorption and VCD spectra of PLGA fibrils simulated for three values of the twist angle ϕ. The length of the model fibril was kept constant (N = 135; N is the number of elementary units of the fibril structure marked on the left).

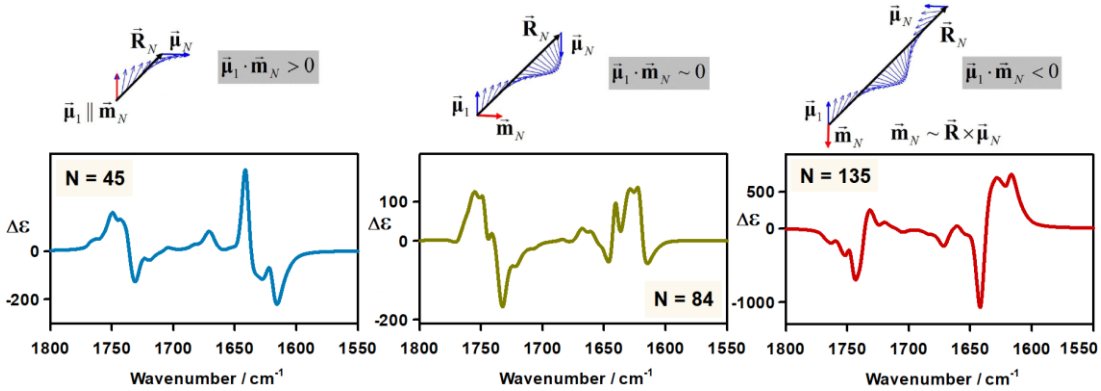

Figure 27. Simulated dependence of VCD spectra of PLGA fibrils on the length of a thread for a constant twist ϕ = 2°. N is the number of two amide elementary units; therefore, N = 45 corresponds to the total twist of 90° between amide groups at the beginning and at the end of the filament, etc. Also, the transition dipole moments ($\boldsymbol{\mu}_1$, $\boldsymbol{\mu}_N$) providing the most distinct values of rotational strength (the distance vector $\mathbf{R}_N$) are illustrated on the right. In case of N = 45 when the dipole moments are perpendicular, the rotational strength is positive. For parallel $\boldsymbol{\mu}_1$ and $\boldsymbol{\mu}_N$ ($N \approx 84$), the rotational strength is close to zero. In case of $N \approx 135$ and perpendicular dipole moments, the rotational strength is negative.

While IR absorption spectra do not significantly depend on the twist, VCD signal for twist ϕ = 2° and ϕ = -2° between two neighboring amides gives approximately an opposite sign. A sign dependence of VCD signal was observed also

when the length of a model fibril was varied. This is explained by a constructive and destructive coupling of the dipoles connected to the repetition of VCD patterns after certain length (**Figure 27**). For more details on the calculations, please refer to Krupová et al.: *Polymorphism of Amyloid Fibrils Induced by Catalytic Seeding: A Vibrational Circular Dichroism Study*.

2.2.3. Circularly Polarized Luminescence of Ln^{3+} Luminophores

In our experiments, we measured circularly polarized luminescence induced in two luminescent probes: Eu^{3+} ion introduced as $EuCl_3$, or a non-chiral complex $Na_3[Eu(DPA)_3]$ (DPA = pyridine-2,6-dicarboxylic acid). In each probe the chirality is induced in a different way. The association of Eu^{3+} ion and a chiral molecule results in the formation of a chiral complex. The chirality in $[Eu(DPA)_3]^{3-}$ is connected to a preferred helical twist of the ligands: in a plain solution, a dynamic mixture of two conformations (Δ and Λ) exists. An addition of a chiral molecule can perturb this equilibrium and favor one conformation (**Figure 28**).[139]

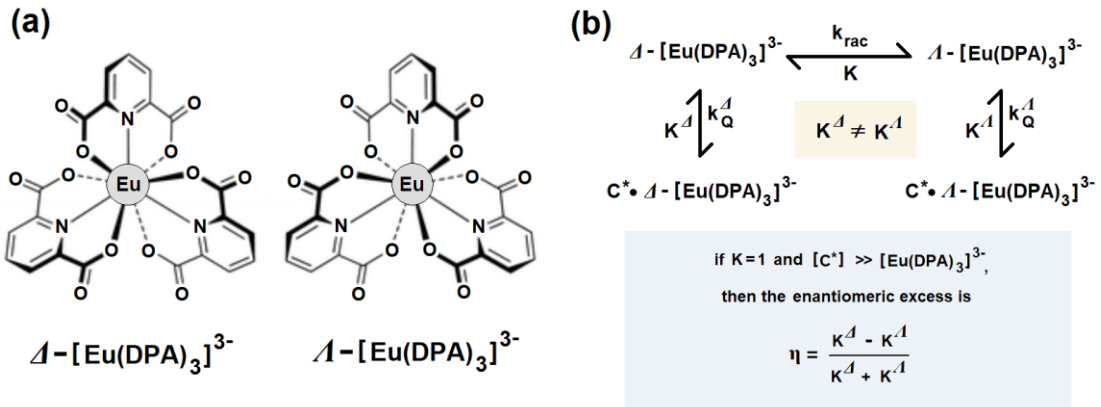

Figure 28. The principle of chirality sensing with $Na_3[Eu(DPA)_3]$. **(a)** $[Eu(DPA)_3]^{3-}$ is an anionic tris-chelate complex of D_3 symmetry. Two helical-like arrangements of chelate rings around the Eu^{3+} centre are possible, giving rise to the Λ- and Δ-enantiomers. **(b)** When interacting with a chiral species C*, the dissociation constants of the C* • $[Eu(DPA)_3]^{3-}$ adduct for each enantiomer (K^{Δ} and K^{Λ}) differ, and one enantiomer prevails. The enantiomeric excess η is related to these constants.[139]

The interaction between Eu^{3+} and a protein is driven by electrostatic forces. Therefore, an Eu^{3+} ion can be used to detect the PGA fibrils but it does not interact with positively charged lysozyme and insulin at low pH. On the other hand, anionic complex $[Eu(DPA)_3]^{3-}$ interacts strongly with lysozyme and insulin, and not with polyglutamic acid. In **Figure 29**, circularly polarized luminescence spectra of Eu^{3+}/PGA are plotted. On the left, the total luminescence and CPL of PLGA was measured at 0, 24 and 48 hours from the beginning of incubation. A sharp and intense band at 1535 cm^{-1} (579 nm) corresponding to the $^5D_0 \rightarrow {}^7F_0$ transition (see **Table 6**) does not provide any measurable CPL. On the other hand, a broad TL band at 1915 cm^{-1} (592 nm) corresponding to the $^5D_0 \rightarrow {}^7F_1$ transition provides a very strong CPL (CID ~ 3×10^{-2}), shape of which is highly dependent on the PGA conformation and its changes during the fibril growth and maturation. The TL spectra show only minor changes as fibrils grow; the two shoulders of the main TL band at 1960 and 1790 cm^{-1} disapper, while the shoulder at 1870 cm^{-1} becomes more prominent. Fibrils grown from two enantiomers of PGA exhibit a mirror-image CPL with only slight variations in intensity that can be attributed to experimental error.

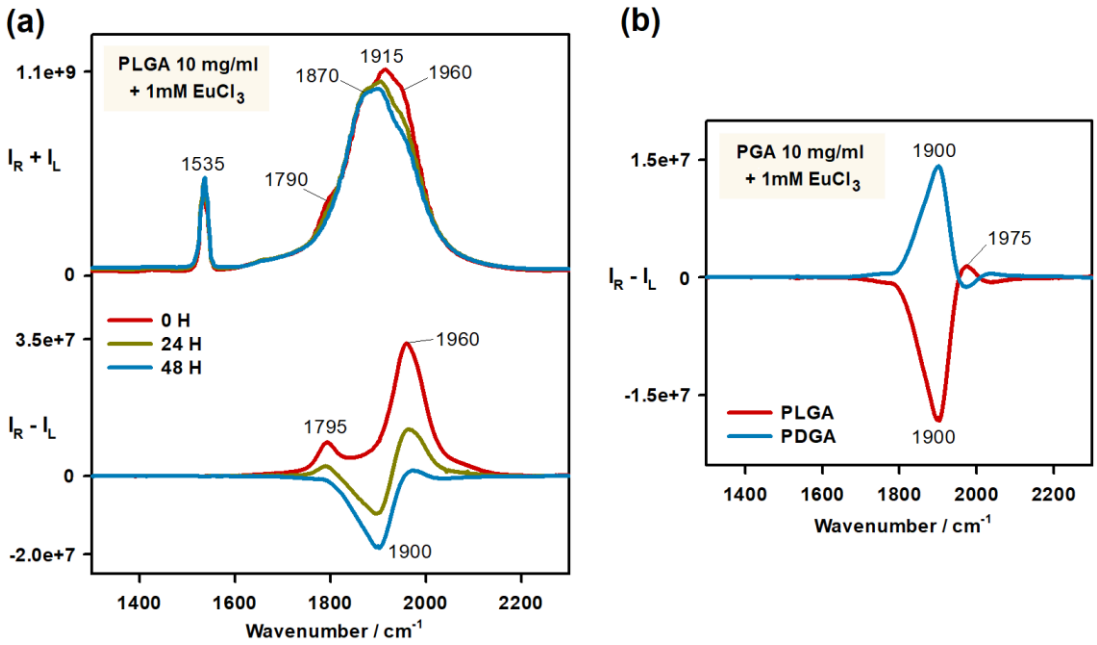

Figure 29. TL and CPL spectra of $EuCl_3$ mixed with PGA fibrils. **(a)** Time dependence for PLGA. **(b)** CPL of the PGA fibril enantiomers.

Table 6. Transitions observed in Eu^{3+} luminescence.[225]

Transition	Character[A]	Wavelength (nm)	Relative Intensity[B]	Remarks
$^5D_0 \rightarrow {}^7F_0$	ED	570 - 585	**vw** to **s**	only in $C_{n(v)}$ and C_S symmetry
$^5D_0 \rightarrow {}^7F_1$	MD	585 - 600	**s**	intensity not dependent on environment
$^5D_0 \rightarrow {}^7F_2$	ED	610 - 630	**s** to **vs**	very sensitive to environment
$^5D_0 \rightarrow {}^7F_3$	ED	640 - 660	**vw** to **w**	forbidden transition
$^5D_0 \rightarrow {}^7F_4$	ED	680 – 710	**m** to **s**	sensitive to environment
$^5D_0 \rightarrow {}^7F_5$	ED	740 – 770	**vw**	forbidden transition
$^5D_0 \rightarrow {}^7F_6$	ED	810 - 840	**vw** to **m**	rarely observed

A ED – electric dipole, MD – magnetic dipole. **B** vw – very weak, w – weak, m – moderate, s – strong, vs – very strong.

Anionic $[Eu(DPA)_3]^{3-}$ has a high affinity to lysozyme and insulin and produces a strong CPL signal (**Figure 30**). In TL spectra of lysozyme fibrils, two negative bands at 1877 and 1975 cm^{-1} (591 and 594 nm) belong to the $^5D_0 \rightarrow {}^7F_1$ transition. In case of insulin fibrils, only minor shifts of the maxima occur in TL (1880 and 1970 cm^{-1}, respectively). The shape of CPL is not very specific either. Depending on which enantiomer of $[Eu(DPA)_3]^{3-}$ is stabilized, we see either two negative or two positive bands at 1865 and 1975 cm^{-1} with only minor distortions. The observed CIDs are quite high; $\sim 2\times10^{-2}$ for HEWL fibrils and $\sim 2\times10^{-3}$ for INS fibrils.

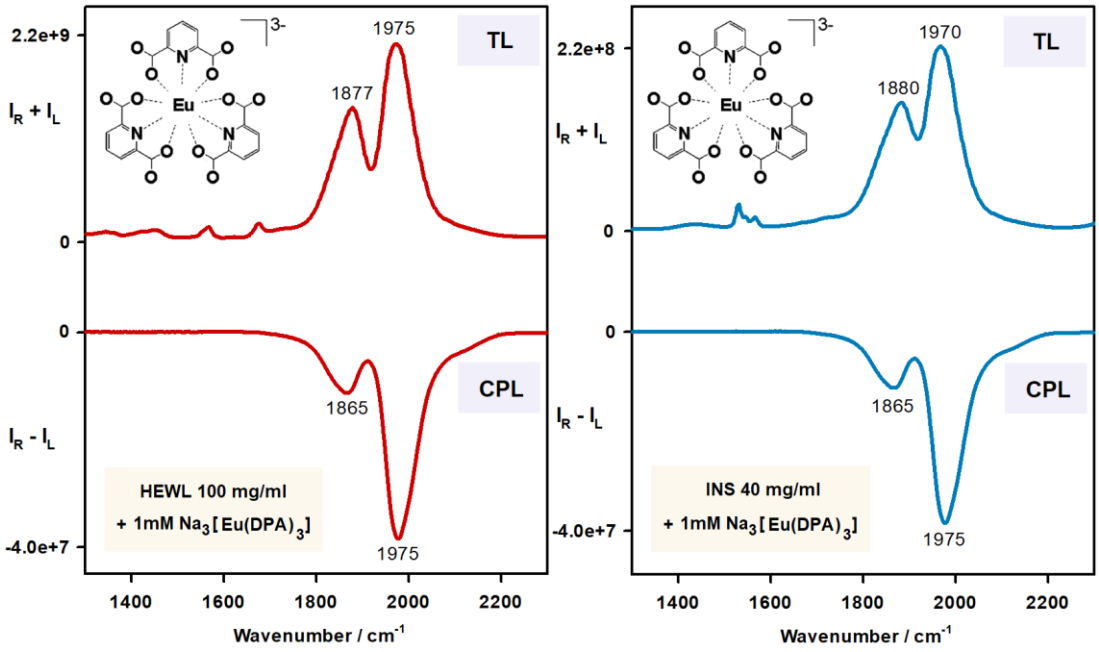

Figure 30. TL and CPL of HEWL (left) and INS (right) fibrils mixed with $Na_3[Eu(DPA_3]$.

To better understand the interaction between the protein and europium luminophore, a Job's plot[226] (dependence of CPL intensity on different HEWL / $Na_3[Eu(DPA)_3]$ molar ratios) at pH 2 and 7, as well as the dependence of induced CPL intensity of HEWL / $Na_3[Eu(DPA)_3]$ on the Eu-complex concentration is shown in **Figure 31**. Both of these plots indicate that one lysozyme molecule binds on average to up to 3 $[Eu(DPA)_3]^{3-}$ ions at pH 2, and 1.5 ions at pH 7. This confirms the importance of protein charge for the interaction (calculated as +8 at pH 7 and +18 at pH 2). Although the interaction between the protein and europium-complex may be more complicated, a simple model considering the electrostatic potential of a protein is able to explain well the variable affinity of Eu-luminophores to different proteins.

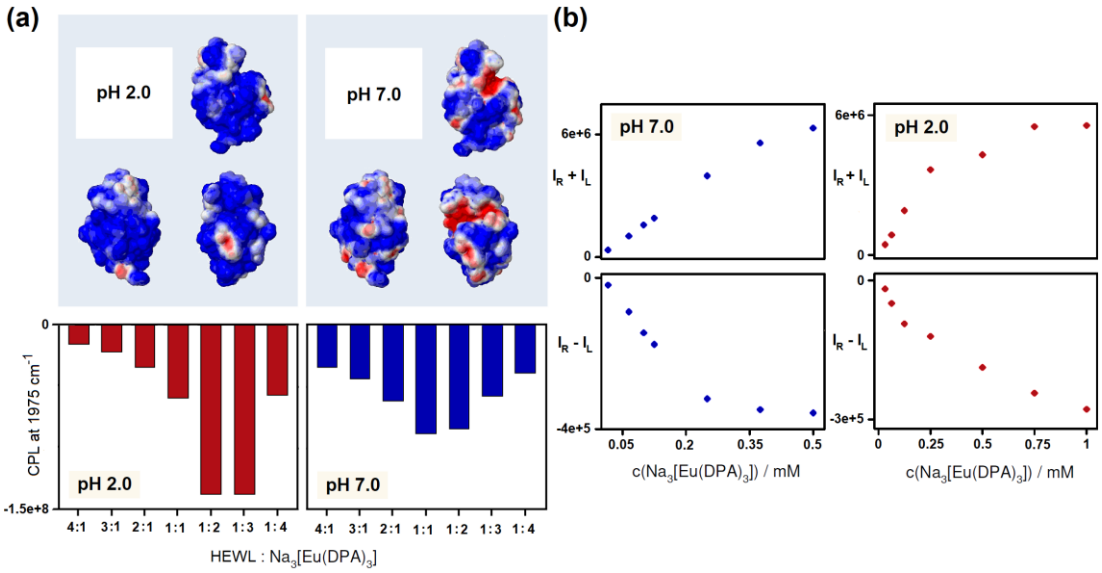

Figure 31. Electrostatic interaction between lysozyme and the $[Eu(DPA)_3]^{3-}$ anion. **(a) Top:** Electrostatic potential surface (EPS) map (blue – positive, red – negative) of lysozyme at pH 2.0 (10.2210/pdb3WUN/pdb) and at pH 7.0 (10.2210/pdb2HUB/pdb). The calculation of protonation states by PROPKA 3.0[227, 228] showed that HEWL had a total net charge of +8 at pH 7.0, and +18 at pH 2.0. EPS map was obtained by online visualization tool implemented in CHARMM-GUI.[229-231] **Bottom:** Job's plots of CPL intensity at 1975 cm^{-1} for the mixture of HEWL and $Na_3[Eu(DPA)_3]$ at different molar ratios; the total molar concentration of both species was kept constant at 0.5 mM. **(b)** TL and CPL intensity of HEWL and $Na_3[Eu(DPA)_3]$ at 1975 cm^{-1} as dependent on the concentration of the complex; concentration of HEWL was 0.25 mM.

Our adapted *ChiralRaman-2X* (*BioTools, Inc.*) spectrometer is able to measure Stokes shifts from 532 nm laser excitation in the range of 90 to 2300 cm^{-1} (~534 – 606 nm). This allowed to measure two luminescent transitions of Eu^{3+} ion: $^5D_0 \rightarrow {}^7F_0$ and $^5D_0 \rightarrow {}^7F_1$. Other transitions from the $^5D_0$ excited state (see **Table 6**) are unreachable. However, an ROA instrument built in the Palacký University in Olomouc can measure in an extended range from 45 to 4000 cm^{-1} (~534 – 675 nm). TL and CPL spectra obtained within collaboration with the Olomouc laboratory for monomeric HEWL / $Na_3[Eu(DPA)_3]$ and PLGA / $EuCl_3$ are shown in **Figures 32** and **33**. The grey area in the figures shows the spectral range accessible with *ChiralRaman-2X* instrument.

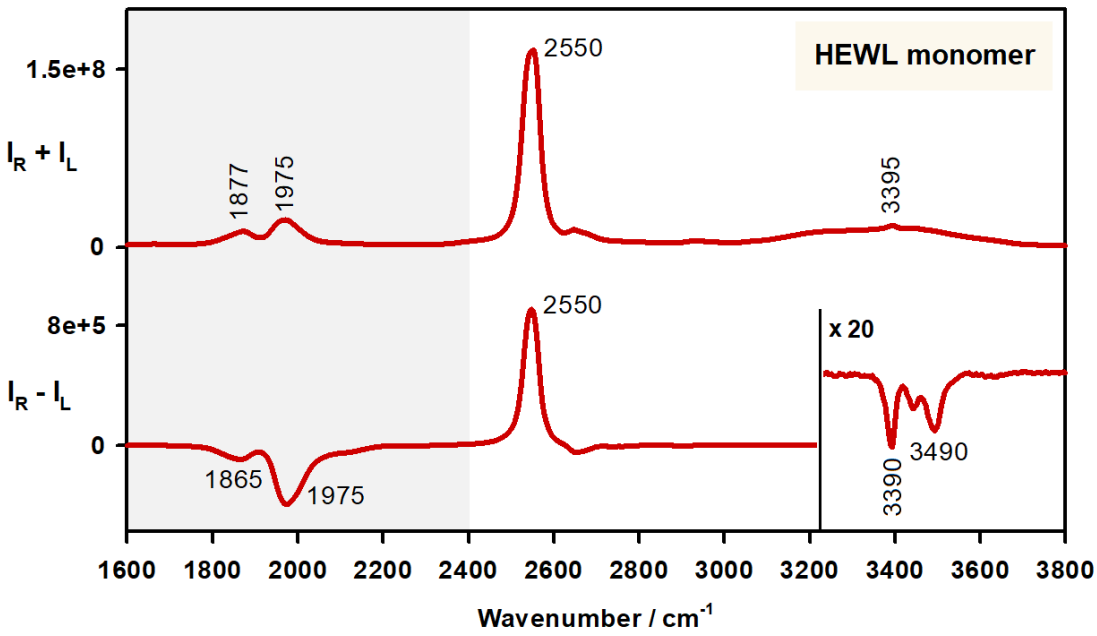

Figure 32. TL and CPL spectra of native HEWL (100 mg/mL) with 1mM $[Eu(DPA)_3]^{3-}$ in an extended spectral region. Spectra were measured with a custom-built ROA spectrometer in Palacký University in Olomouc.

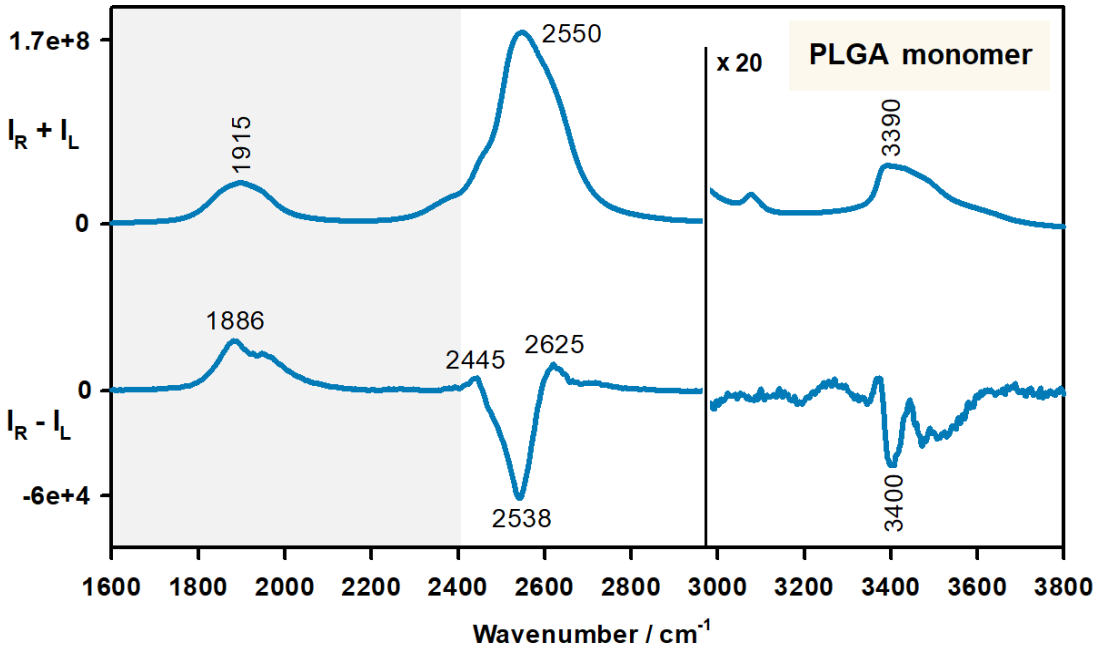

Figure 33. TL and CPL spectra of PLGA (10 mg/mL) with 1mM $EuCl_3$ in an extended spectral region. Spectra were measured with a custom-built ROA spectrometer in Palacký University in Olomouc.

We thus observed two additional TL bands. The more intense one at 2550 cm^{-1} (~ 615 nm; $^5D_0 \rightarrow {}^7F_2$) is hypersensitive, i.e. its intensity is significantly influenced by the local symmetry of Eu^{3+} ion and the nature of ligands. The transition at 3395 cm^{-1} (~649 nm, $^5D_0 \rightarrow {}^7F_3$) is very weak because it is forbidden by Judd-Ofelt theory and can be observed due to the *J*-mixing in strong crystal fields.[225] These additional bands can be used in the future for further correlation of spectra to protein structure.

In addition to the wide range, the spectrometer in the Palacký University in Olomouc allows to measure in all four ROA polarization modes: SCP, ICP, DCP I and DCP II. An overview of the modes and TL and CPL spectra of PLGA in the presence of $EuCl_3$ are shown in **Figure 34**. The scattered circular polarization provides the usual CPL spectrum. In DCP I and DCP II modulations, the resultant spectra reflect also a differential absorption of left- and right-circular polarization (circular dichroism). In this case, CD is negligible and the spectra can be related to the SCP CPL signal as:

$$\mathrm{DCP_I} \approx \frac{\mathrm{CPL}}{2} \tag{41}$$

$$\mathrm{DCP_{II}} \approx -\frac{\mathrm{CPL}}{2} \tag{42}$$

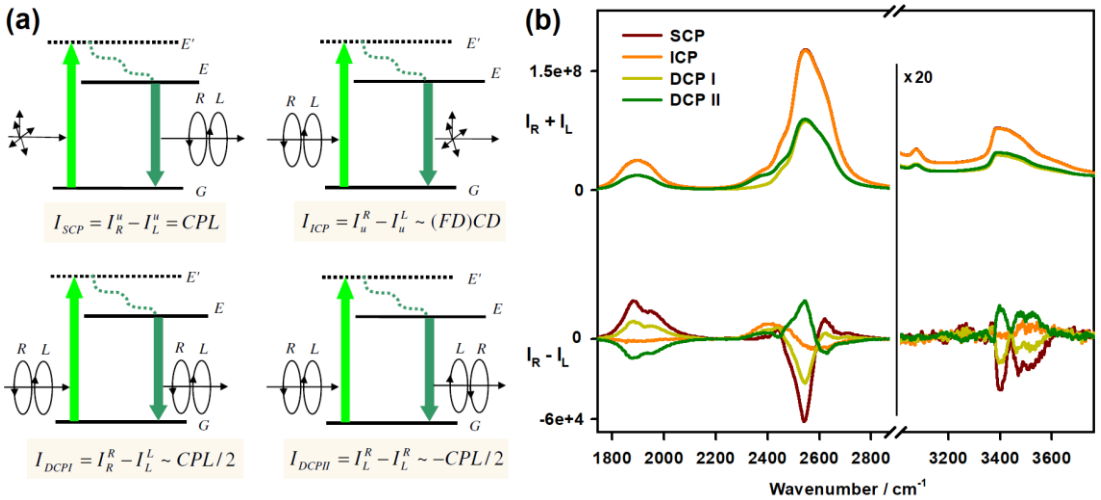

Figure 34. Circularly polarized luminescence in different ROA polarization modes. **(a)** Schematic representation of ROA polarization modes in terms of CPL. **(b)** TL and CPL spectra of PLGA (10 mg/mL) and 1mM $EuCl_3$ in different polarization modes measured with a custom-built ROA instrument in Palacký University in Olomouc. In TL, SCP and ICP spectra overlap.

Only the ICP modulation provides additional information to the SCP mode. In this case, the induced chirality originates mainly from the small differences in absorption of left- and right-circularly polarized light. Therefore, it formally equals to the fluorescence-detected circular dichroism. In **Figure 34b**, these basic trends are illustrated; only ICP mode provides a different shape (and lower intensity) when compared to usual CPL measured in SCP.

2.2.4. Polymorphism of Amyloid Fibrils

Fibril polymorphism means that the same polypeptide chain can adopt multiple geometries. It is very common both *in vivo*[232] and *in vitro*.[233, 234] Various polymorphic fibril types can have different characteristics, e.g. assembly mechanism, kinetics of growth or cytotoxicity.[235, 236] *In vitro*, polymorphism of the fibrils is highly dependent on experimental conditions during their preparation; even small variations in pH, protein concentration or seeding can trigger growth of different fibril polymorphs.[210, 237, 238] Differences between individual fibril types include variations in length and fibril bending, fibril width or assembly into macroscopic aggregates. Such variations usually originate in the differently structured oligomers, which later fold into the fibril structure (**Figure 35**). Sometimes the polymorphism on protofilament level may not translate to the macroscopic fibril polymorphism.[239] Therefore, it is convenient to assess the polymorphism of fibrils not only by high-resolution microscopic techniques such as TEM or AFM, but also use spectroscopic methods that may produce specific spectroscopic signatures for different fibril types.

We monitored an effect of the seeding on the morphology of amyloid fibrils. Usually, seeds (solutions containing already grown fibrils, sonicated for 1 hour to decrease viscosity and break fibrils to smaller pieces) were added to the fresh protein solutions at the concentration of 10 % (w/w). Then the fibrils were grown in a standard way. We used both the seeds of the same protein (homogeneous seeding) and of a different protein (heterogeneous seeding). The seeds significantly affected the structure of resultant fibrils; VCD proved to be the most sensitive of all used methods to the fibril polymorphism. In some cases, the intensity of the amide I' vibration varied

within several orders of magnitude, and even the shape and sign of the spectra was changed.

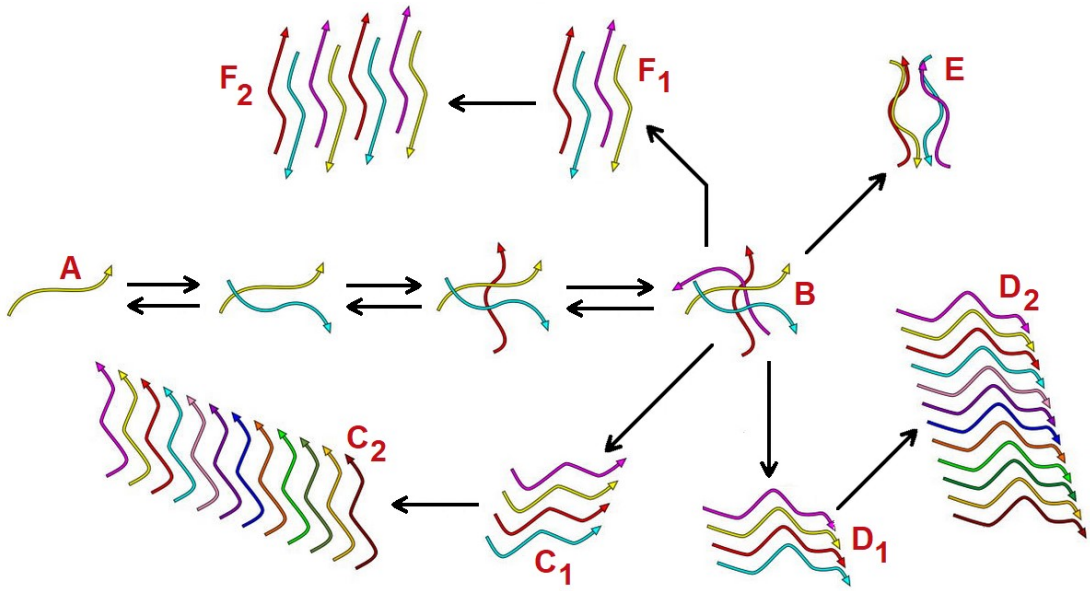

Figure 35. Schematic representation of molecular mechanisms leading to the formation of various fibril polymorphs. From monomer **A**, a transient oligomer **B** can be created by a series of reversible monomer additions. Next, cross-β-like structures $\mathbf{C_1}$, $\mathbf{D_1}$ and $\mathbf{F_1}$ can serve as nuclei for growth of polymorphic fibril types $\mathbf{C_2}$, $\mathbf{D_2}$ and $\mathbf{F_2}$. Outside of aggregation into fibrils, metastable non-regular oligomers such as **E** can be present. All of the species $\mathbf{C_1}$, $\mathbf{D_1}$, $\mathbf{F_1}$ and **E** are in a dynamic equilibrium with oligomer **B** and can interchange from the less stable to the more stable species.[240]

Figure 36 shows CPL, fluorescence and VCD spectra of two polymorphic types of lysozyme fibrils; the first one was prepared by a standard procedure and the second one by homogeneous seeding. When HEWL fibrils grow slowly from acidified protein solutions, a relatively strong negative VCD band can be observed at 1616 cm^{-1} ($g = 4\times10^{-4}$). If the protein solution is seeded with pre-grown fibrils, the growth is much faster, the sign of the VCD band at 1616 cm^{-1} is flipped and its intensity is almost 10× higher ($g = 39\times10^{-4}$). The flip may indicate a different long-range twist in two fibril types, while higher *g*-factor suggests that larger protein aggregates are preferred by catalytic seeding. Also, the ThT fluorescence assay provides about 8 times higher fluorescence for seeded fibrils with a slight shift of a maximum from 483 to 476 nm.

However, CPL seems to be indifferent to two fibril types. This confirms the hypothesis that while VCD signal enhancement is sensitive to long-range ordering of chromophores and therefore its intensity may be at least partially proportional to the length of fibrils, the $[Eu(DPA)_3]^{3-}$ ion is sensitive only to the environment in close vicinity of the metal ion and is therefore unable to capture changes in the long-range order.

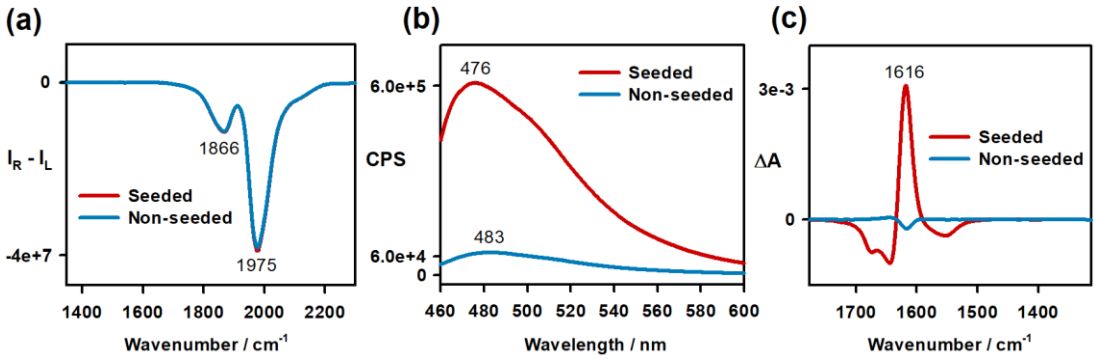

Figure 36. Seeded and non-seeded HEWL fibrils. **(a)** CPL of fibrils (100 mg/mL, pH 2.0) with 1mM $Na_3[Eu(DPA_3]$, normalized to TL; the spectra of seeded and non-seeded fibrils overlap. **(b)** Fluorescence spectra of HEWL fibrils (0.5 mg/mL) with ThT (50 μM). **(c)** VCD spectra of HEWL fibrils in D_2O in a BaF_2 cell, normalized to IR.

The seeding has a profound effect on VCD spectra. Homogeneous seeding of PLGA fibrils results in the similar IR as for the spontaneous fibrils (**Figure 37**). In VCD, the COOD signal around 1736 cm^{-1} adopts a three-sign W-shape and the main band shifts to 1595 cm^{-1}. Also, differences in relative intensities of the negative bands at 1620 and 1580 cm^{-1} can be observed. The amide II' bands at 1471 and 1416 cm^{-1} become more visible and more comparable with the amide I' intensity. In case of heterogeneous seeding with PDGA seeds, the main 1597 cm^{-1} VCD band flips sign, while IR spectrum remains about the same. The COOD couplet around 1735 cm^{-1} has a flipped sign when compared to the spontaneous fibrils. Interestingly, the sign of amide II' bands remains the same in all of the fibril types. A significant drop in *g*-factors for seeded fibrils can be observed (~30×10^{-4} for spontaneous fibrils vs. 5×10^{-4} for homogeneous and 3×10^{-4} for heterogeneous seeding). This can be interpreted as

a sign of imperfect fibrils; the accelerated growth initiated by seeds forms either shorter or less-ordered aggregates.

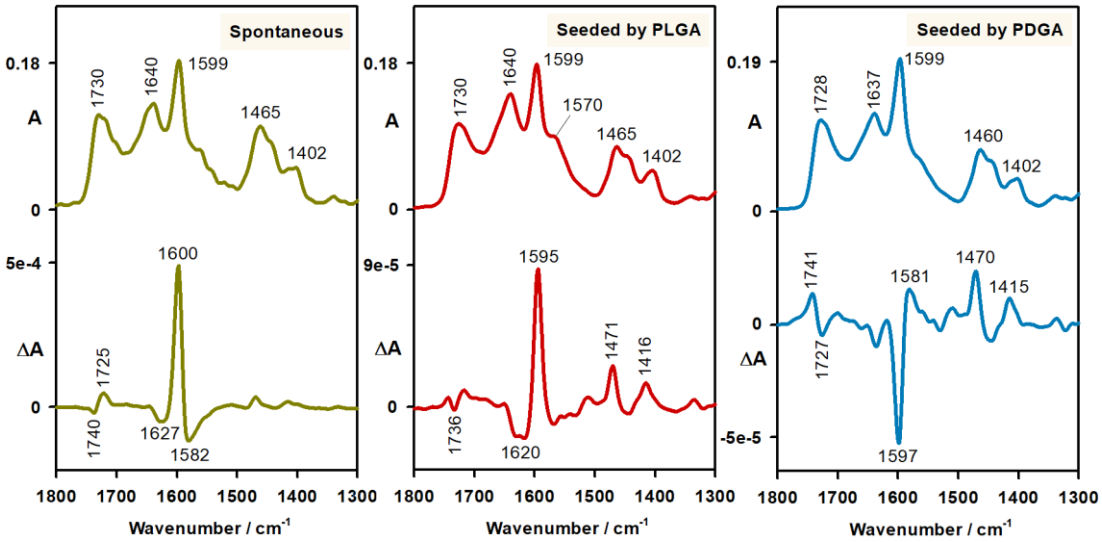

Figure 37. IR absorption and VCD spectra of spontaneous, PLGA- and PDGA-seeded PLGA fibrils (PLGA concentration 15 mg/mL, seeds 10 % (w/w), pH 4.3, CaF_2 cell).

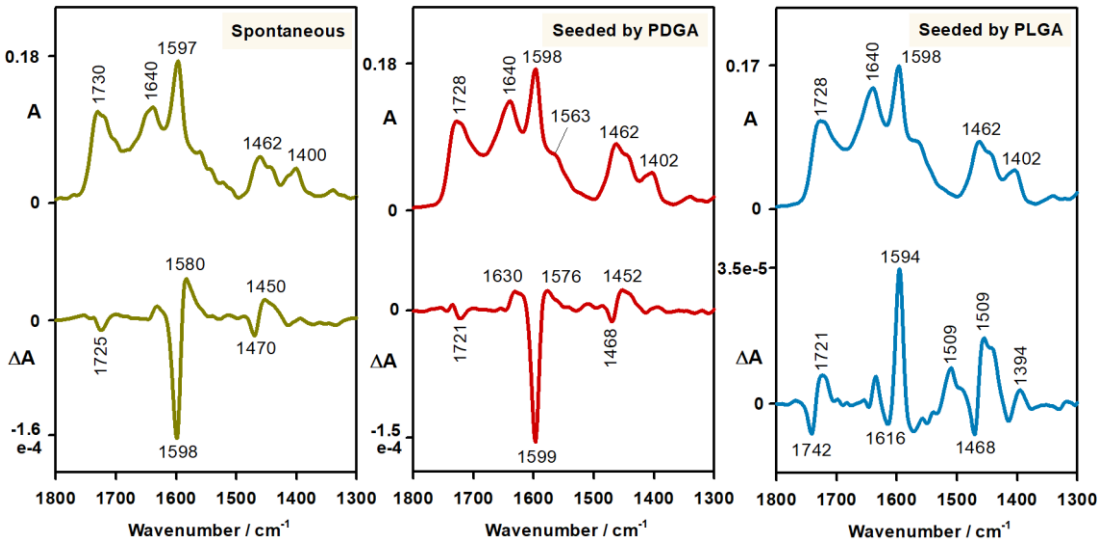

Figure 38. IR absorption and VCD spectra of spontaneous and seeded PDGA fibrils; conditions are the same as in Figure 37.

Similar conclusions can be drawn from the seeding of PDGA fibrils (**Figure 38**). While homogeneous seeding provides fibrils with the same negative sign of the main amide I' VCD band around 1599 cm^{-1}, seeding with PLGA causes a slight shift in the frequency (from 1598 to 1594 cm^{-1}) and a flipped sign. This behaviour can be explained by a sergeant-and-soldiers principle, where chirality of the system is determined by chirality of a relatively minor component. In this case the chirality of the fibrils represented by the sign of the main amide I' VCD band is governed by the chirality of the seeds. This principle is schematically presented in **Figure 39**.

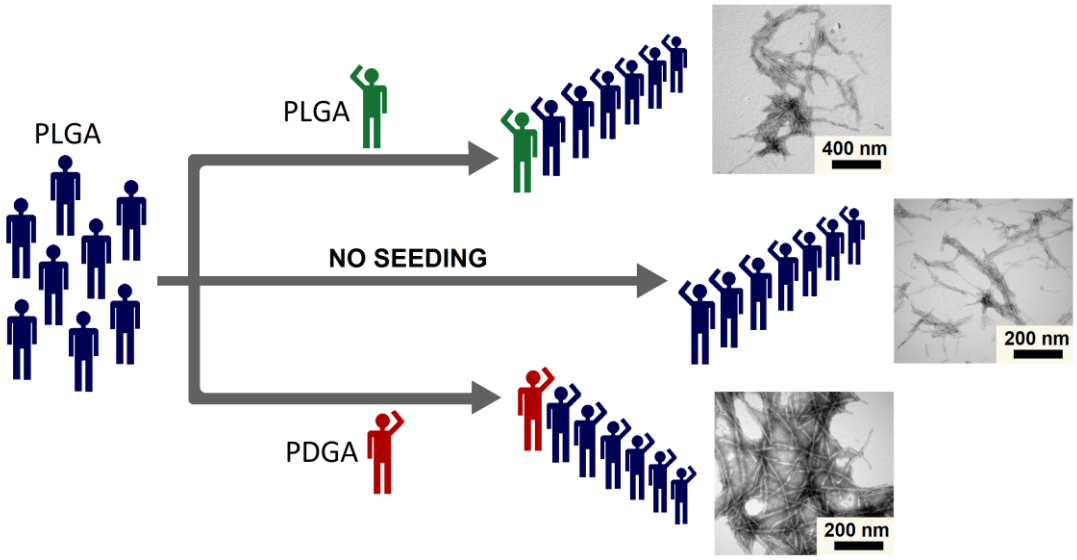

Figure 39. The sergeant-and-soldiers principle in seeding of amyloid fibrils. Chirality of the seeds determines the structure and chirality of the resulting fibrils, observable by a sign of the amide I' VCD band.

To better understand the mechanism behind the sign flip of VCD signal, we varied the amount of PLGA seeds used to catalyze the growth of PDGA fibrils (**Figure 40**). VCD spectra of spontaneous PDGA fibrils (**Figure 38**) and those seeded by 1 % of PLGA both exhibit a main negative VCD band at 1598 cm^{-1}. As for the other seeded PGA fibrils, VCD intensity is lower ($g = 5\times10^{-4}$) than without seeds. As the amount of seeds in the solution increases, the negative maximum of this band shifts to higher frequencies (1612 cm^{-1} in 10 % of seeds), and its relative intensity significantly decreases. Similarly, the positive band at 1583 cm^{-1} for 1 % seeded fibrils grows in

intensity and shifts to 1594 cm^{-1} for 10 % of seeds. The flip of the main VCD band is therefore not a simple mirroring across the x-axis, but involves a frequency shift and a change of relative intensities.

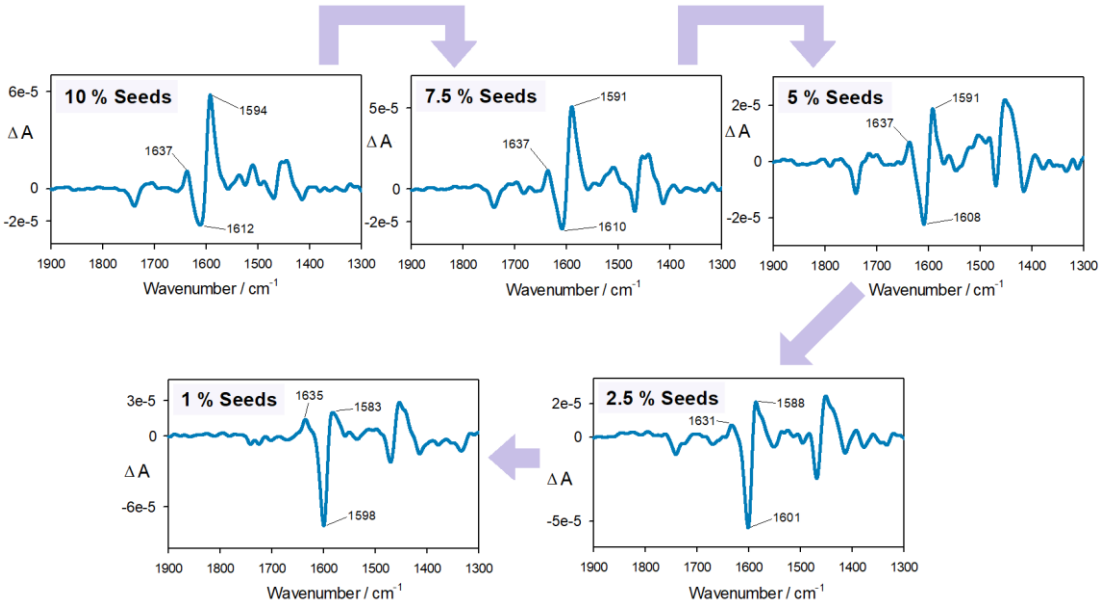

Figure 40. VCD spectra of PDGA fibrils seeded with different amounts of PLGA seeds. The arrows indicate the direction of decreasing amount of seeds in the samples.

Another interesting example of fibril polymorphism induced by the seeding of lysozyme fibrils by different proteins is illustrated in **Figure 41**. Only slight differences in the amide I' IR band at 1623 cm^{-1} (1617 cm^{-1} for seeding with polyglutamic acids) occurs. The band at 1623 cm^{-1} indicates a high β-sheet content. A shift of its maxima to 1617 cm^{-1} in case of PGA seeding indicates a stronger inter-sheet interaction and possibly more compact packing. Interestingly, all seeds produced fibrils with reversed sign of VCD main amide I' band when compared to the spontaneous case. This could mean that rather than due to a specific structure of seeds, the seeding produces fibrils with a reversed sign of VCD due to a kinetic preference. The *g*-factor for spontaneous fibrils is 4×10^{-4}; all of the seeded fibrils produced higher *g*-factors (39×10^{-4} for seeding with HEWL, 18×10^{-4} for INS, 14×10^{-4} for PLGA and 9×10^{-4} for PDGA seeding).

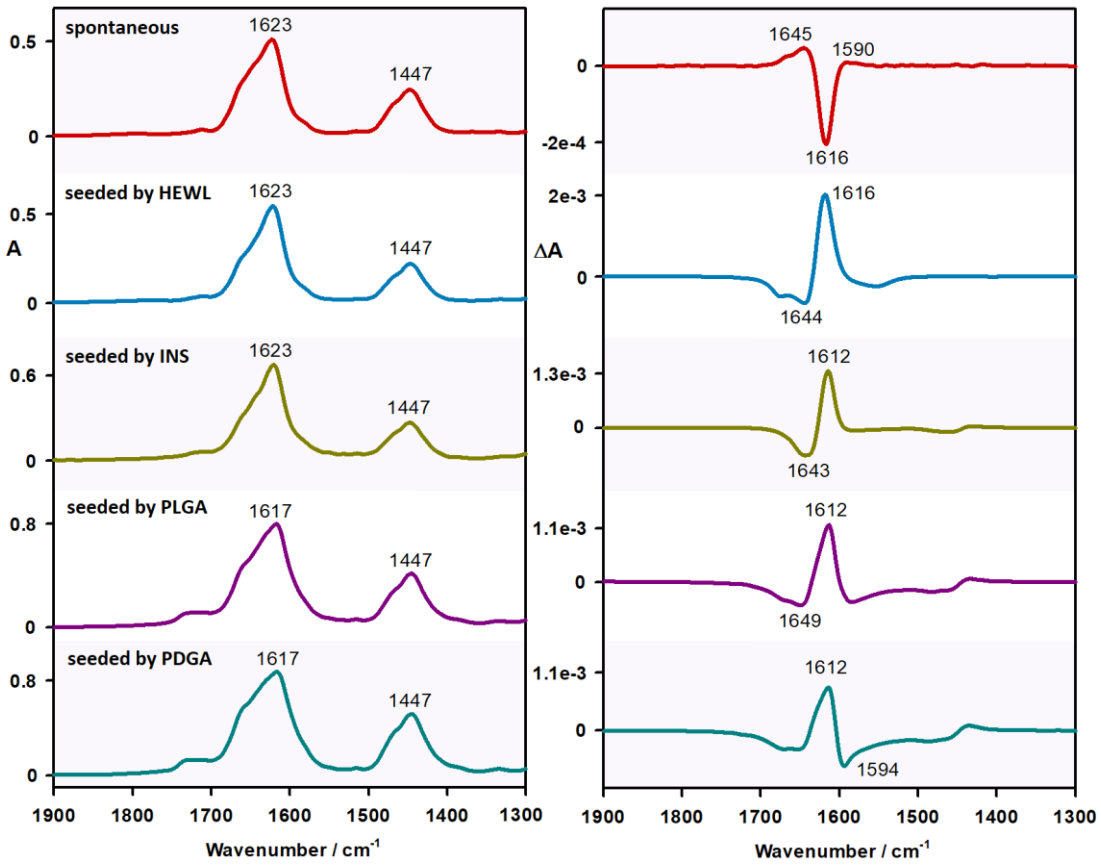

Figure 41. IR absorption and VCD spectra of HEWL fibrils (100 mg/mL in D_2O, pH 2.0, CaF_2 cell) prepared by 5 procedures: spontaneous fibrils, fibrils seeded by HEWL, by INS, by PLGA and by PDGA.

The seeding for lysozyme and insulin is presented in **Figure 42**. The VCD of insulin spontaneous fibrils is similar to that of HEWL fibrils seeded by insulin. It looks like the supramolecular arrangement is not dependent on the protein used, but is determined by the seeds. A similar behavior can be observed for HEWL spontaneous fibrils and insulin fibrils seeded by HEWL seeds. These results suggest the presence of the sergeant-and-soldiers principle during the initial stages of fibrillation during which the structure of future fibrils is already determined. Various polymorphic fibril types can have a similar secondary structure seen by IR and CPL spectra (typically *β*-sheet), but they differ in the macroscopic arrangement and chirality reflected by VCD. Therefore, VCD allows to easily distinguish between the fibril polymorphs. The seeding procedures are often used in *in vitro* fibril preparations. We showed that they

significantly affect the structure of the fibrils, and therefore should be used with caution.

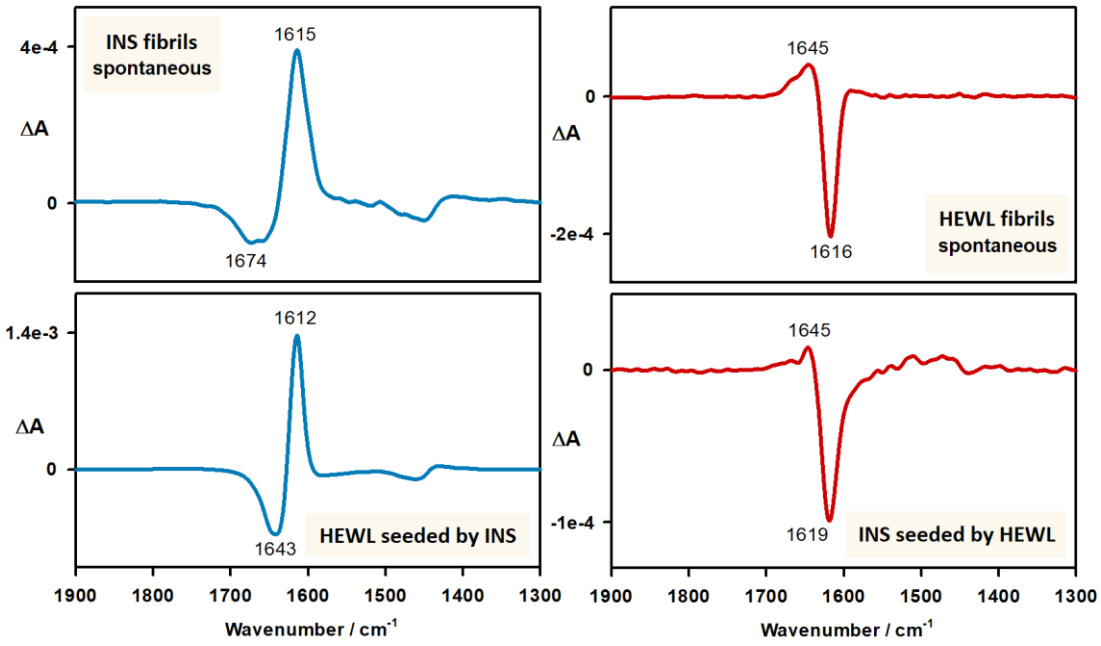

Figure 42. VCD spectra of spontaneous and seeded HEWL (100 mg/mL in D_2O, pH 2.0, CaF_2 cell) and INS (40 mg/mL in D_2O, pH 2.0, CaF_2 cell) fibrils.

3. Vibrational Circular Dichroism of Nucleoside Crystals

Although standard applications of VCD aim to the liquid phase, "solid-state VCD" (SS-VCD) exists as well.[211, 241] Samples can be measured inside KBr pellets, as mull suspensions, or films. Such experiments were conducted on amino acids,[242-245] peptides,[245-248] carbohydrates[249] and other molecules.[250-255] Recently, the VCD of chiral molecules adsorbed on nanoparticles was reported.[256, 257] The lack of solvent interference is one of the main benefits of some SS-VCD experiments. For peptides, up to 100-times less sample was required for SS-VCD experiments compared to the classical approach.[247] VCD can be applied to turbid suspensions usually not suitable for electronic spectroscopic methods due to the scattering. As another advantage, the number of conformations in SS-VCD is limited and theoretical interpretation of the data may thus be simplified.[258]

On the other hand, solid samples may be anisotropic, they often exhibit linear and circular birefringence (LB, CB) and dichroism (LD, CD). LB is an anisotropy in the refraction, CB is a difference in the refractive indices for left- and right-circularly polarized light, LD is the anisotropy in absorption, and CD is the difference in the absorption of left- and right-circularly polarized light.[259] These effects may contribute to artifacts that are often much larger than true VCD signal. Also, the non-ideal characteristics of the spectrometer such as residual birefringence of the photoelastic modulator or anisotropic sensitivity of the detector can combine with the orientation dependent artifacts.[260]

A beam of polarized light can be expressed as a Stokes vector (eq. 43; I_{total} is the total intensity, I_X is its x-component, and I_{rcp} / I_{lcp} are the intensities of the right- and left-circularly polarized light). Intensity of the detected signal $\mathbf{I_d}$ in the standard VCD spectroscopic setup (**Figure 43**) can be expressed as in eq. 44, where **D**, **V**, **M** and **P** are Mueller matrices corresponding to the detector, sample, photoelastic modulator and linear polarizer, respectively. $\mathbf{I_0}$ is the intensity of the incident light. The Mueller matrices describe the influence of the optical elements and the sample on the passing light.[251]

$$\mathbf{S} = \begin{pmatrix} S_0 \\ S_1 \\ S_2 \\ S_3 \end{pmatrix} = \frac{1}{I_{total}} \begin{pmatrix} I_{total} \\ I_{45°} - I_{135°} \\ I_{rcp} - I_{lcp} \\ I_{0°} - I_{90°} \end{pmatrix} \tag{43}$$

$$\mathbf{I_d} = \mathbf{D} \cdot \mathbf{V} \cdot \mathbf{M} \cdot \mathbf{P} \cdot \mathbf{I_0} \tag{44}$$

The form of Mueller matrices can be found in the literature.[251, 260] To separate true VCD signal from other contributions, the experimental setup needs to be calibrated. Several contributions can be directly measured by a specific configuration of optical elements (**Figure 43**). Some artifacts coming from the optics can be reduced by double polarization modulation[261] and use of a rotating half-wave plate.[262]

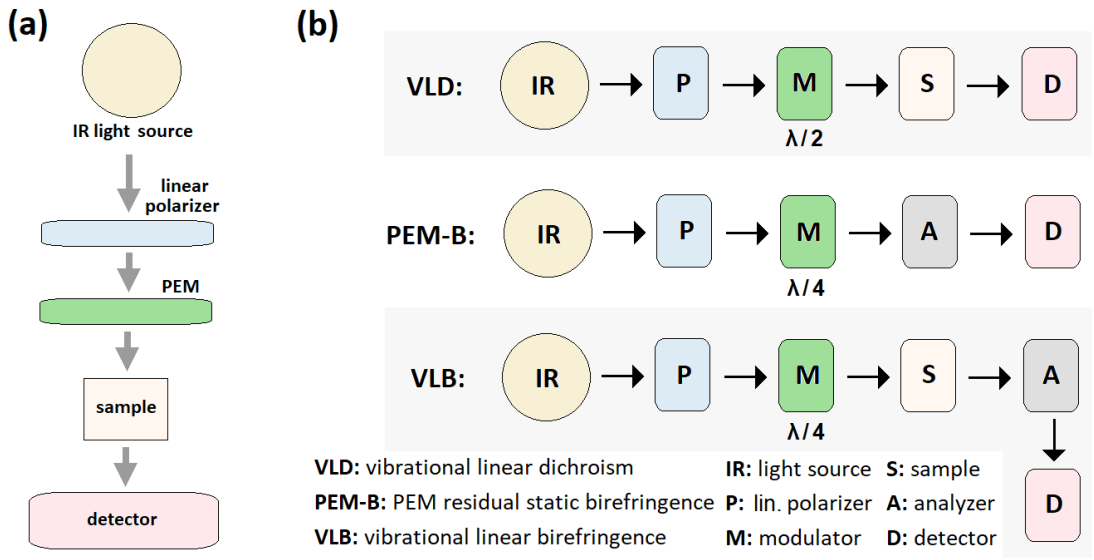

Figure 43. (a) Schematic illustration of a standard single PEM VCD setup.[251] **(b)** Configuration of optical elements to obtain the linear dichroism (top), PEM residual static birefringence (middle) and linear birefringence (bottom) contributions to VCD signal.[260]

Special procedures were proposed to measure SS-VCD. An approach from Buffeteau *et al.*[260] requires determination of the angle of sample rotation with maximum linear anisotropy and setting it to $\Theta = 0°$. Then the spectra measured at Θ and at $\Theta \pm 90°$ can be used to extract the true VCD (eq. 45). Another approach, for which further measurements of the maximum anisotropy are not necessary, was

developed by Merten *et al*.[251] The VCD spectrum is obtained by recording the spectra for selected sample orientations and calculating their quarter-sum (eq. 46). The most convenient method which we used also here is to use rotators that rotate the sample around the light propagation axis. To avoid as many artifacts as possible, spectra for the sample flipped around the axis perpendicular to the IR beam were measured as well.[258]

$$VCD = \frac{\boldsymbol{VCD}\,(\boldsymbol{\theta}) + \boldsymbol{VCD}\,(\boldsymbol{\theta} \pm \mathbf{90°})}{\mathbf{2}} \tag{45}$$

$$VCD = \frac{\boldsymbol{S}_{\boldsymbol{VCD}}^{\boldsymbol{face}}(\boldsymbol{\theta}) + \boldsymbol{S}_{\boldsymbol{VCD}}^{\boldsymbol{face}}(\boldsymbol{\theta}+\mathbf{90°}) + \boldsymbol{S}_{\boldsymbol{VCD}}^{\boldsymbol{back}}(\boldsymbol{\theta}) + \boldsymbol{S}_{\boldsymbol{VCD}}^{\boldsymbol{back}}(\boldsymbol{\theta}+\mathbf{90°})}{\mathbf{4}} \tag{46}$$

In the solid state, atoms / molecules may form either crystals or amorphous glasses. In amorphous solids, SS-VCD is provided by molecular chirality similarly as for liquids. In crystals, "supramolecular chirality" may lead to additional signal, often very strong. Chiral molecules always form chiral crystals.[263] But even achiral molecules can form chiral crystals if the crystal space group contains at least one screw axis other than 2_1. Approximately 23 % of all non-biological and 38 % of all known crystals are chiral.[264] Distortions of a crystal can also lead to an additional chirality.[265] Crystals often exhibit polymorphism. In polymorphic crystals, the same kind of molecules form different crystallographic structures due to different packing arrangements within the crystal structure. Polymorphic crystals also exhibit different supramolecular chirality.[266-268] This all is very challenging for the chiroptical spectroscopy. Due to the high intensity of crystal VCD, its measurement is easy.[170, 269] A recent computational study of crystalline alanine[169] linked this strength to a helical arrangement of the chromophores in crystal layers.

We used VCD spectroscopy to study several nucleosides. Nucleosides are glycosylamines that consist of a nitrogenous base and ribose or 2'-deoxyribose. The base derives from purines (A: adenine, G: guanine) or pyrimidines (T: thymine, U: uracil, C: cytosine). The anomeric carbon of the sugar is connected to N9 of purine or N1 of pyrimidine by a glycosidic bond (**Figure 44**). Nucleoside and one or more phosphate groups connected to the C5' of the sugar form a nucleotide. These

compounds form nucleic acids and participate in a variety of signaling, regulatory and energetic pathways. They are also used as antibiotics,[270-272] antiviral[273-275] and anticancer drugs.[276-279]

Table 7. Water solubility of selected nucleosides at room temperature.[280-282]

A	G	U	C	T	dG
5.1 mg/mL	0.7-1 mg/mL	50 mg/mL	100 mg/mL	50 mg/mL	8.4 mg/mL

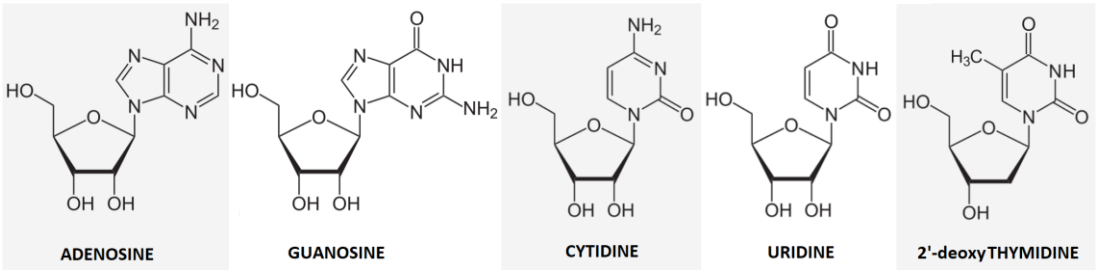

Figure 44. Chemical structure of common nucleosides.

Purine nucleosides are generally poorly soluble in water (**Table 7**) due to the strong intermolecular interactions in the solid state. Their solubility can be slightly enhanced by a complex formation with various amino acids, carbohydrates or vitamins.[283, 284] Above the solubility limit, they form turbid water suspensions. Guanosine and its derivatives in solution self-assemble into supramolecular semi-regular structures.[285-288] These are usually based on the G-quadruplex motif, in which four guanine bases associate by hydrogen bonds into a square planar structures (G-tetrads) that stack on top of each other. G-quadruplexes are stabilized by divalent cations.[289] Outside of their important biological roles, such structures can be used in organic chemistry as enantioselective catalysts,[290] or in medical diagnostics and treatment.[291]

Nucleosides, nucleotides and nucleic acids exist in a variety of hydrated states depending on the relative humidity. The hydration can even trigger conformational transitions, e.g. from A- form to B-form in DNA.[292] Water molecules are also

important for recognition and interactions between proteins and nucleic acids.[293, 294] Water in crystals may affect their structure, stability or solubility.[295]

From this point of view, guanosine is very interesting. It exists in anhydrous (A) and semi-hydrated (M; ~1.2 – 1.3 H_2O per 1 nucleoside) forms, and as a dihydrate (H).[296-298] At ambient humidity, only the H-form is stable. A-form is present at the humidity up to 10 %, while M-forms exist within 10 – 20 % humidity. Crystal structures of some of these forms have been solved. Crystals of the H-form (**Figure 45**) are monoclinic ($P2_1$) with two nucleoside molecules and 4 waters per an asymmetric unit. Two asymmetric units form the unit cell. The two bases in the asymmetric unit are nearly equivalent, while the two riboses adopt different conformations. The bases are stacked along the *c*-axis at ~3.3 Å, and hydrogen-bonded along the *b*-axis forming layers. Two water molecules are located in the cavity within the layers bridging the carbonyl and amino groups of the bases and hydroxyl groups of the sugars. The remaining two molecules of water are positioned between the layers and they bridge the hydroxyl groups of riboses in the adjacent layers.[299]

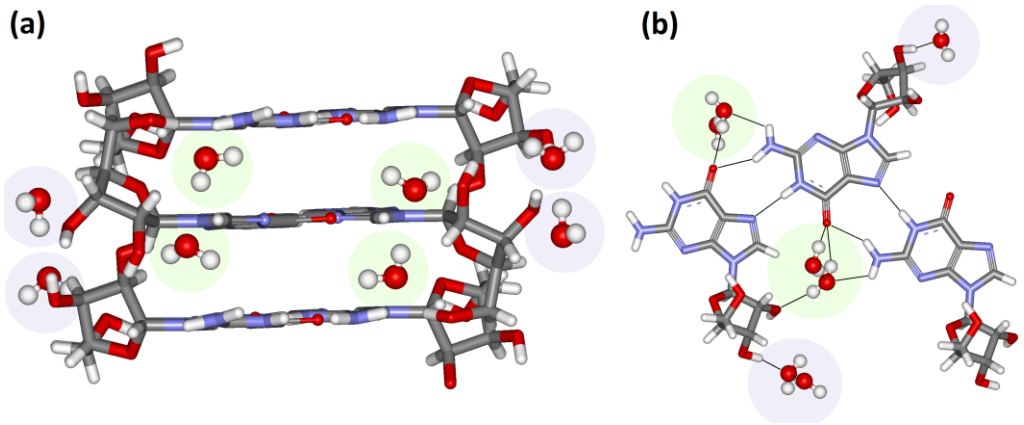

Figure 45. X-ray structure of guanosine dihydrate.[299] **(a)** Layer structure produced by stacked guanine bases. **(b)** 3D hydrogen bonding network (grey solid lines) between the guanosine molecules and waters. The intralayer water is marked with a green circle, while interlayer water is marked with a purple circle.

In the A-state, guanine bases are stacked, and ribose is disordered. During the hydration transition from the A- to the H-state, intralayer hydration sites are occupied prior to the interlayer ones. In the M-state, only the intralayer hydration sites are

usually occupied. Its crystals are orthorhombic. During the desorption process (drying), the intra- and interlayer waters are lost simultaneously. During these transitions, the crystallinity is altered, even though the base-stacking structure is always retained.[297] Some studies show that the M-state can be further resolved into several partially hydrated states with various involvements of hydration sites.[296, 298]

The X-ray structure of adenosine crystals (**Figure 46**) was solved by the Structural Biology group in IOCB (Dr. Blanka Klepetářová) and is in agreement with previous reports.[300] Each adenosine molecule is hydrogen bonded to six neighboring molecules with all nitrogen and oxygen atoms except N9 and O1'. The adenine bases are stacked along the *a* axis with the interplanar distance of ~3.6 Å. The crystal cell is monoclinic, space group $P2_1$. The unit cell contains two adenosines and no water. In standard conditions, solid adenosine does not hydrate. It forms crystals about 7× bigger than guanosine that can no longer orient randomly in the narrow VCD cell with optimal pathlength. Therefore, it provides an interesting system to study the orientational artifacts.

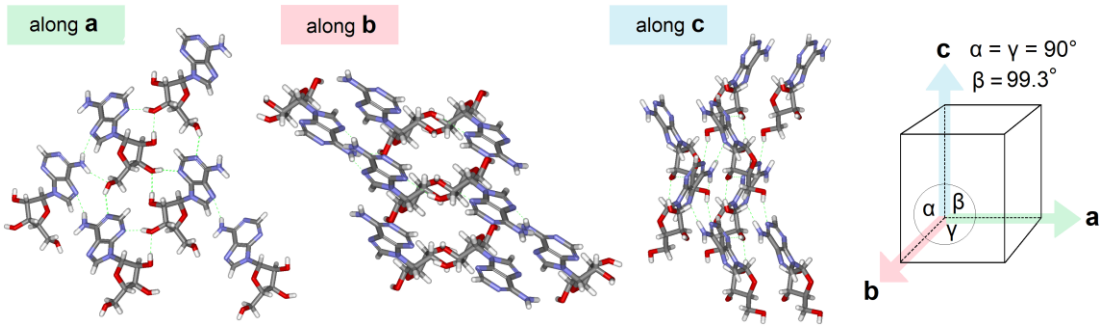

Figure 46. X-ray structure of adenosine seen along the three crystallographic axes. On the right, the axes and angles for monoclinic unit cell are illustrated.

3.1. Methods

3.1.1. Preparation of Nucleoside Suspensions

The nucleosides were obtained from *Sigma-Aldrich* in the anhydrous form (adenosine and *L*-guanosine), as a monohydrate (2'-deoxyguanosine), or in the

hydrated form (guanosine · xH_2O). To prepare anhydrous samples the nucleoside powders were either dried in the vacuum oven at 50 °C overnight or their D_2O suspension was lyophylized overnight. Both of these procedures gave the same VCD spectra. For hydrated samples, the nucleoside powders were stored in saturated water atmosphere for 2 months. To prepare nucleoside suspensions, the powders were mixed with D_2O and thoroughly dispersed in the solvent by vortexing. Above solubility limit, turbid suspensions of nucleoside crystals were obtained. In the text, we state the total concentration of nucleoside in the samples in mg/mL, although it is not the "true concentration" since the samples composed of two phases: truly dissolved nucleosides and nucleoside crystals.

3.1.2. Vibrational Spectra

IR absorption and VCD spectra were measured with a *Chiral IR-2X* instrument (*BioTools, Inc.*) using a BaF_2 cell of 50 μm pathlength, teflon spacer and 4 cm^{-1} resolution. Usually one block of 1560 scans (30 mins accumulation time) was sufficient to achieve adequate signal to noise ratio. The cell was rotated during the measurement. Spectra of D_2O were subtracted as a baseline. Low concentration solutions were measured longer time to increase VCD signal to noise ratio (30 blocks of 1560 scans; total accumulation time ~15 hours).

3.1.3. Optical Microscopy

Nucleoside suspensions (20 mg/mL unless stated otherwise) were placed on a microslide, covered with coverslip and sealed around its edges with a nail varnish. Coverslip and microslide were firmly clamped together with paper clips until the varnish solidified. Microscopy of the crystals was performed with Meopta C36Bi microscope equipped with phase-contrast objectives (Ph20/0.45 and Ph45/0.65) and phase-contrast turret condenser (numerical aperture 1.0). Micrographs were taken through a standard eyepiece (Lambda 010x). The following modalities were employed: polarization (specimen between two crossed linear polarizers), phase contrast and brightfield.

3.2. Results and Discussion

We used VCD spectroscopy to study the supramolecular chirality of crystalline guanosine, *L*-guanosine, 2'-deoxyguanosine and adenosine. We focused also on hydration polymorphism of guanosine crystals. **Figure 47** shows IR and VCD spectra of guanosine at concentrations 1 and 2 mg/mL. IR spectra within 1800 – 1500 cm^{-1} are dominated by base vibrations, which are sensitive to base pairing and stacking. Under 1500 cm^{-1}, base-sugar vibrations can be observed. These are generally sensitive to glycosidic bond rotation and sugar pucker.[301]

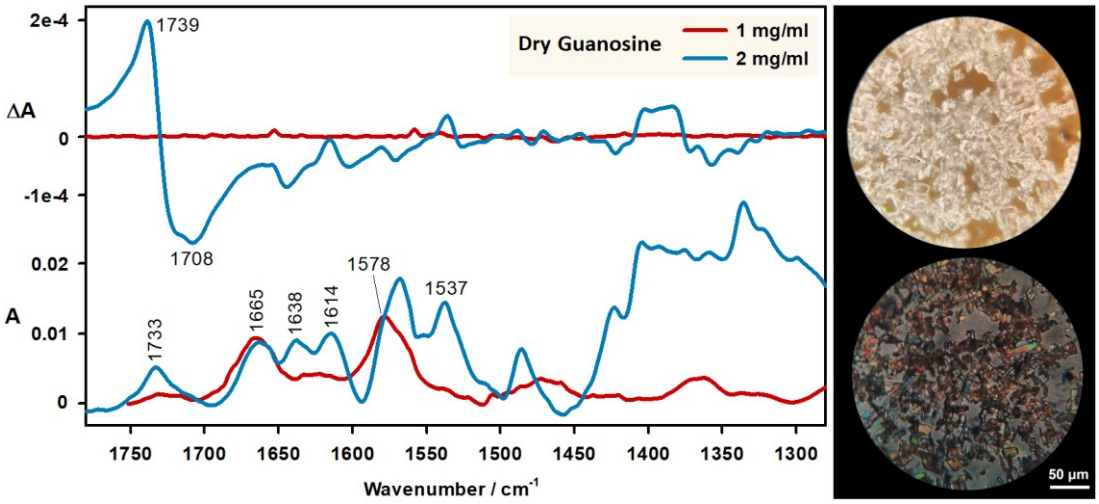

Figure 47. IR and VCD spectra of guanosine solution in D_2O at 1 mg/mL and anhydrous guanosine crystals suspended in D_2O at 2 mg/mL, and microscopic images of guanosine crystals in suspension (top: 45× magnification, phase contrast; bottom: 45× magnification, bright field).

At 1 mg/mL, guanosine formed a solution without a measurable VCD signal. IR is dominated by two absorption bands at 1665 (stretching vibration of the C=O of a non-base paired guanine) and 1578 cm^{-1} (C=N stretching ring vibrations of guanine).[301] IR of crystalline guanosine is more complex with several bands connected exclusively to the base vibrations of crystal guanosine (1638, 1614 and 1537 cm^{-1}). The most prominent (+/–) couplet in VCD centered at 1730 cm^{-1} originates from the absorption band at 1733 cm^{-1}, none of which are present in monomeric guanosine solution. To our best knowledge, assignment of this band is not known. The *g*-factor

for guanosine crystal suspension is fairly high (7.3×10^{-2}) suggesting a long-range chiral order of the chromophores in the crystal structure.

Only very minor changes in IR and VCD spectra occur at different concentrations (**Figure 48**). In absorption, the peak at 1665 cm^{-1} corresponding to the dissolved guanosine is less prominent at higher concentrations due to the increasing amount of crystalline phase. In lower wavenumber region, a strong absorption band at 1129 cm^{-1} corresponds to CO and CC stretching in the ribose ring. Between 1100 and 1000 cm^{-1}, several bands of C5'-OH symmetric and antisymmetric stretching vibrations arise. Lower frequency bands at 988, 916 and 890 cm^{-1} were assigned to ribose-related vibrations. The strongest VCD couplet centered at 1730 cm^{-1} is present at all concentrations with crystalline guanosine, and its shape is not altered. For all spectra, the *g*-factor oscillates around 8×10^{-2}.

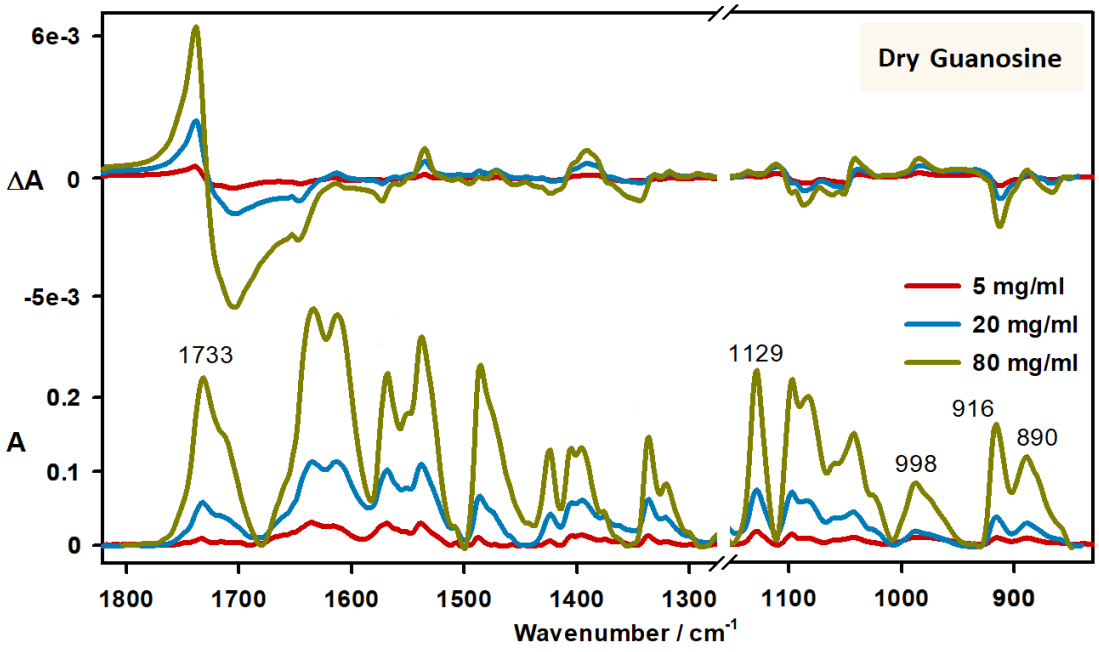

Figure 48. IR and VCD spectra of guanosine crystals in suspension at concentrations 5, 20 and 80 mg/mL in D_2O.

Guanosine crystals exhibit polymorphism dependent on the degree of hydration. We measured and compared the spectra of dry and fully hydrated guanosine (guanosine dihydrate) crystals at concentrations 2 and 20 mg/mL (**Figure 49**). There

are only minor to moderate changes in relative intensities and positions of absorption bands at two concentrations. However, dry and hydrated G shows almost opposite VCD signal independent of concentration. The *g*-factors are comparable (5.4×10^{-2} for dry, and 8.2×10^{-2} for hydrated guanosine at concentration 20 mg/mL).

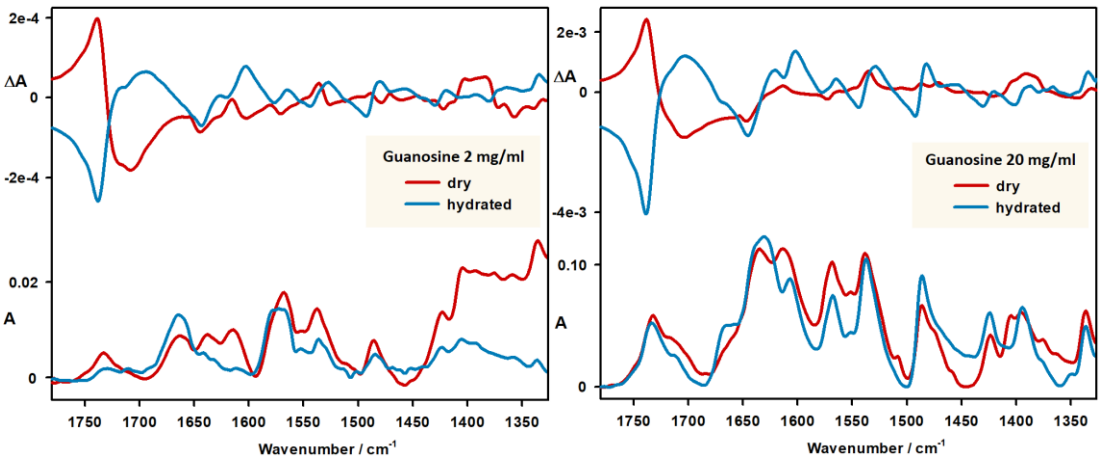

Figure 49. IR and VCD spectra of dry and hydrated guanosine crystals at concentrations 2 and 20 mg/mL in D_2O.

VCD spectra of guanosine crystals can be measured very quickly. Only several scans were needed compared to ~15 hours accumulation times for true solutions of nucleotides and nucleic acids. At 20 mg/mL, VCD was stabilized within 12 seconds (**Figure 50**). The convergence curve shows that the spectrum does not improve beyond 15 mins. VCD can be therefore used as a very fast and easy method for determination of the hydration state of crystalline guanosine.

Next, we compared absorption and VCD spectra of dry 2'-deoxyguanosine (dG) with guanosine (**Figure 51**). Crystals of dG differed significantly from those of G; they were thin and long (~50 – 100 μm). The dG crystalline suspension also exhibited enhanced VCD, although not so much as for G. This is at least partially due to the ~8× higher solubility of dG when compared to G. Therefore, higher concentration of the nucleoside was needed for the same amount of crystals. This is nicely illustrated on the more or less comparable VCD intensity of G at 10 mg/mL and dG at 70 mg/mL. Since our sample consists of monomeric and crystalline dG, the *g*-

factor is different for various concentrations (1.9×10^{-3} at concentration 20 mg/mL, and 5.5×10^{-3} at concentration 70 mg/mL). The shape of dG VCD spectrum is very different compared to G; the strongest VCD originates in stretching vibrations of the guanine base.

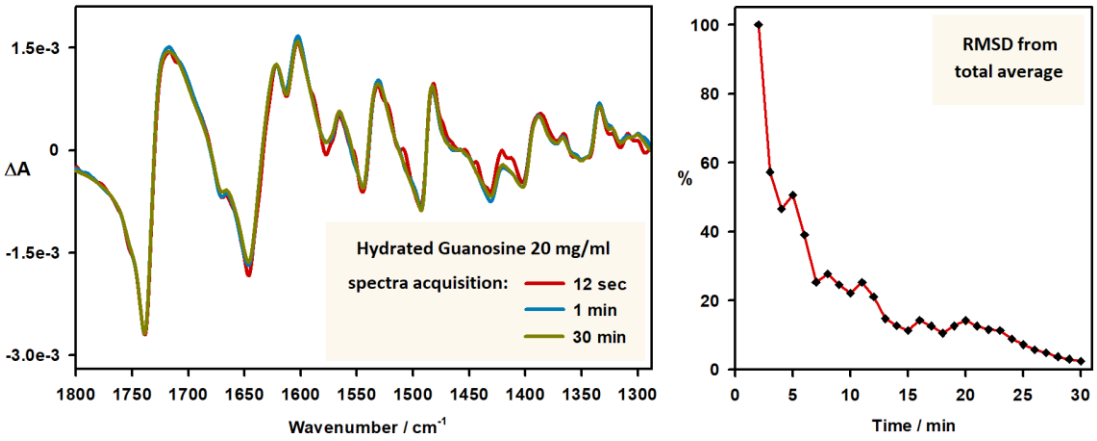

Figure 50. Left: VCD spectra of hydrated guanosine averaged over 12 s, 1 min and 30 mins. Right: Convergence of VCD spectra depending on the total accumulation time; convergence was evaluated as a relative deviation (root-mean-square deviation, RMSD) of successive averages from the total average.

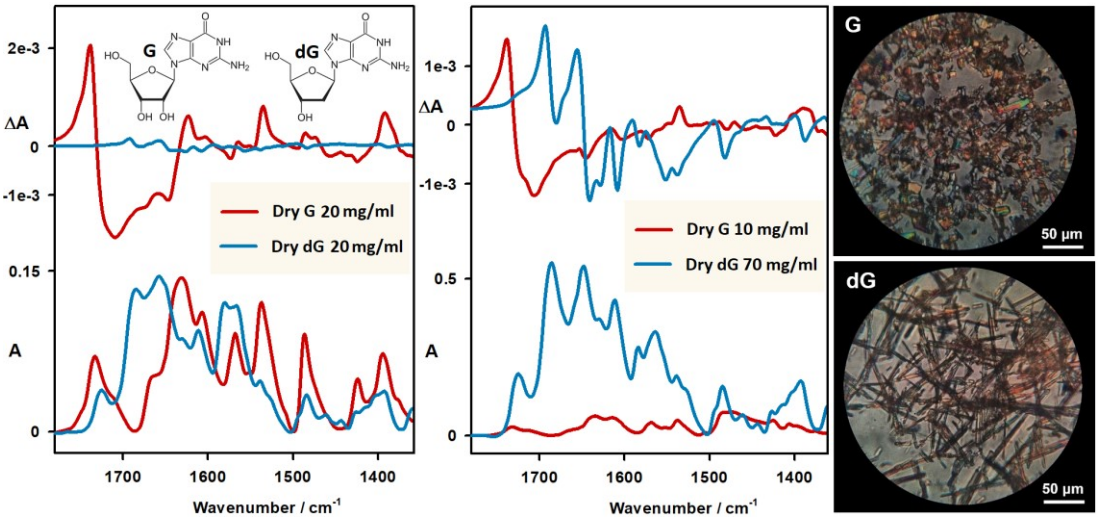

Figure 51. IR and VCD spectra of dry guanosine (G) and 2'-deoxyguanosine (dG) in D_2O at two concentrations; microscopic images of the nucleoside crystals in the suspension (45× magnification, bright field).

In dG, the lack of hydroxyl group on the C2' carbon of ribose ring results in a change of hydration properties; monohydrated species are the most stable.[302] No significant changes were observed in VCD of dry and hydrated dG (**Figure 52**, left). However, the thermogravimetric analysis (TGA) of dry dG revealed 1 mol of bound water per 1 mol of dG, suggesting that drying of 2'-deoxyguanosine at 50 °C for 12 h failed to remove water from the crystal. The water was fully removed at 110 °C in the TGA experiment (**Figure 52**, right). Above 170 °C, the sample decomposed.

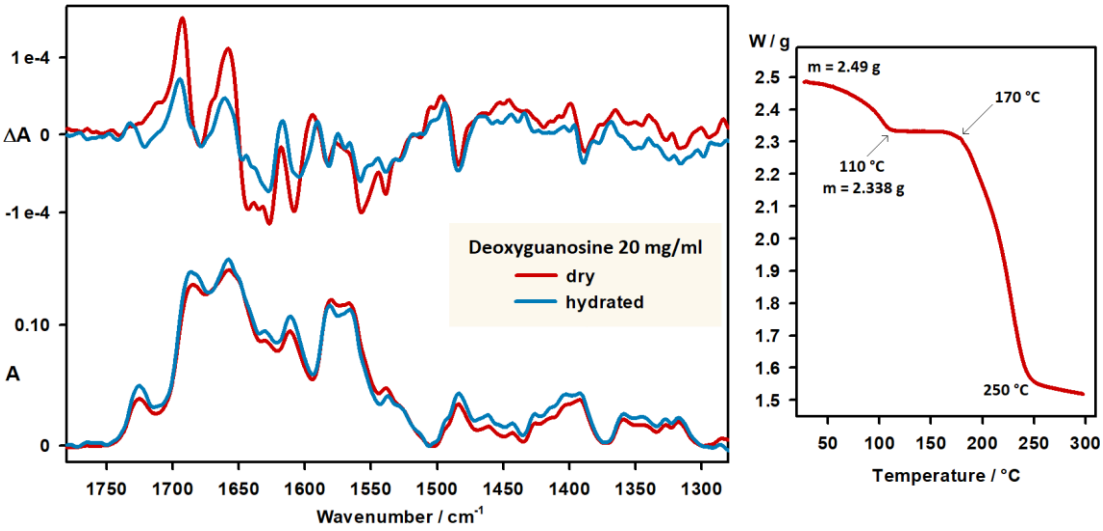

Figure 52. Left: IR and VCD spectra of dry and hydrated 2'-deoxyguanosine in D_2O. Right: Thermogravimetry curve for 2'-deoxyguanosine, dried in the vacuum at 50 °C for 12 hours beforehand.

IR and VCD spectra of both *D*- and *L*-enantiomers of guanosine are shown in **Figure 53**. As expected, the absorption spectra are almost the same. VCD spectrum of *L*-guanosine (L-G) is flipped with respect to natural guanosine and almost 3× less intense (*g*-factor for L-G 1.8×10^{-2}, *g*-factor for G 5.4×10^{-2}). This can be probably connected to the absence of large crystals in the suspension which may result in less ordered structure and weaker VCD signal. Next, we compared VCD spectra of dry and hydrated *L*-guanosine (**Figure 54**). The main VCD bands remain the same and the hydration does not trigger a flip of the sign of the ~1730 cm^{-1} couplet as in natural guanosine. Since L-D is a synthetic nucleoside, trace impurities introduced during the

synthesis may prevent formation of regular crystals, which may affect incorporation of water molecules into the crystal.

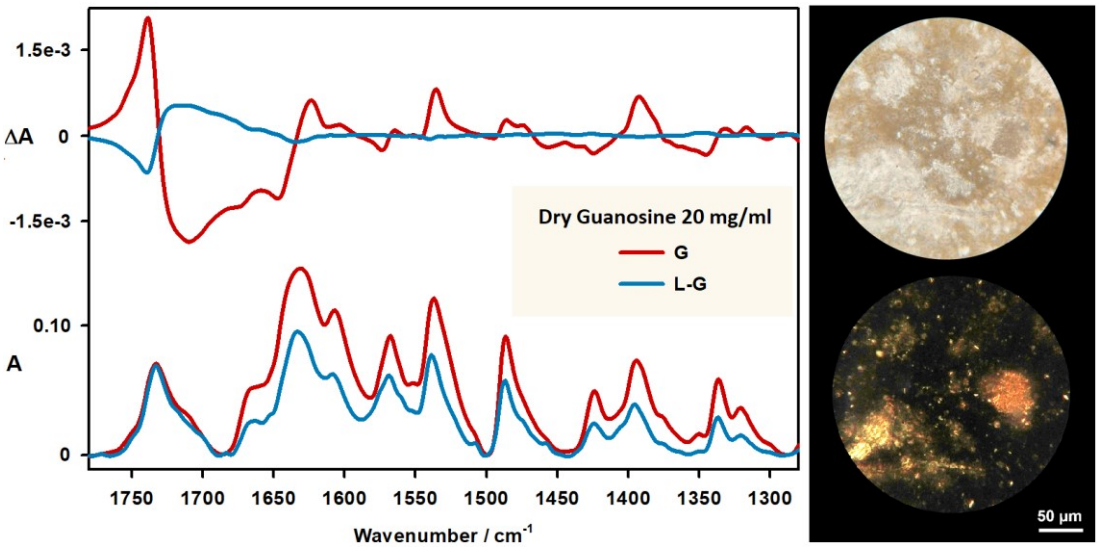

Figure 53. IR and VCD spectra of dry *D*-guanosine (G) and *L*-guanosine (L-G) in D_2O; microscopic images of L-G crystals (top: 45× magnification, phase contrast; bottom: 45× magnification, polarization mode).

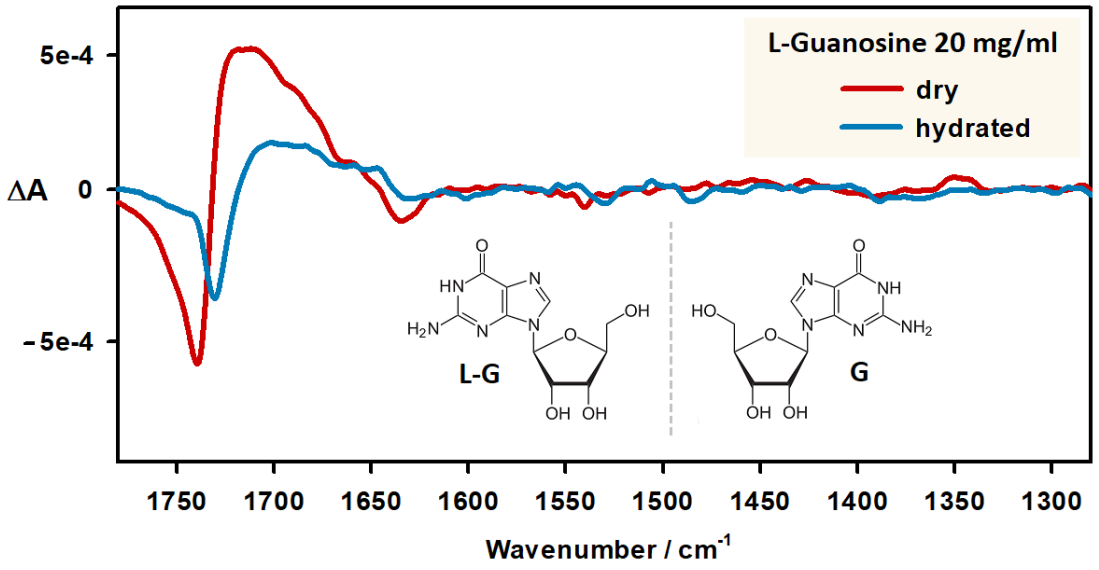

Figure 54. VCD spectra of dry and hydrated *L*-guanosine in D_2O.

Adenosine (A) crystallizes into relatively big blocks up to 25-40 μm thick and about 70-100 μm long. In **Figure 55**, the IR absorption and VCD spectra of dry and hydrated crystals are shown. In IR, the most intense band at 1624 cm^{-1} corresponds to C=N and C=C ring vibrations of adenine.[301] Less intense bands also belong to various ring vibrations of adenine. VCD is strong (*g*-factor 2×10^{-2} for hydrated adenosine), although weaker than for guanosine. Dry and hydrated adenosines give the same spectra. Indeed, as shown by TGA and X-ray analyses, adenosine crystals do not hydrate.

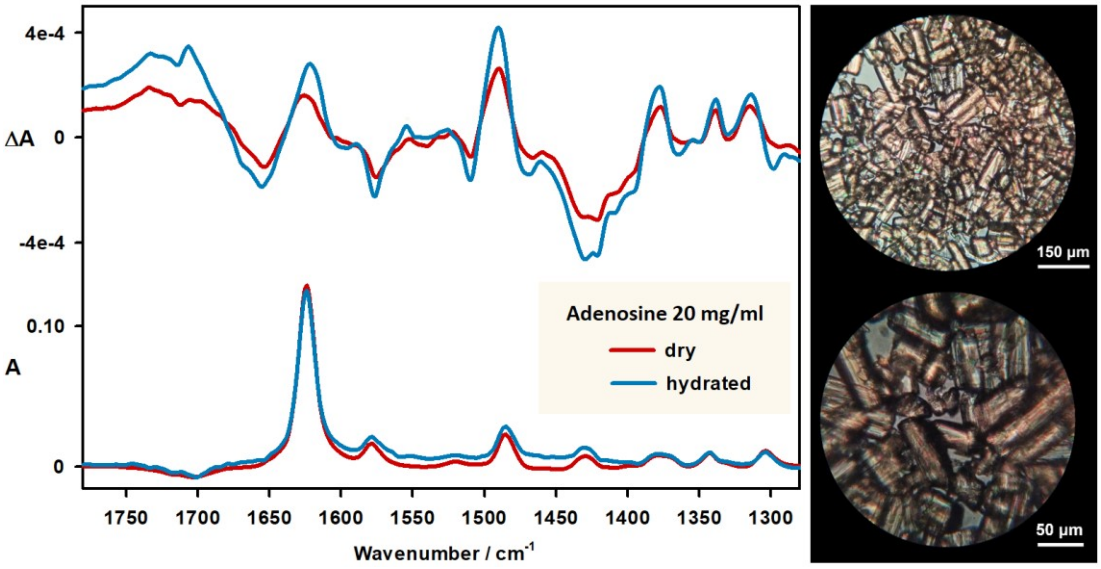

Figure 55. IR absorption and VCD spectra of dry and hydrated adenosine in D_2O. The spectra are accompanied by microscopic images of adenosine crystals (top: 20× magnification, bright field; bottom: 45× magnification, bright field).

In all experiments the samples were rotated during acquisition of the spectra. In this way, the polarization artifacts are minimized, although some may still be present. Therefore, we also flipped the sample cell along the axis perpendicular to IR beam and recorded the absorption and VCD spectra of hydrated guanosine (**Figure 56**). Only minor alterations in absorption spectra were observed; VCD spectra were even less sensitive. Since guanosine crystals are fairly small, they can orient randomly in the cell, and therefore VCD signal reflects average crystal chirality.

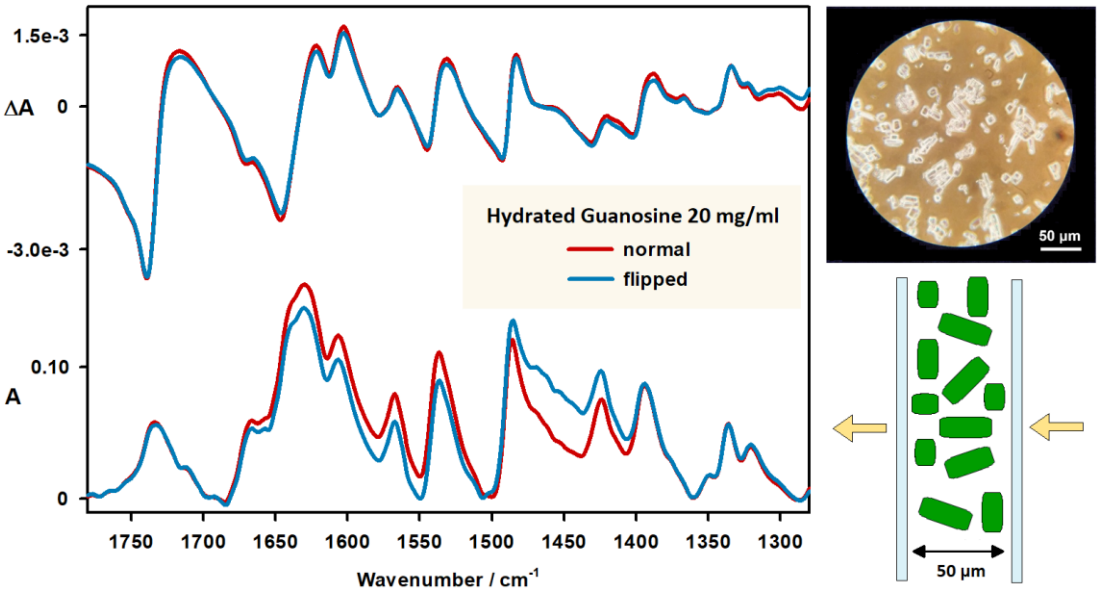

Figure 56. IR and VCD spectra of hydrated guanosine in two sample orientations: normal and flipped with respect to the direction of IR beam; microscopic image of guanosine crystals (3 mg/mL; 45× magnification, phase contrast), the crystals are much smaller than the pathlength of the cell used for VCD measurement (50 µm).

This was different for adenosine crystal suspension. Some VCD bands were opposite after the cell flipping (**Figure 57**). Moreover, VCD changed when the "same" experiment was repeated. Adenosine crystals are longer than VCD cell pathlength, they can orient randomly only in two directions and therefore they cause a lot of artifacts in the VCD spectrum. To further investigate if the propensity of adenosine VCD to artifacts is connected to the size of the crystals, we grinded the adenosine powder in a mortar and collected absorption and VCD spectra of such "crushed" crystal suspensions (**Figure 58**). The size of such crystals was between 10 – 20 µm. The orientational artifacts in the spectra were still present, although to a much smaller extent. Interestingly, crushed adenosine crystals show slightly smaller VCD signal enhancement when compared to "normal" A crystal VCD; *g*-factor for "crushed" A is 1.4×10^{-2}, while for larger adenosine crystals it is 2×10^{-2}. This further shows the importance of extended ordered structure for VCD enhancement.

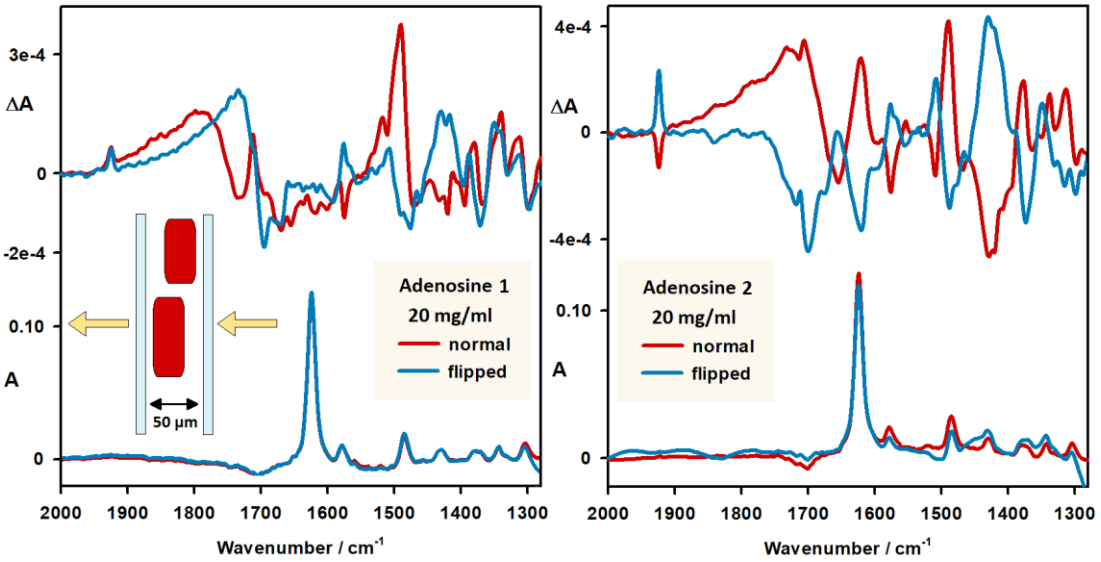

Figure 57. Two independent IR and VCD measurements (1, 2) of adenosine crystal suspension (large crystals) in two sample orientations: normal and flipped with respect to the direction of IR beam.

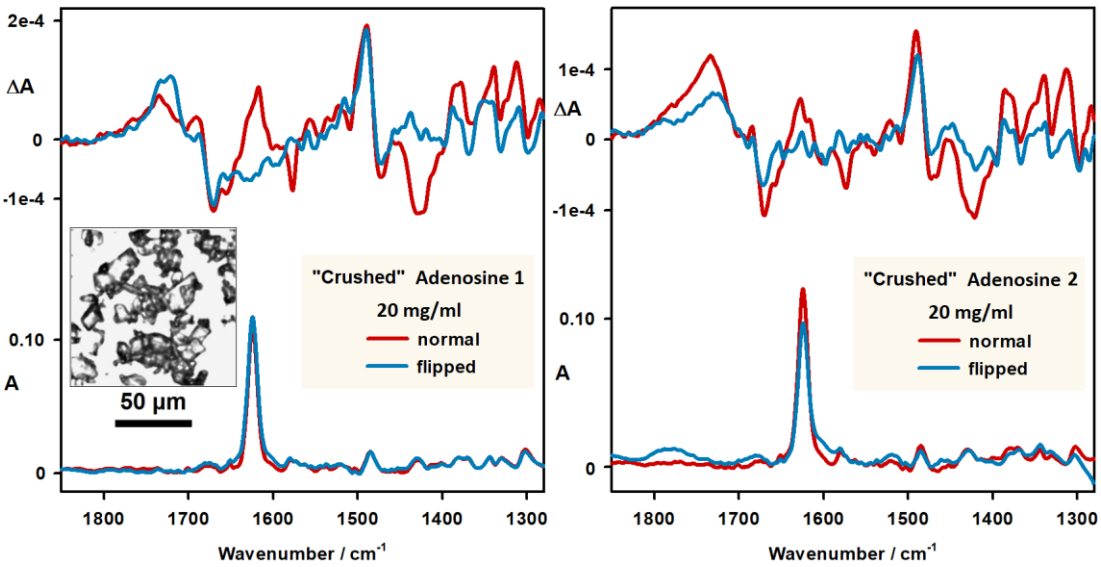

Figure 58. Two independent IR and VCD measurements of smaller "crushed" adenosine crystals in suspension in two sample orientations: normal and flipped with respect to the direction of IR beam.

The enhanced VCD was previously linked to the chiral arrangement of oscillators in many crystal layers.[169] We observed it for all studied crystalline nucleoside suspensions (**Figure 59**). The highest *g*-factor was observed for guanosine

crystals (~8×10^{-2}), and 2'-deoxyguanosine spectra showed the lowest *g*-factor (~2×10^{-3}). This may be caused by a higher solubility of dG when compared to G. Adenosine and *L*-guanosine crystals provided spectra with similar *g*-factors. In adenosine, smaller VCD compared to G crystals may be explained by the different packing of the chromophores and higher solubility. In the case of *L*-guanosine, the *g*-factor was lower when compared to G probably due to the lower regularity and smaller size of the L-G crystals. Nonetheless, all of the nucleoside suspensions showed at least ~1 order of magnitude higher *g*-factors when compared to B-DNA (5×10^{-4}).[63]

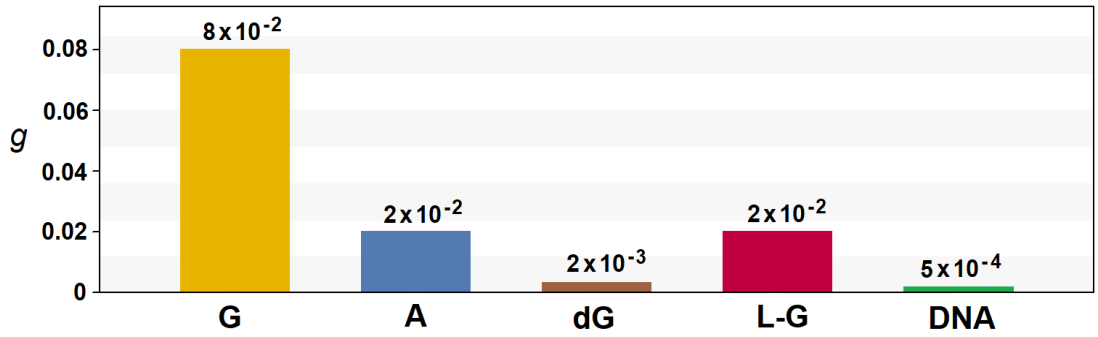

Figure 59. Maximal *g*-factors measured for selected nucleosides (20 mg/mL) and B-DNA (30 mg/mL).

In a publication in preparation, we are going to report the exceptional sensitivity of VCD to guanosine hydration, which is experimentally well-established. We observed also other effects (imbalance of *D*- and *L*-guanosine chirality and orientational effects and artifacts in adenosine crystal spectra), analysis of which will be done in the future.

4. Magnetic Circular Dichroism of Ln^{3+} Ions

Trivalent lanthanide ions are used in a variety of applications such as medical diagnostics, fluorescent probes of molecular structure, nanomaterials, magnets or solar cells.[128, 130, 303-305] They can form a variety of coordination compounds. Since their spectroscopic properties are highly dependent on the particular positioning of the ligands around the Ln^{3+} ion, they are used as sensitive probes of the chemical environment.[139] The environment affects also spectroscopic properties of Ln^{3+} ions in solutions. We used magnetic circular dichroism spectroscopy to study the effect of Ln^{3+} solvation on electronic transitions within the *f*-shell. MCD can potentially be more sensitive or bring additional information to absorption. To understand the absorption and MCD of selected Ln chlorides and nitrates, the experimental spectra were measured and compared to spectra simulated by two methods: the crystal field theory (CFT) model, and multi-state complete active space calculations with second order perturbation correction (MS-CASPT2).

Crystal field theory developed in late 1920s[306-308] describes the splitting of originally degenerate electron states (in a free atom) in the static electric field produced by a surrounding charge distribution (in a molecule). Such a fairly simple model was first used to explain a wide range of properties exhibited by transition metal complexes such as their color, structure, reactivity or magnetic properties. In transition metals, for example, the *d*-orbitals closer to the ligands repel each other, which results in the energy splitting. The magnitude is affected by many factors, such as the type of metal ion, its oxidation state, or ligands. The most important factor is often the arrangement or symmetry of the ligands around the metal ion (**Figure 60**).

Crystal field theory can be also applied to *4f* orbitals of lanthanides, even though these are generally much less susceptible to crystal field splitting than *d*-orbitals. This is because they are located much closer to the metal nucleus and they are shielded by *5s* and *5p* orbitals (**Figure 61**). Also, for the *f*-elements, the spin-orbit coupling energy is generally larger than the effect of crystal field. Therefore, the crystal field is acting as a perturbation to the spin-orbit splitting of energy levels.[309]

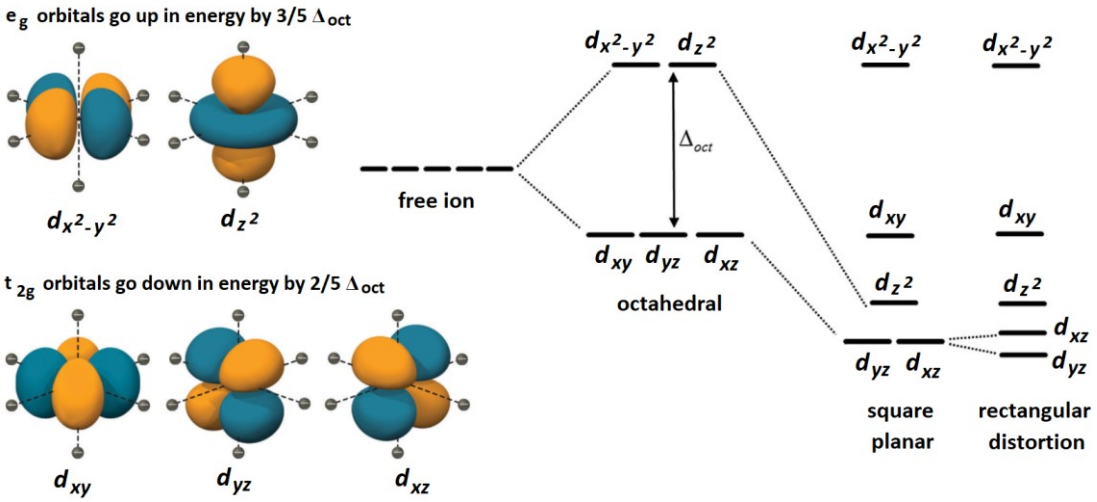

Figure 60. Application of crystal field theory to *d*-orbitals.[310] Octahedral crystal field causes splitting of 5 originally degenerate *d*-orbitals into two groups: e_g and t_{2g} separated by Δ_{oct} energy. The magnitude of Δ_{oct} depends on the type of ligands surrounding the central ion. Orbital energy splitting is different in various geometries.

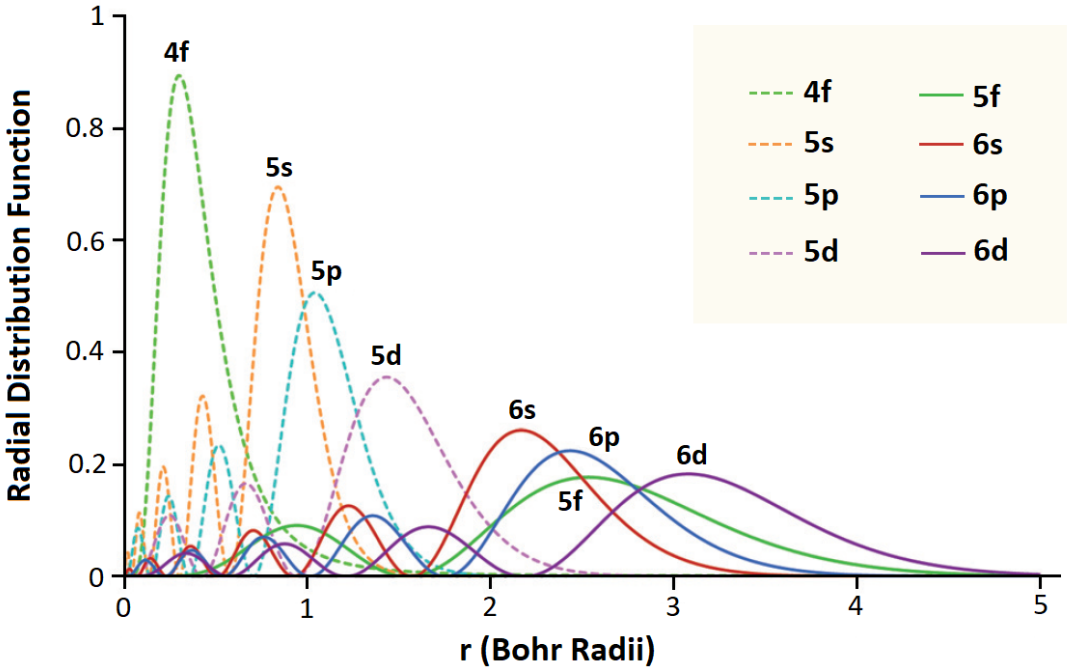

Figure 61. The radial distribution functions for *4f*, *5s*, *5p*, *5d*, *5f*, *6s*, *6p* and *6d* orbitals.[311]

Figure 62 shows the effect of various perturbations on the ground state energy levels of Dy^{3+} ion. Nine electrons in Dy^{3+} ion occupy seven *4f* orbitals giving rise to the ^6H ground state with the total spin $S = 5/2$ and the orbital angular momentum $L =$

5. This state is further split by spin-orbit coupling to different *J*-states. Each *J*-state of the free ion is (*2J + 1*)-fold degenerate; each substate can be characterized by a magnetic quantum number m_J (*+J, J–1, J–2, ... , –J*). The crystal field removes this degeneracy between m_J substates.

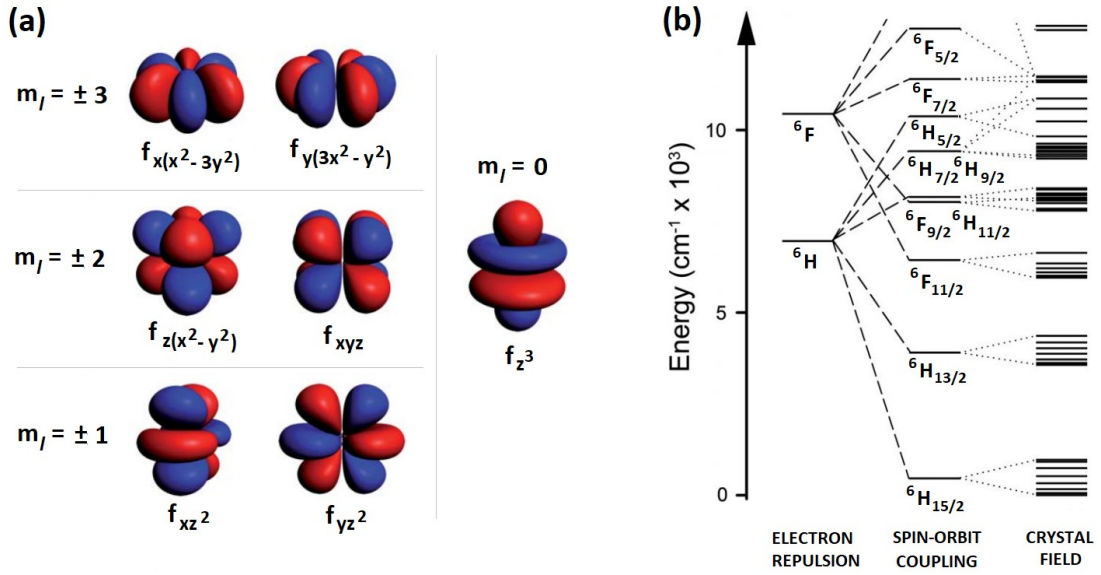

Figure 62. (a) Real representation of *4f* orbitals. Orbitals with high m_l are oblate, while low m_l orbitals are more prolate. **(b)** Low energy levels of the Dy^{3+} ion, and the effects of perturbation by electron-electron repulsion, spin-orbit coupling and crystal field.[309] In the term symbols $^{M}L_J$, $M = 2S+1$ is spin multiplicity connected to the total spin quantum number *S*, *L* is the total orbital quantum momentum number in spectroscopic notation (0 = S, 1 = P, 2 = D, 3 = F, …) and *J* is the total angular momentum.

Due to lanthanides' complicated electronic structure, usage of *ab initio* methods for calculations of their spectra is limited. Therefore, parametric approaches such as CFT are often used to describe lanthanide energy levels with impressive accuracy.[225, 312] Since transitions within the *f*-shell of lanthanides are electric-dipole forbidden, the mixing of the *f* and *d* electronic levels due to the external crystal field is usually considered as a way to explain the spectroscopic properties.[313-315] This is the basic concept of the Judd-Ofelt theory that explains observed intensities in lanthanide absorption spectra.[316] The symmetry and strength of the crystal field around the Ln^{3+} ion therefore determines the absorption, MCD, luminescence, CPL, etc.[139, 140, 317]

Lately, also *ab initio* methods became available for calculation of lanthanide spectroscopic parameters.[318-320] In the present work, we combine the CFT with molecular dynamics, which does not give accurate intensities, but allows us to study the interplay between the spectral intensities and lanthanide ion environment. A similar approach was also used before to identify the Ln^{3+} transitions in magnetic circularly polarized luminescence.[151]

We use *ab initio* approach based on the multi-state complete active space calculations with second order perturbation correction (MS-CASPT2) for smaller systems.[321-323] The CASPT2 method[324, 325] offers relatively accurate solutions for multireference systems with reasonable computational effort. Several implementations of CASPT2 method are available in widely used software packages such as MOLCAS[326] or MOLPRO.[327] CASPT2 method combines a multiconfigurational complete active space (CAS) wavefunction[328] that accounts for the static correlation effects and second order perturbation correction that adds the dynamic correlation effects. It can be also used for excited electronic states.

In CASSCF (CAS self-consistent field), molecular orbitals (MOs) are partitioned into three groups: inactive orbitals are doubly occupied and do not participate in configuration interaction (CI); active orbitals whose occupancy differs in various configurations; and virtual orbitals that remain unoccupied in all configurations. Orbital energies generally increase in the order *inactive* < *active* < *virtual*. The number of possible configurations increases exponentially with the number of active orbitals and active electrons.[329] Therefore, only a limited number of MOs can be included in the active space; usually some of the highest occupied and some of the lowest unoccupied MOs are included. The selection of the active space has a significant effect on the results; a careful examination of underlying electronic structure is necessary.[330] Various approaches such as restricted active space (RAS) can be used to limit the number of possible configurations within the active space.[331] An overview of CI, CAS and RAS methods can be found in **Figure 63**.

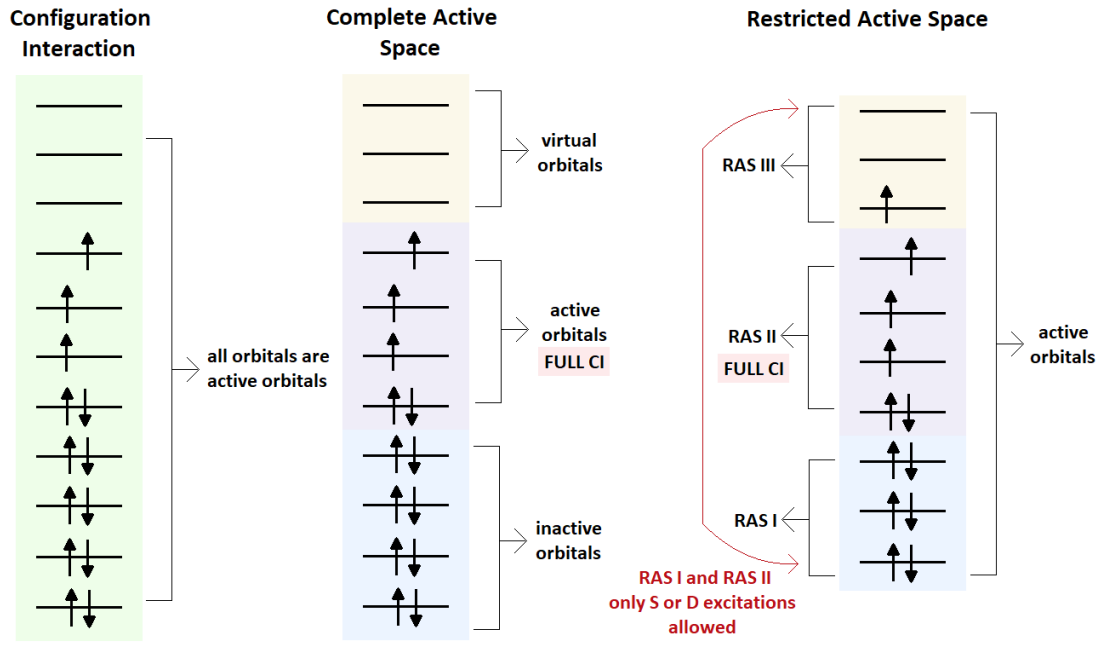

Figure 63. The CI, CAS and RAS methods. In full CI, all of the molecular orbitals are considered active and excitations of all orders are allowed. In CAS, the orbitals are divided into three groups, only the active ones participate in full CI. In RAS, the active orbitals are divided into subgroups, in which the excitations are limited.

Within the active space, the full CI is performed. CASSCF optimizes both the orbital coefficients and the CI coefficients. For excited states, a state-averaging scheme is usually used.[329] The active space is characterized by a CAS(n,m) notation, which means that *n* active electrons are distributed over *m* active orbitals. CASSCF states are then used as the zeroth-order states for PT calculations. The first-order perturbed wavefunctions and second-order perturbation energies account for the finer dynamic correlation.

To calculate MCD intensities from CASPT2 states, we used a first-principles method proposed earlier[161] that directly estimates the difference between the left- and right-circularly polarized light transition probabilities in external magnetic field. In this approach, quasi-degenerate perturbation theory is used to account for the spin-orbit coupling (SOC), spin-spin coupling (SSC) and Zeeman interaction. A wavefunction from MS-CASPT2 is obtained in the form of eq. 47, where indices *SS* correspond to the spin quantum number *S* and the spin projection $M_S = S$. The SOC, SSC and Zeeman interactions are evaluated in the basis of preselected solutions of

Born-Oppenheimer (BO) Hamiltonian $\{\Psi_l^{SM}\}$ (eq. 48). The diagonalization of this matrix gives the energy levels and wave functions of the coupled states. The detailed calculation of SOC and SSC matrix elements is described elsewhere.[161]

$$\left|\Psi_l^{SS}\right\rangle = \sum_\mu C_{\mu l}\left|\phi_\mu^{SS}\right\rangle \tag{47}$$

$$\left\langle\Psi_l^{SM}\middle|\hat{H}_{BO} + \hat{H}_{SOC} + \hat{H}_{SSC} + \hat{H}_Z\middle|\Psi_J^{S'M'}\right\rangle = \tag{48}$$

$$= \delta_{lJ}\delta_{SS'}\delta_{MM'}E_l^{(S)} + \left\langle\Psi_l^{SM}\middle|\hat{H}_{SOC} + \hat{H}_{SSC} + \hat{H}_Z\middle|\Psi_J^{S'M'}\right\rangle$$

$$H_{Zeeman} = \beta_e(\mathbf{L} + g_e\mathbf{S}).\mathbf{B} \tag{49}$$

$$\frac{\Delta\varepsilon}{E} = \gamma\sum_{a,j}\left(N_a - N_j\right)\left(\left|\left\langle\Psi_a\middle|\mu_{LCP}\middle|\Psi_j\right\rangle\right|^2 - \left|\left\langle\Psi_a\middle|\mu_{RCP}\middle|\Psi_j\right\rangle\right|^2\right)f(E) \tag{50}$$

The Zeeman terms between the electronic states are included in the form of eq. 49, where $\mathbf{L} = \sum_i \mathbf{l}(i)$ is angular momentum, **S** is total spin quantum number, g_e is free-electron g factor, **B** is magnetic field and β_e is Bohr magneton. After the diagonalization of the SOC, SSC and Zeeman operator matrices, the produced eigenvectors are used to calculate the transition dipole moments which are further used to calculate the MCD intensity (eq. 50; *a* and *j* label the initial and excited states, *E* is the energy of incident radiation, $\Delta\varepsilon$ is the difference in extinction coefficients for right- and left-circularly polarized light, N_x is the Boltzmann population of the x^{th} state sublevel at a given energy, *f(E)* stands for line shape function, γ is a collection of constants, and μ_{LPC} and μ_{RPC} correspond to the electric dipole operators for left- and right-circularly polarized light).[161, 332]

4.1. Methods

4.1.1. Magnetic Circular Dichroism Spectra

Lanthanide salts ($LnCl_3$ or $Ln(NO_3)_3$, obtained from *Sigma-Aldrich*) were dissolved in H_2O to the concentration of 30 mg/mL. To observe transitions with low intensity, some lanthanides were measured in solutions with higher concentration

(~1000 mg/mL). UV-VIS absorption and MCD spectra were measured at room temperature with *Jasco J-815* spectrometer equipped with a 1.5 T permanent magnet in a quartz cell of 0.1 cm optical pathlength. The spectra were recorded for both magnet orientations (N or S side facing the detector) in the 180 – 850 nm range using 0.5 nm resolution, 4 s response time, and a scanning speed of 20 nm/min. In total, three accumulations were averaged. Finally, the solvent spectra acquired at identical conditions were subtracted from those of the samples. The experimental intensity of absorption and MCD is presented in ε and Δε, respectively (units: $L.mol^{-1}.cm^{-1}$).

4.1.2. Simulations of Ln^{3+} MCD Spectra

Molecular dynamics simulations were performed to acquire Ln^{3+}/H_2O cluster geometries. Representative "snapshots" were selected, solvent molecules outside of the first hydration shell were deleted, and a partial geometry optimization of such clusters was performed at a DFT level. Next, two approaches were used to calculate the absorption and MCD spectra: a parametrized CFT model, and MS-CASPT2 calculations. **Figure 64** schematically illustrates this workflow.

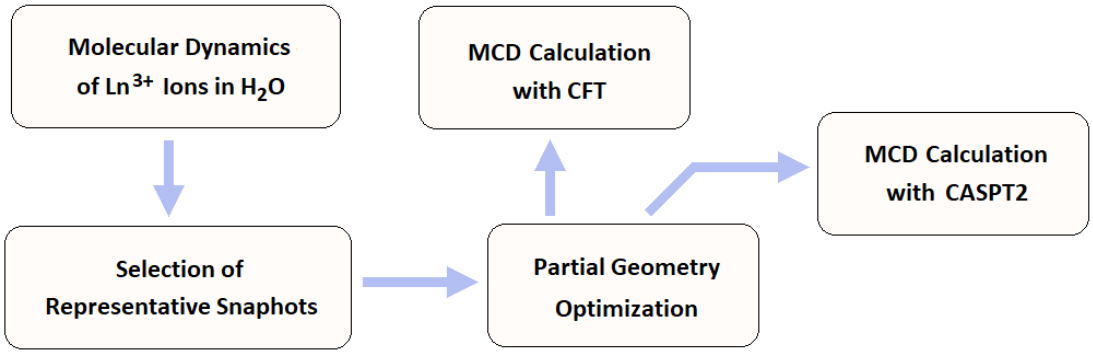

Figure 64. Flow of calculations of MCD spectra of hydrated Ln^{3+} ions.

4.1.2.1. Ln^{3+}/H_2O Cluster Geometries

For MD simulations, Ln^{3+} ions were placed into a 15 Å cubic box filled with water molecules. After 100 ps equilibration, the productive MD was run for 30 ns with Amber10[333, 334] software (*NTV* thermodynamic ensemble at the temperature 300 K, 1

fs integration time, GAFF force field and periodic boundary conditions). During 30 ns simulation, a snapshot was saved each 10 ps producing 3000 snapshots in total. Water molecules outside a given sphere (**Table 8**) were deleted and the geometries of remaining clusters were partially optimized (in 3 optimization steps). The charge distribution around the Ln^{3+} ions was described by partial atomic charges or grid charge density. The quantum chemistry calculations were performed with the Gaussian09[335] software at B3LYP[336, 337] level with effective core potentials (ECP)[338] for each Ln^{3+} ion specified in **Table 8**. The Ln^{3+} ionic radii and the parameters for MD were taken from the literature.[339-341]

Table 8. Parameters used for the preparation of Ln^{3+}/H_2O geometries.

	Ce^{3+}	Pr^{3+}	Nd^{3+}	Sm^{3+}	Eu^{3+}
	$[Xe]4f^1$	$[Xe]4f^2$	$[Xe]4f^3$	$[Xe]4f^5$	$[Xe]4f^6$
r^A	3.9	3.9	3.9	3.8	3.6
X^B	47	48	49	51	52
	Gd^{3+}	Tb^{3+}	Dy^{3+}	Ho^{3+}	Er^{3+}
	$[Xe]4f^7$	$[Xe]4f^8$	$[Xe]4f^9$	$[Xe]4f^{10}$	$[Xe]4f^{11}$
r^A	3.7	3.7	3.7	3.7	3.7
X^B	53	54	55	56	57

A Radius of the Ln^{3+} first hydration shell [Å]. **B** Parameter of the effective core potential MWB[X].

4.1.2.2. Crystal Field Theory Calculations

Energy levels within the Ln^{3+} *f*-shell were calculated by the LANTHANIDE software by Åberg and Edvardsson.[342] The Hamiltonian can be expressed as a sum of free ion (H_{free}) and crystal field (H_{CF}) contributions (eq. 51).[225, 343] Free ion contribution can be described by eq. 52, where f_k is the angular part of the electrostatic interaction, A_{SO} corresponds to the angular part of the spin-orbit interaction, L is the orbital angular momentum, Casimir operators for the groups G_2 and R_7 are $G(G_2)$ and $G(R_7)$,

respectively, and t_i corresponds to the three particle operators. Parameters in the eq. 52 (electron repulsion parameter F^k, the spin-orbit coupling constant ξ, three body configuration interaction parameter T^i, and Trees configuration interaction parameters α, β and γ) used in our calculations were taken from the literature.[343]

$$H = H_{free} + H_{CF} \tag{51}$$

$$H_{free} = \sum_{k=2,4,6} F^k f_k + \xi A_{SO} + \alpha L^2 + \beta G(G_2) + \gamma G(R_7) + \\ + \sum_{i=2,3,4,6,7,8} T^i t_i \tag{52}$$

Crystal field contribution to the Hamiltonian can be divided into two parts: a potential V_q is caused by the partial atomic charges, and V_p is connected to the atomic polarizabilities (eq. 53). When expanded in spherical tensor operators $C_{im}(\vartheta,\phi)$ dependent on the angular spherical coordinates ϑ and ϕ, we get V_q in the form of eq. 54, where ε_0 is the vacuum permittivity, e_i and r_i represent the charge of the electron i and its distance from the lanthanide, r_{iL} is the distance between electron i and the ligand L, Q_L is its charge, r_L is the distance between the lanthanide and a ligand, and A_{im} is defined in the eq. 55. The index i runs over all electrons in the f-shell, and l index is cut off at $l = 7$, since higher terms give only negligible contributions.

$$H_{CF} = V = V_q + V_p \tag{53}$$

$$V_q = \frac{1}{4\pi\varepsilon_0} \sum_{i,L} \frac{e_i Q_L}{r_{iL}} = \sum_{i=1}^{n} \sum_{l=0}^{7} \sum_{m=-l}^{l} r_i^l A_{im} C_{im}(\vartheta_i, \phi_i) \tag{54}$$

$$A_{im} = \sum_L (-1)^{l+1} \frac{Q_L}{r_L^{l+1}} C_{l-m}(\vartheta_L, \phi_L) \tag{55}$$

Likewise, V_p can be expressed in a similar form (eq. 56), where A_{imn} is described by eq. 57. The coefficients P_α were generated by an additional program, and the expansion of V_p was restricted to $n_{i\alpha} = l_{max} = 7$.

$$V_p = \sum_{\alpha=1}^{m} P_\alpha \sum_i r_i^{n_\alpha} A_{imn} C_{im}(\vartheta_i, \phi_i) \tag{56}$$

$$A_{imn} = -\frac{1}{4\pi\varepsilon_0} \sum_L \frac{\alpha_L}{r_L^{n_{L\alpha}}} C_{l_{L\alpha} m_{L\alpha}}(\vartheta_L, \phi_L) \tag{57}$$

Transitions within the *f*-shell in the non-relativistic model are dipole forbidden. To model spectral intensities, coupling of the *f*-states with others must be considered. The initial $\langle A|$ and final $|B\rangle$ states of a transition $A \rightarrow B$ can be described by eq. 58. One-electron spinorbitals (eq. 59) are used as basis functions ($l_1 = l_2 = \ldots = l_n = l$, s_i are spins and m_i are magnetic quantum numbers). The crystal field perturbation V mixes the states, and the first order-corrected A and B states are expressed in eq. 60 and 61, where E_i are unperturbed state energies.

$$\Psi_A = |A\rangle = \sum_q C_q^A \, |l^n q\rangle \tag{58}$$

$$|l^n q\rangle = \left\{\left|l_1 m_{1q} s_{1q}\right\rangle \left|l_2 m_{2q} s_{2q}\right\rangle \ldots \left|l_n m_{nq} s_{nq}\right\rangle\right\} \tag{59}$$

$$\left\langle A'\right| = \langle A| + \sum_{u \neq A} \frac{\langle A|V^*|u\rangle}{E_A - E_u} \langle u| \tag{60}$$

$$\left\langle B'\right| = \langle B| + \sum_{u \neq B} \frac{\langle u|V|B\rangle}{E_B - E_u} |u\rangle \tag{61}$$

The largest contribution comes from the excited states $|u\rangle = \left|l^{n-1} l'\right\rangle$ where one electron of the *l*-shell is moved to another shell, e.g. $|u\rangle = |f^{n-1} d\rangle$.[344] The absorption band area is proportional to total dipolar strength D, which can be divided into two parts: dipolar strength connected to electric dipole moments D_E and magnetic dipolar strength D_M (eq. 62 – 64, **m** is a magnetic dipole, **μ** is an electric dipole and χ is a parameter).

$$D = D_E + D_M \tag{62}$$

$$D_E = \left\langle A'\right|\boldsymbol{\mu}\left|B'\right\rangle \cdot \left\langle B'\right|\boldsymbol{\mu}\left|A'\right\rangle \tag{63}$$

$$D_M = \chi\left\langle A'\right|\mathbf{m}\left|B'\right\rangle \cdot \left\langle B'\right|\mathbf{m}\left|A'\right\rangle \tag{64}$$

Unlike electric dipole moments, magnetic dipole moments are non-zero even for *f*-shell transitions. The expression for electric dipole moment matrix element is shown in eq. 65, with the effective dipole moment specified in eq. 66. The index α corresponds to *x, y* and *z* directions. Transition magnetic dipole moment can be expressed as in eq. 67 where **L** and **S** correspond to the orbital angular moment and

spin operators, respectively. The Faraday *B* term for MCD intensities can be calculated by expression 68.[159, 160] Also, the Faraday *A* term can be extracted from eq. 67 by arbitrary degeneracy lifting.[159] The Faraday *C* term is generally negligible at room temperature.

$$\langle A'|\mu_\alpha|B'\rangle = \mu_{\alpha AB} \cong \sum_{q,q'} C_q^{A*} C_{q'}^{B} \langle l^n q|\mu_\alpha|l^n q'\rangle_{eff} \tag{65}$$

$$\langle l^n q|\mathbf{\mu}|l^n q'\rangle_{eff} = K \sum_{u\neq B}\langle l^n q|\mathbf{\mu}|u\rangle\langle u|V|l^n q'\rangle + \\ + \sum_{u\neq A}\langle l^n q|V^*|u\rangle\langle u|\mathbf{\mu}|l^n q'\rangle \tag{66}$$

$$\langle A'|\mathbf{m}|B'\rangle = \mathbf{m}_{AB} = \sum_{q,q'} C_q^{A*} C_{q'}^{B} \langle l^n q|\mathbf{L} + 2\mathbf{S}|l^n q'\rangle \tag{67}$$

$$B_{MCD} = Im\left[\sum_{C\neq A} \frac{\mathbf{m}_{CA}\cdot\mathbf{\mu}_{AB}\times\mu_{BC}}{E_{CA}} + \sum_{C\neq B} \frac{\mathbf{m}_{BC}\cdot\mathbf{\mu}_{AC}\times\mathbf{\mu}_{CA}}{E_{CB}}\right] \tag{68}$$

To describe the CFT potential, we used partial atomic (Mulliken) charges or charge density extracted from Gaussian09 output. The convergence of calculated absorption and MCD spectra on the number of averaged molecular dynamics snapshots was evaluated as a root-mean-square deviation (RMSD) of succesive averages from the total average.

4.1.2.3. MS-CASPT2 Calculations

All CASSCF and MS-CASPT2 calculations were performed with the ORZ program developed by T. Yanai and co-workers. Most of the results were obtained from calculations with the active space composed of only *4f* lanthanide orbitals, and state-averaging (SA-CASSCF) over all components of the generally orbitally degenerate ground states was employed during the orbital optimization. Our testing calculations suggest that the significantly more expensive CASSCF orbital optimization involving state-averaging over both ground and excited states is not necessary, as it leads to fairly minor changes in the calculated spectra. This seems logical if we realize that each of the seven *4f* lanthanide orbitals is optimized on the same footing even when only the ground state is considered. In addition, calculations

with the active space composed of both *4f* and *5d* lanthanide orbitals were performed for ions where $f \rightarrow d$ transitions were observed experimentally. In this case, we used the minimal number of states which ensures that all *f* and all *d* orbitals are "equally" optimized (for example, SA-CASSCF orbital optimization for Ce^{3+} involved all components of ^2F ground state and ^2D excited state). The number of states of various spin multiplicities included in the final MS-CASPT2 / CASCI calculations was chosen to cover the measured spectral region (from few tens to few hundreds of states were used). The calculated spectral intesities of $f \rightarrow d$ transitions are heavily overestimated, which strongly affects also the intensities of $f \rightarrow f$ transitions. Thus, the active space composed of both *f* and *d* orbitals was used only to describe the $f \rightarrow d$ transitions, and results for all $f \rightarrow f$ transitions were taken from the calculations with only *f* orbitals in the active space.

Throughout the work, ANO-RCC[345-347] basis set combining the QZP and DZP (quadruple and double zeta basis sets, respectively) quality was used (contracted to [9*s* 8*p* 5*d* 4*f* 3*g* 2*h*] for lanthanides, [3*s* 2*p* 1*d*] for O and [2*s* 1*p*] for H). In all MS-CASPT2 calculations, IPEA[348] and imaginary[349] level shifts of 0.25 and i0.2 a.u. were used, respectively, and orbitals up to lanthanides' *4d* were kept frozen (*5s* and *5p* shells were correlated). The second-order Douglas–Kroll–Hess (DKH2) transformation was applied to the one-electron scalar terms,[350-352] spin–orbit coupling,[353] and Zeeman terms.[353, 354] SOC integrals were evaluated using the flexible nuclear screening spin–orbit (FNSSO)[355] approximation.

For the calculations of absorption spectra, the SOC effects were included via the state interaction method.[356] In case of magnetic circular dichroism, both SOC and Zeeman matrix elements between the precalculated states were involved in the state interaction, as proposed by Ganyushin and Neese.[161] The resulting quasi-relativistic states are explicitly split by the magnetic field, and MCD intensities are thus constructed only from the differences between absorption of left- and right-circularly polarized light. Experimental conditions were used for the MCD calculations; T = 293.15 K and B = 1.5 T. Origin of the angular momentum operator was placed to the lanthanides' coordinates.

4.2. Results and Discussion

Experimental absorption and MCD spectra of hydrated Ln^{3+} ions usually have many transitions within 240 – 850 nm (**Figure 65**). Spectra provided by Ce^{3+} and Pr^{3+} at the beginning of lanthanide series are simpler due to the low number of *4f* electrons that can participate in the transitions. Also, spectra provided by Gd^{3+} ion (electron configuration $[Xe]4f^7$) are simple, since there is a big energy gap between the ground and the lowest excited state (see **Figure 12**, p. 23).

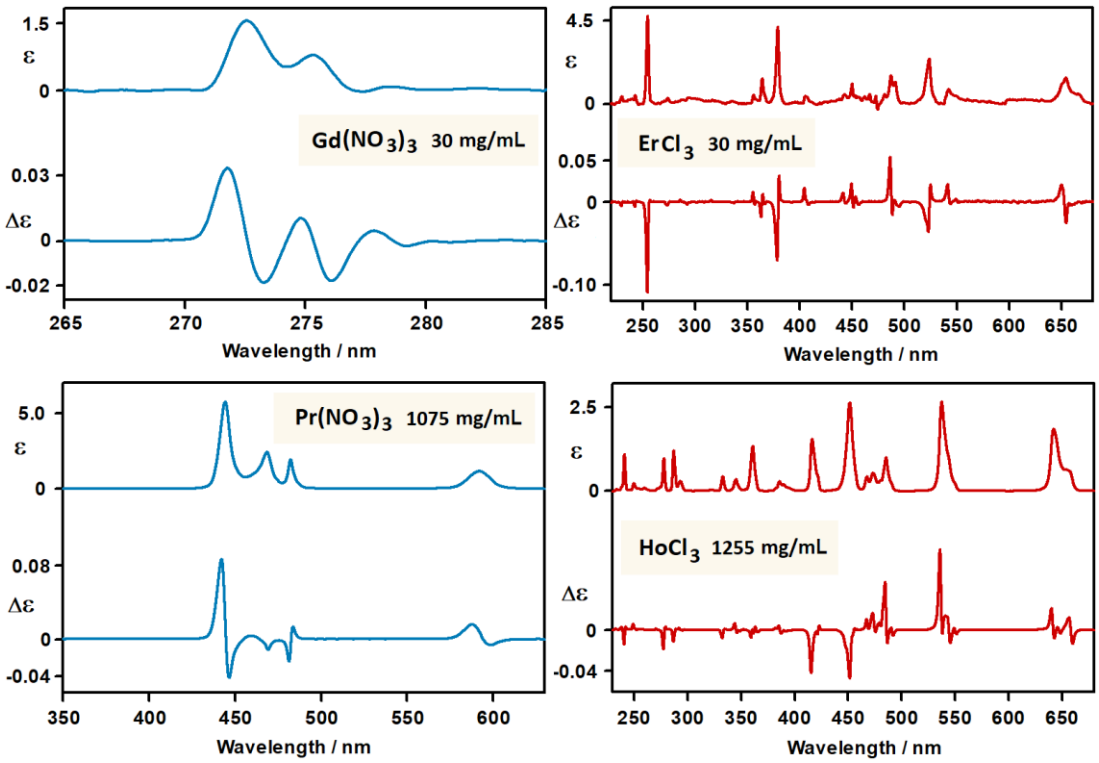

Figure 65. Absorption and MCD spectra (B = 1.5 T) of 4 selected lanthanides: $Gd(NO_3)_3$, $Pr(NO_3)_3$, $ErCl_3$ and $HoCl_3$.

In Ho^{3+} ion, the absorption lines are significantly wider. The ground state of Ho^{3+} ion $^5I_8$ is split by crystal field into 17 energy levels[225] which are almost degenerate and therefore more or less equally populated which then translates to a considerable line broadening. Another effect that contributes to the significant line broadening comes from the coupling of electronic states of the Ln^{3+} ion with the vibrations of the ligands. This effect is generally the least prominent in the middle of lanthanide series,

therefore Gd^{3+}, Eu^{3+} and Tb^{3+} show only minor line broadening due to the vibronic coupling.[225]

The hydrated Ln^{3+} ions were measured as nitrates or chlorides. As shown for absorption and MCD spectra of $NdCl_3$ and $Nd(NO_3)_3$ in **Figure 66a**, both salts provide more or less the same spectra within the experimental error. As expected, two orientations of magnet during spectra accumulation give rise to opposite signs of MCD peaks. This is illustrated in **Figure 66b** for experimental absorption and MCD spectra of $EuCl_3$. If not stated otherwise, we show only experimental spectra measured with magnet in N-orientation.

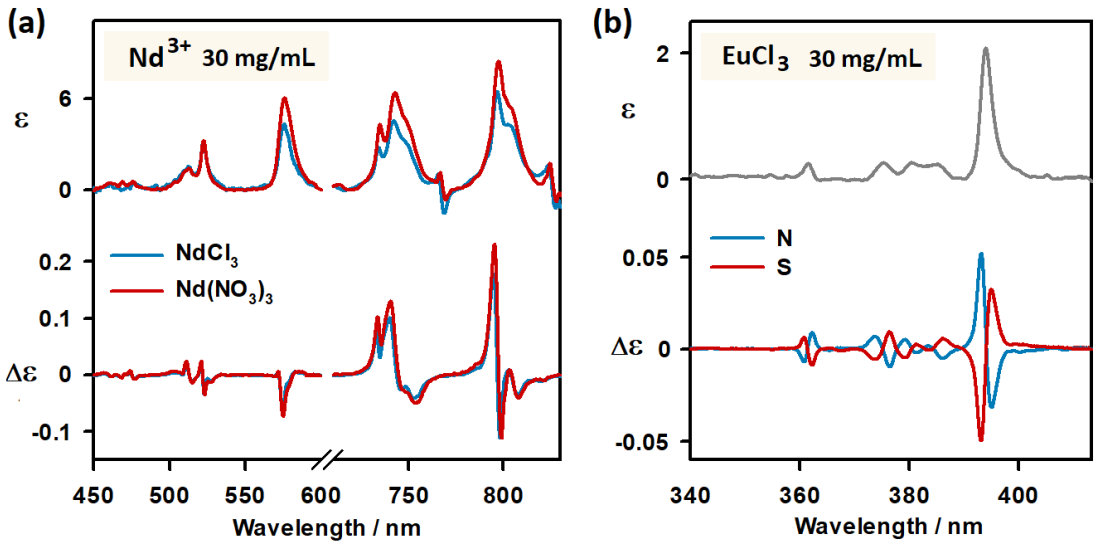

Figure 66. UV-Vis absorption and MCD spectra of hydrated Ln^{3+} ions (B = 1.5 T). **(a)** Nd^{3+} ion in the form of $NdCl_3$ and $Nd(NO_3)_3$. **(b)** $EuCl_3$ in two orientations of the magnet.

4.2.1. Interpretation of Molecular Dynamics Simulations

The number of H_2O molecules in the first hydration shell obtained by MD was specific for each ion. Ce^{3+}, Pr^{3+} or Nd^{3+} can accommodate up to 10 water molecules in their first hydration sphere. As the Ln^{3+} atomic number increases, the size of the ion decreases due to the lanthanide contraction. Therefore, the first hydration shell is reduced to 9 H_2O molecules for Sm^{3+} to Er^{3+}, and small ions such as Ho^{3+} and Er^{3+}

exist to some extent also in configurations with only 8 water molecules in their first hydration sphere. These trends are illustrated in **Figure 67**.

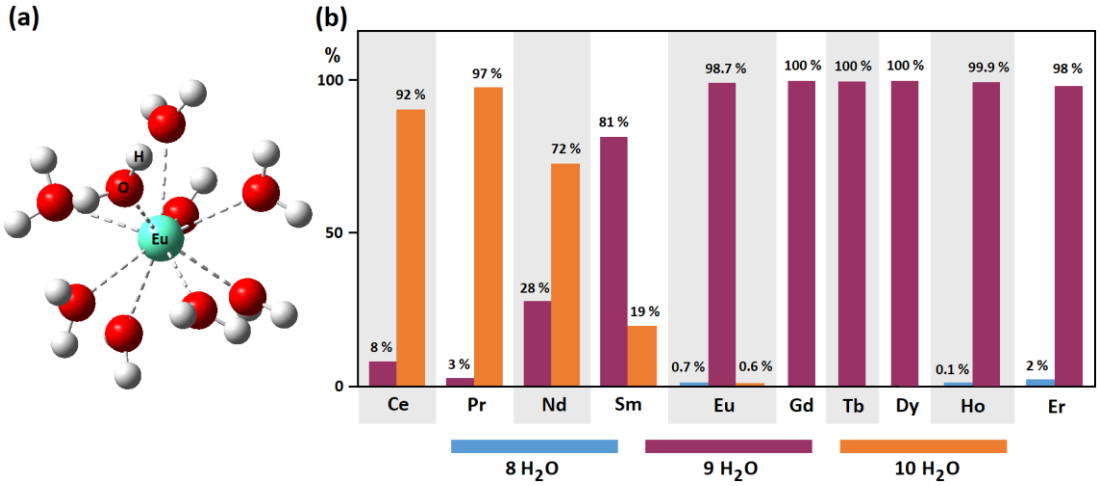

Figure 67. (a) A cluster of Eu^{3+} ion and 9 water molecules. **(b)** Distribution of the number of H_2O molecules in the first solvation sphere of the Ln^{3+} ions based on the analysis of 3000 MD snapshots.

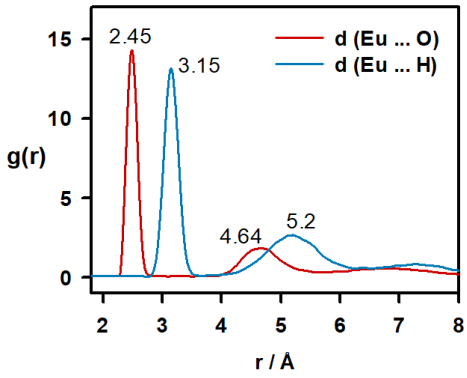

	Ce	Pr	Nd	Sm	Eu
1st O	2.62	2.63	2.57	2.51	2.45
2nd O	4.81	4.87	4.75	4.67	4.64
1st H	3.3	3.3	3.24	3.2	3.15
2nd H	5.4	5.34	5.32	5.3	5.2

	Gd	Tb	Dy	Ho	Er
1st O	2.5	2.46	2.44	2.43	2.38
2nd O	4.63	4.61	4.6	4.56	4.6
1st H	3.2	3.14	3.1	3.1	3.1
2nd H	5.2	5.22	5.18	5.2	5.1

Figure 68. Left: Radial distribution functions of water's hydrogen and oxygen atoms in first and second hydration spheres of the Eu^{3+} ion. Right: The mean distances between the Ln^{3+} ions and hydrogens and oxygens in the 1st and 2nd hydration shells.

The first solvation sphere of Ln^{3+} ions is relatively well-defined; the radial distribution function for Eu^{3+}/H_2O is plotted in **Figure 68**. The average Eu-O distance was calculated as 2.45 Å and it fluctuates only little around this value (± ~0.25 Å). The

oxygens from the 2nd hydration shell are distributed at ~4.64 Å from the Eu^{3+} ion; their distribution varies more significantly (± ~0.45 Å). The closest hydrogens are located at the average distance of 3.15 Å, and their distance probability is dispersed more because of the wagging motion of the water molecules. Similar results were obtained for other lanthanides.

4.2.2. Simulations of Eu^{3+}/H_2O MCD Spectra

The strongest bands in UV-Vis absorption spectrum of aqueous Eu^{3+} ion belong to transitions from the $^7F_0$ ground state. The $^7F_0$ level is populated by 65 % of ions at room temperature. Transitions from the $^7F_1$ electronic level are less intense, because this level is populated by only about 35 % of ions at room temperature. Transitions from the $^7F_2$ level are very weak and usually not observed.[225] The bands originating in $^7F_1$ level are broader than those for $^7F_0$. The strongest transitions of Eu^{3+} compounds are listed in **Table 9**.

Table 9. Transitions observed in absorption spectra of Eu^{3+} compounds.[225]

Transition	Dipole Character[A]	Wavelength (nm)
$^7F_0 \rightarrow {}^7F_6$	ED	1850 - 2200
$^7F_1 \rightarrow {}^5D_0$	MD	585 - 600
$^7F_0 \rightarrow {}^5D_0$	ED	570 - 585
$^7F_1 \rightarrow {}^5D_1$	ED	530 - 540
$^7F_0 \rightarrow {}^5D_1$	MD	520 - 530
$^7F_1 \rightarrow {}^5D_2$	ED	470 - 480
$^7F_0 \rightarrow {}^5D_2$	ED	460 - 470
$^7F_1 \rightarrow {}^5D_3$	ED	410 - 420
$^7F_1 \rightarrow {}^5L_6$	ED	400 - 410
$^7F_0 \rightarrow {}^5L_6$	ED	390 - 405

$^7F_1 \rightarrow {}^5D_4$	ED	365 - 370
$^7F_0 \rightarrow {}^5D_4$	ED	355 - 365

A ED – electric dipole transition, MD – magnetic dipole transition.

The lower wavelength Eu^{3+} absorption and MCD spectra are shown in **Figure 69**. The $^7F_0 \rightarrow {}^5L_6$ transition at 394 nm is the most intense in the absorption. In MCD, it provides a strong (+/–) couplet with $g = 2.5\times10^{-2}$. Between 372 and 390 nm, several low intensity bands corresponding to the transitions from the $^7F_0$ level to several *J*-levels of ^5L_J (J = 7, 8 and 9) can be observed.[357] At 361.5 nm, a $^7F_0 \rightarrow {}^5D_4$ transition can be observed. The region below 330 nm is very rich in transitions ($^7F_0 \rightarrow {}^5F$ and ^5I levels)[225] and their assignment is complicated. The most intense band in this region at 317.5 nm corresponding to the $^7F_0 \rightarrow {}^5H_3$ transition[357] is accompanied by a (+/–) couplet in MCD with $g = 2.6\times10^{-2}$.

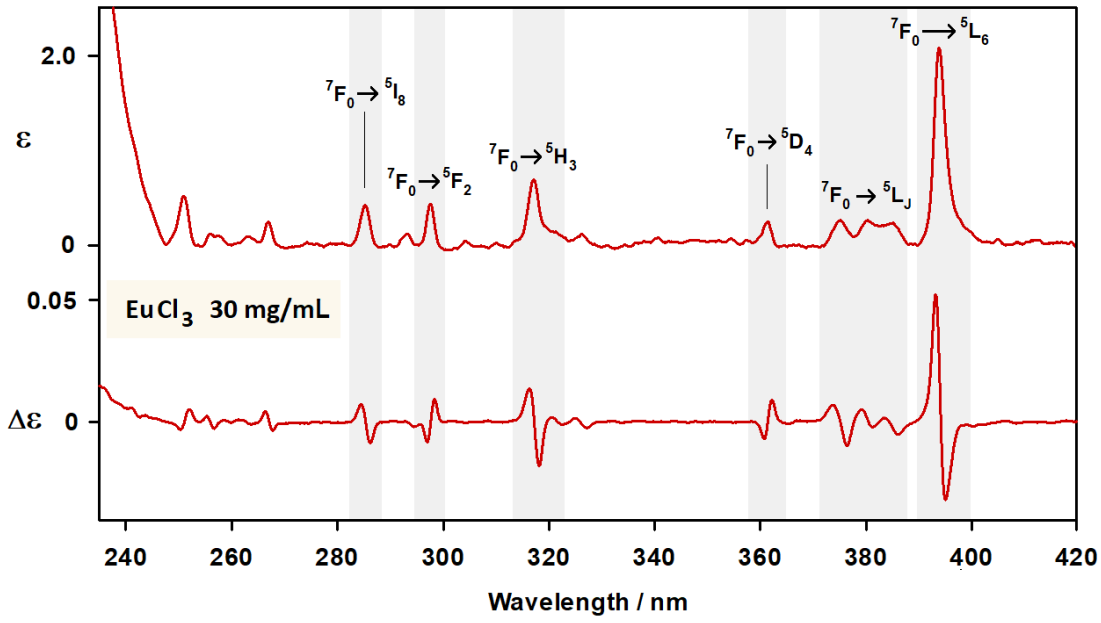

Figure 69. Experimental UV-Vis absorption and MCD spectra of $EuCl_3$ (concentration 30 mg/mL, B = 1.5 T) between 235 and 420 nm. The bands were assigned according to the literature.[225, 357]

At higher wavelengths (**Figure 70**), only 3 electronic transitions yield MCD bands of considerable intensity. A peak at 526 nm corresponding to the magnetic dipole transition $^7F_0 \rightarrow {}^5D_1$ is used to estimate the strength of crystal field surrounding the Eu^{3+} ion. In strong crystal fields it is split into two bands, while in crystal fields of low intensity such as water solvent, only one band is observed. It is accompanied with a (+/–) couplet in MCD with $g = 2.8\times10^{-2}$. The similar behavior can be observed also for the electric dipole $^7F_1 \rightarrow {}^5D_1$ transition located at 535 nm.[358] The $^7F_0 \rightarrow {}^5D_0$ transition located between 570 – 585 nm is sensitive to the number of coordinated species to the Eu^{3+} ion. If 8-coordinate and 9-coordinate species are comparably represented in the solution, two distinct peaks can be observed.[225] We do not observe this transition in our spectra probably because of conformer averaging. A broad band at 592.5 nm corresponding to the $^7F_1 \rightarrow {}^5D_0$ transition is accompanied by a (+/–) couplet in MCD. The last absorption band with considerable MCD intensity in this region is located at 464.5 nm and belongs to the $^7F_0 \rightarrow {}^5D_2$ transition. The *g*-factor is somewhat lower ($g = 1.1\times10^{-2}$).

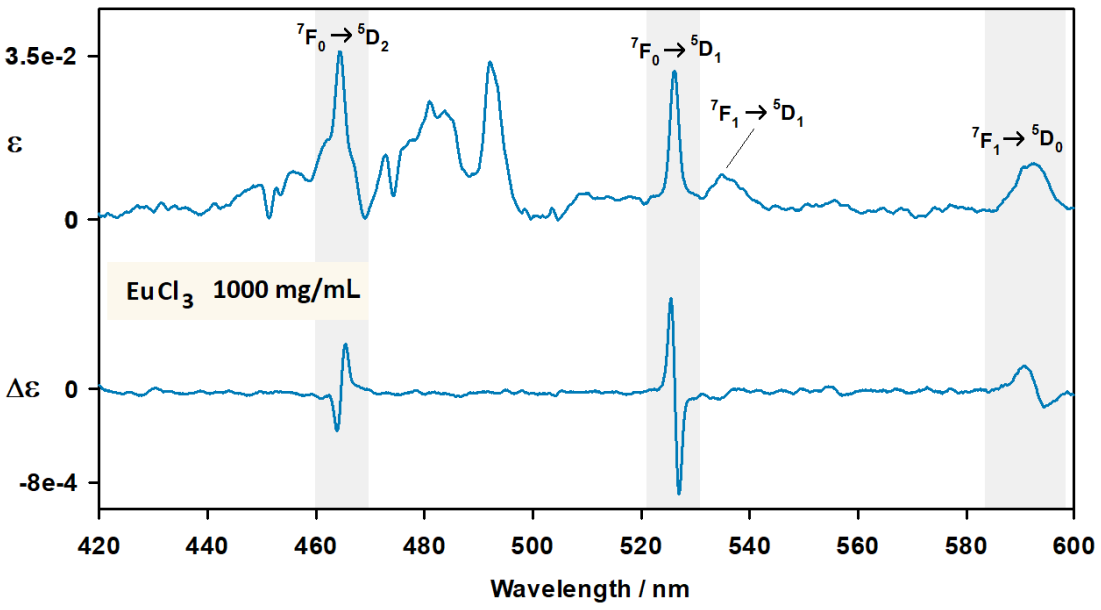

Figure 70. Experimental UV-Vis absorption and MCD spectra of $EuCl_3$ (concentration 1000 mg/mL, B = 1.5 T) between 420 and 600 nm. The spectra were interpreted according to the literature.[225]

Within the CFT model, the water ligands perturb the europium *f*-states and lead to non-zero electric absorption and MCD intensities. For simplicity, only the electrostatic perturbation was considered, and the spectra are simulated for 0 K. The way we account for the charge distribution around the Eu^{3+} ion in CFT calculations has a remarkable effect on the calculated spectra. The comparison of absorption and MCD spectra for two models (point charges vs. charge density) is plotted in **Figure 71**. While the absorption spectra show only minor changes, the MCD spectra provide different patterns and sometimes even opposite signs for the two methods.

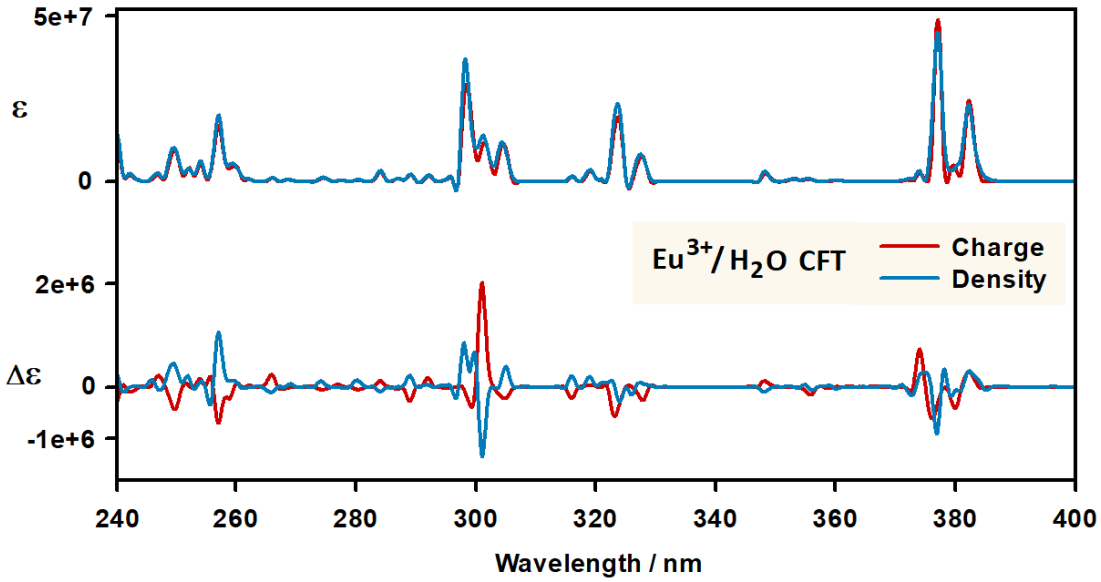

Figure 71. UV-Vis absorption and MCD spectra of Eu^{3+}/H_2O calculated by CFT model using two descriptions of charge around the metal ion: partial atomic charges, or charge density. The average of 3000 snapshots is reported, peak half-width at half-maximum (HWHM) was set to 100 cm^{-1}.

Because the clusters of Eu^{3+}/H_2O do not have a particular rigid structure or symmetry, a relatively high number of them needs to be averaged for a converged spectral pattern. In **Figure 72**, the convergence is shown as a deviation (RMSD) relative to the average of 3000 spectra. For point charges, the MCD spectra converge much faster than for charge density. Also, the absorption curves converge much faster than MCD curves; the higher sensitivity of the MCD intensities to small changes in the system geometry is in agreement with previous studies.[156, 159, 359, 360] Therefore,

while only about a hundred clusters are needed to simulate the main absorption features, several hundreds (point charges) or even thousands (charge density) are needed to obtain a reliable MCD spectral patterns according to this model.

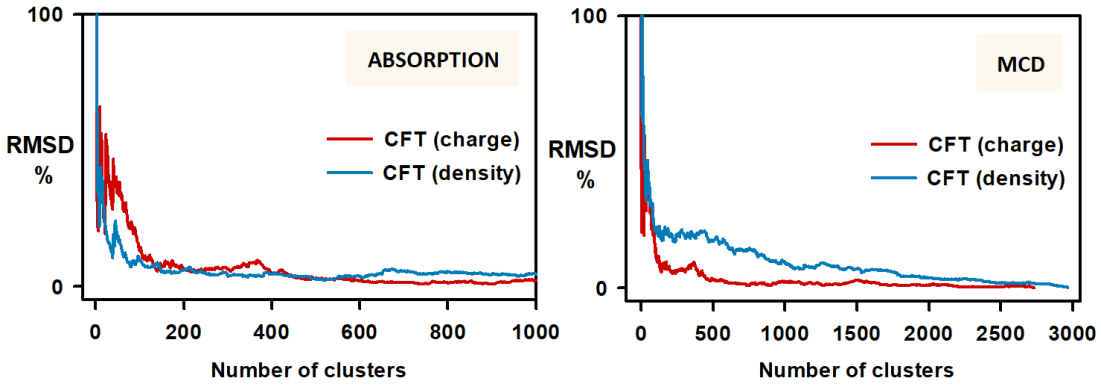

Figure 72. Dependence of the RMSD on the number of averaged absorption (left) and MCD (right) cluster spectra of hydrated Eu^{3+} ion calculated by CFT model.

We compare the spectra calculated by the CFT and MS-CASPT2 methods with the experimental ones in **Figures 73** (absorption) and **74** (MCD). For CFT, we show the spectra calculated using the partial atomic charges. This approach provides transition energies very close to the experimental values, and it reasonably well reproduces the relative absorption intensities below 420 nm. In the region above 420 nm, the intensities of $^7F_0 \rightarrow {}^5D_2$ and $^7F_1 \rightarrow {}^5D_2$ (464.5 and 473 nm in experiment vs. 461 and 470 nm in CFT calculation) are significantly underestimated. For MCD, the simple model seems not to be able to reproduce the experimental sign patterns, except for very rough trends. We attribute this mainly to the simplicity of the crystal field approach, for which an additional tuning of parameters would be required in order to reproduce the MCD spectra.

The MS-CASPT2 method provides qualitatively better absorption and MCD intensities. Especially the absorption bands are in a good agreement with experiment, while in case of MCD, the intensities of $^7F_0 \rightarrow {}^5L_6$ and $^7F_0 \rightarrow {}^5D_1$ transitions (394 and 526 nm in experiment vs. 351 and 448 nm in MS-CASPT2 calculation) are significantly underestimated. Also, a significant but consistent shift of calculated MS-CASPT2 transition energies is apparent and the simulated spectra need to be “scaled”

to compare corresponding peaks. The MS-CASPT2 method provides the correct signs for all of the most intense MCD transitions with the exception of the $^7F_0 \rightarrow {}^5D_2$ transition.

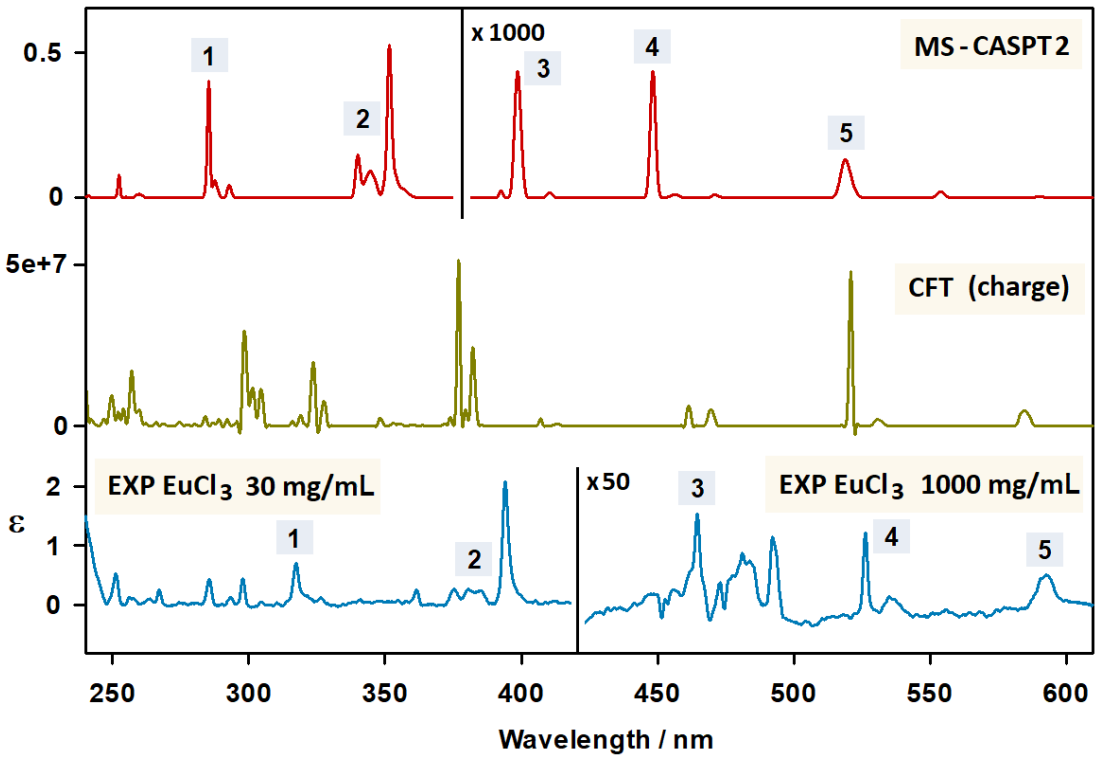

Figure 73. Experimental (bottom, B = 1.5 T) and simulated UV-Vis absorption spectra of hydrated Eu^{3+} ion. For MS-CASPT2 calculation (top), the average of 10 snapshots is reported; B = 1.5 T, T = 293.15 K, peak HWHM was set to 100 cm^{-1}. For CFT (middle), partial atomic charges were used to model the charge distribution around the Eu^{3+} ion; the average of 3000 snapshots is reported, peak HWHM was set to 100 cm^{-1}. The numbers in blue boxes mark the positions of corresponding peaks in experiment and calculation.

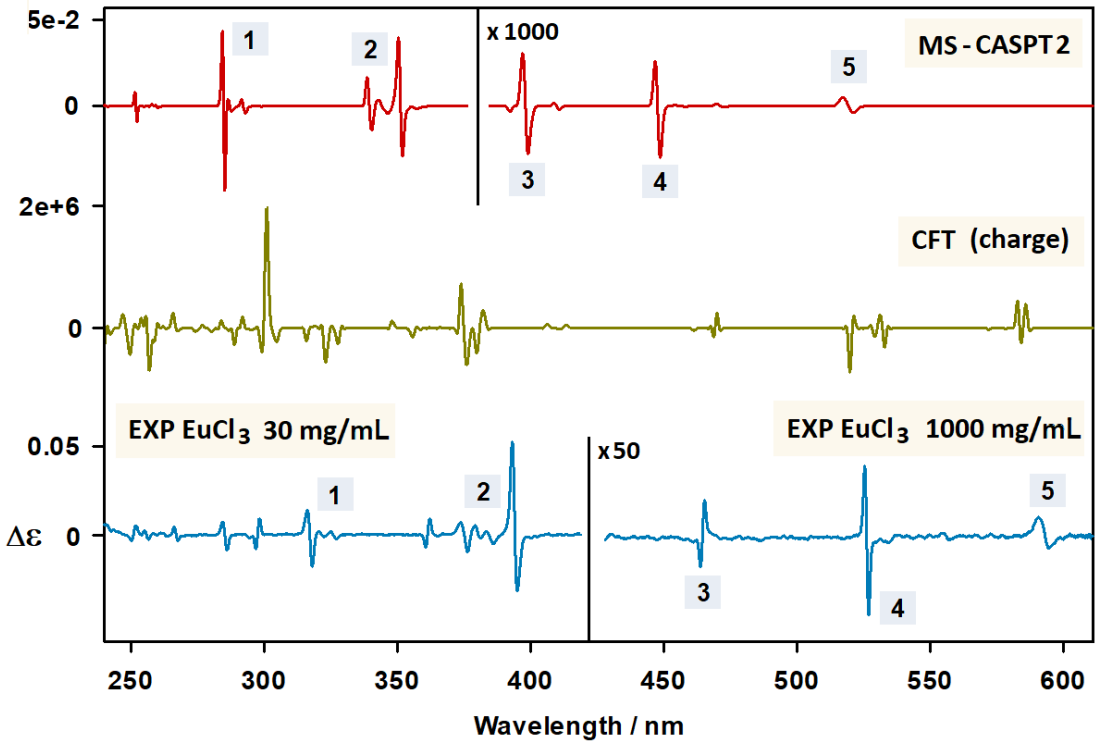

Figure 74. Experimental (bottom, B = 1.5 T) and simulated MCD spectra of hydrated Eu^{3+} ion. For MS-CASPT2 calculation (top), the average of 10 snapshots is reported; B = 1.5 T, T = 293.15 K, peak HWHM was set to 100 cm^{-1}. For CFT (middle), partial atomic charges were used to model the charge distribution around the Eu^{3+} ion; the average of 3000 snapshots is reported, peak HWHM was set to 100 cm^{-1}. The numbers in blue boxes mark the positions of corresponding peaks in experiment and calculation.

4.2.3. MCD Spectra of Ce^{3+}, Pr^{3+}, Nd^{3+} and Gd^{3+}

In **Figure 75**, the spectra for Ce^{3+}/H_2O are shown. In the experimental absorption spectra, we observe several transitions at 212, 222, 239 and 253 nm corresponding to the excitation of a *4f* electron into the *5d* shell ($^2F_{5/2}$ and $^2F_{7/2} \rightarrow$ $^2D_{3/2}$ and $^2D_{5/2}$). The *4f* → *5d* transitions are dipole allowed and generally broad. Their energy largely depends on the chemical environment around the Ln^{3+} ion because the *5d* orbitals are external and therefore can directly interact with the ligand orbitals.[129] Our CFT method does not involve *f* → *d* transitions, therefore we do not show it. In case of MS-CASPT2 method, the calculated energies were correctly attributed to the $^2F \rightarrow {}^2D$ transitions.

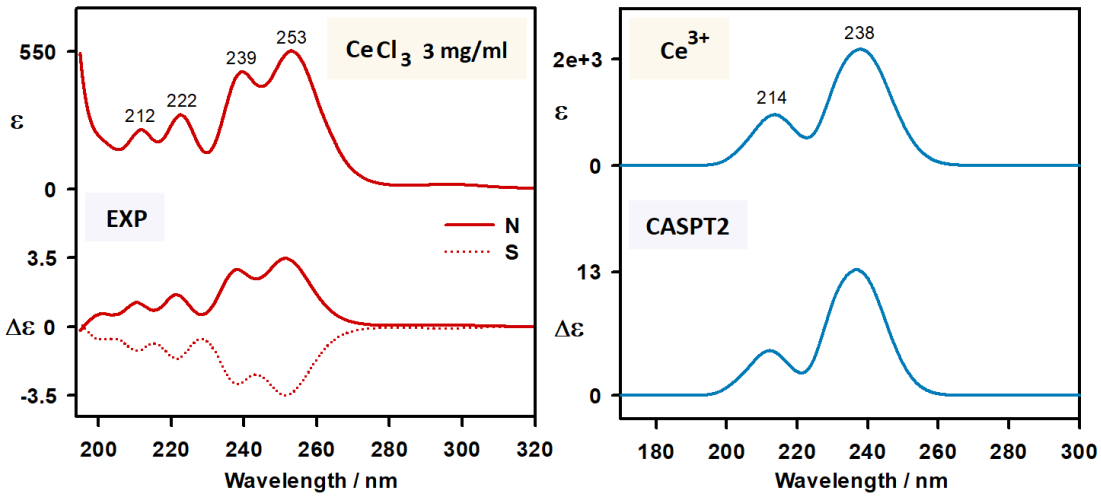

Figure 75. UV-Vis absorption and MCD spectra of hydrated Ce^{3+} ion. The experimental spectrum (left) was measured in two orientations of the magnet; the calculated spectrum was simulated by a MS-CASPT2 method (average of 10 snapshots, B = 1.50 T, T = 293.15 K, peak HWHM was set to 2000 cm^{-1}).

For aqueous Pr^{3+} ion, the CFT calculations reproduce transition energies very well, but similarly as for Eu^{3+} ion it fails to reproduce the relative intensities and MCD signs (**Figure 76**). MS-CASPT2 calculation energies are again significantly shifted to lower wavelengths when compared with the experiment. However, both the relative intensities and the MCD signs are reproduced very nicely. The most intense band in UV-Vis absorption spectrum can be attributed to the $^3H_4 \rightarrow {}^3P_2$ transition[361] (444 nm) with an intense (+/–) couplet in MCD with $g = 1.5\times10^{-2}$. Other bands between 450 and 500 nm originate in the transitions from $^3H_4$ ground state to various *J*-levels of ^3P and ^1I excited states. At 591 nm, a broad and relatively weak $^3H_4 \rightarrow {}^1D_2$ transition accompanied by a broad (+/–) couplet ($g = 1\times10^{-2}$) is observed. Our interpretation of Pr^{3+} spectra by MS-CASPT2 method is in agreement with the literature.[361]

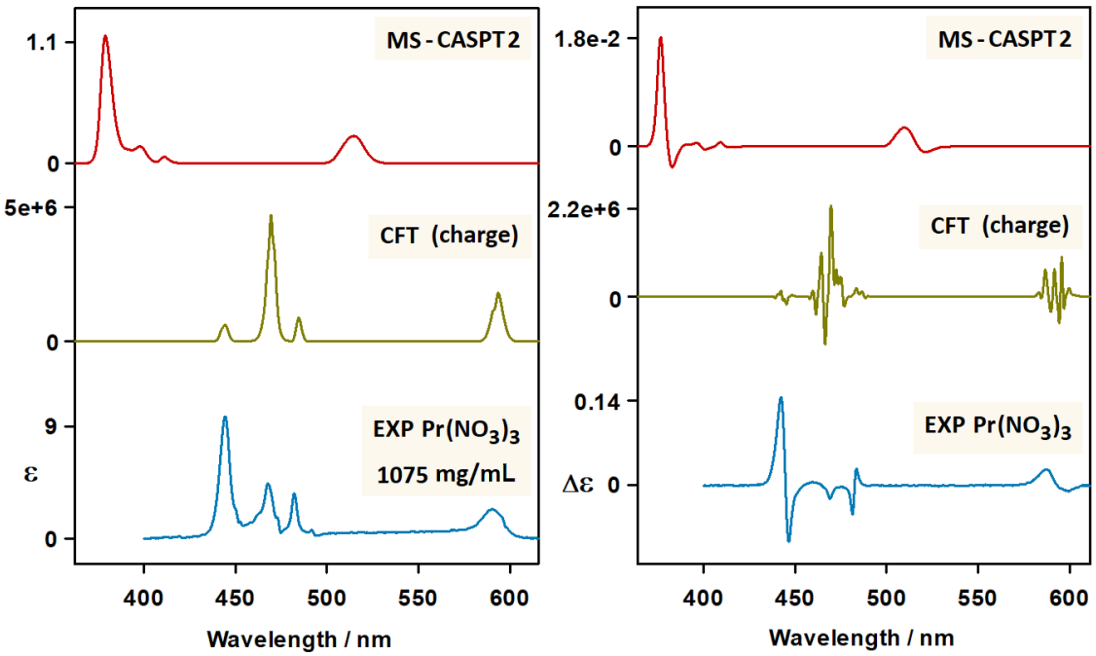

Figure 76. Experimental (bottom, B = 1.5 T) and simulated absorption (left) and MCD (right) spectra of hydrated Pr^{3+} ion. For MS-CASPT2 calculation (top), the average of 10 snapshots is reported; B = 1.5 T, T = 293.15 K, peak HWHM was set to 250 cm^{-1}. For CFT (middle), point charges were used to model the charge distribution around the Pr^{3+} ion; the average of 3000 snapshots is reported, peak HWHM was set to 100 cm^{-1}.

The Nd^{3+} UV-Vis absorption and MCD spectra are very complex and rich in transitions (**Figure 77**). The experiment is consistent with the spectra published.[362, 363] The observed bands correspond to the superposition of several different transitions. Similarly as for other Ln^{3+} ions, the CFT method reproduces the energies but not the relative intensities and MCD signs. In this case, also the MS-CASPT2 method was not too successful in modeling the absorption and MCD bands. The transitions in absorption spectra of aqueous Nd^{3+} ion originate in the $^4I_{9/2}$ ground state. The most intense band under 600 nm corresponds to a combination of $^4I_{9/2} \rightarrow {}^2G_{7/2}$ and $^4I_{9/2} \rightarrow {}^4G_{5/2}$ transitions (575 nm). Between 550 and 400 nm, transitions from the ground state to various *J*-levels of ^4G, ^2G, ^2K, ^2D and ^2P states are responsible for a complex structure of the spectra. Around 350 nm, we observe transitions to ^4D, ^2I and ^2L excited states. In higher wavelengths region, two absorption bands originate from $^4I_{9/2} \rightarrow {}^4S_{3/2}$ / $^4F_{7/2}$ (741 nm) and $^4I_{9/2} \rightarrow {}^4F_{5/2}$ / $^2H_{9/2}$ transitions (796 nm).

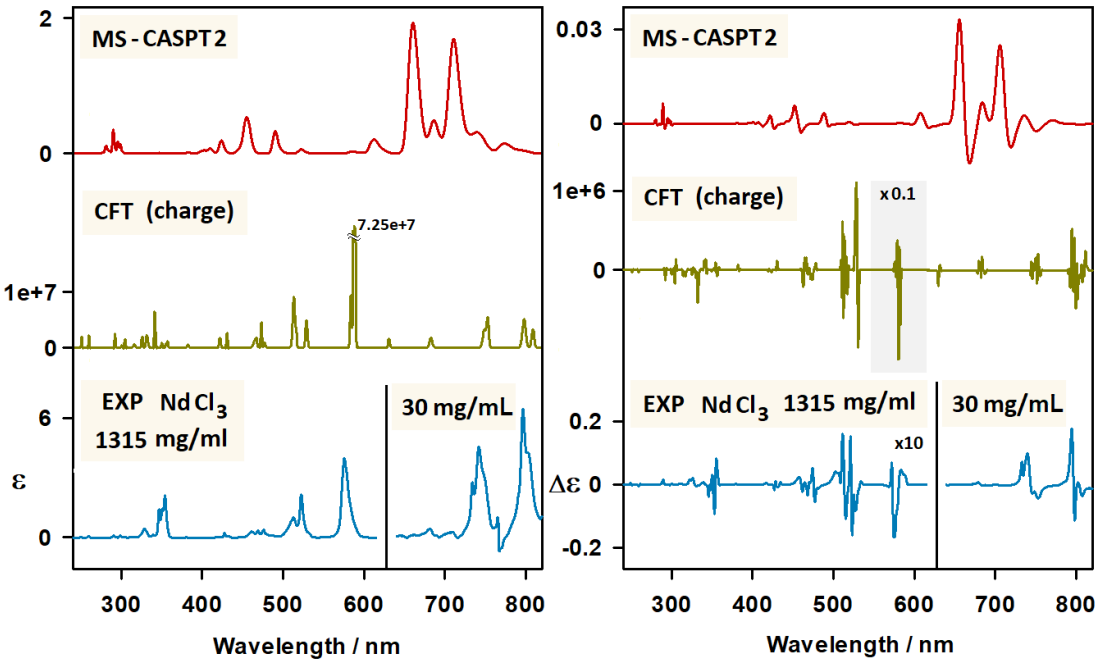

Figure 77. Experimental (bottom, B = 1.5 T) and simulated absorption (left) and MCD (right) spectra of hydrated Nd^{3+} ion. For MS-CASPT2 calculation (top), the average of 10 snapshots is reported; B = 1.5 T, T = 293.15 K, peak HWHM was set to 180 cm^{-1}. For CFT (middle), partial atomic charges were used to model the charge distribution around the Nd^{3+} ion; the average of 3000 snapshots is reported, peak HWHM was set to 100 cm^{-1}.

UV-Vis absorption and MCD spectra of Gd^{3+}/H_2O are very simple (**Figure 78**) due to relatively high energies of transitions and limited instrumental range. In experimental spectrum at ~275 nm we observe a group of transitions from the ground state $^8S_{7/2}$ to various *J*-levels of the ^6I excited state.[364] Besides the energy shift of MS-CASPT2 spectra, it provides a qualitatively very good agreement with the experiment. In this case, the CFT method failed to reproduce the energies of Gd^{3+} transitions.

We conclude that the parametric CFT method provides reasonable estimates of energies for the $f \rightarrow f$ transitions, but it fails to reproduce the MCD signs and intensities. Moreover, it provided very different spectra for each MD snapshot. For MS-CASPT2 calculations, even few clusters provided reasonable agreement with the experiment. MS-CASPT2 in most cases also predicted correct relative intensities of the experimental bands. MS-CASPT2 energies were usually too high (band wavelength too low) when compared to the experiment. Another practical problem of MS-CASPT2 method lies in the correct selection of active orbitals for the CASSCF,

since this choice can have a remarkable effect on the final results. In the future, this method has the potential to provide reliable simulations of absorption and MCD spectra for open-shell systems with reasonable computational costs.

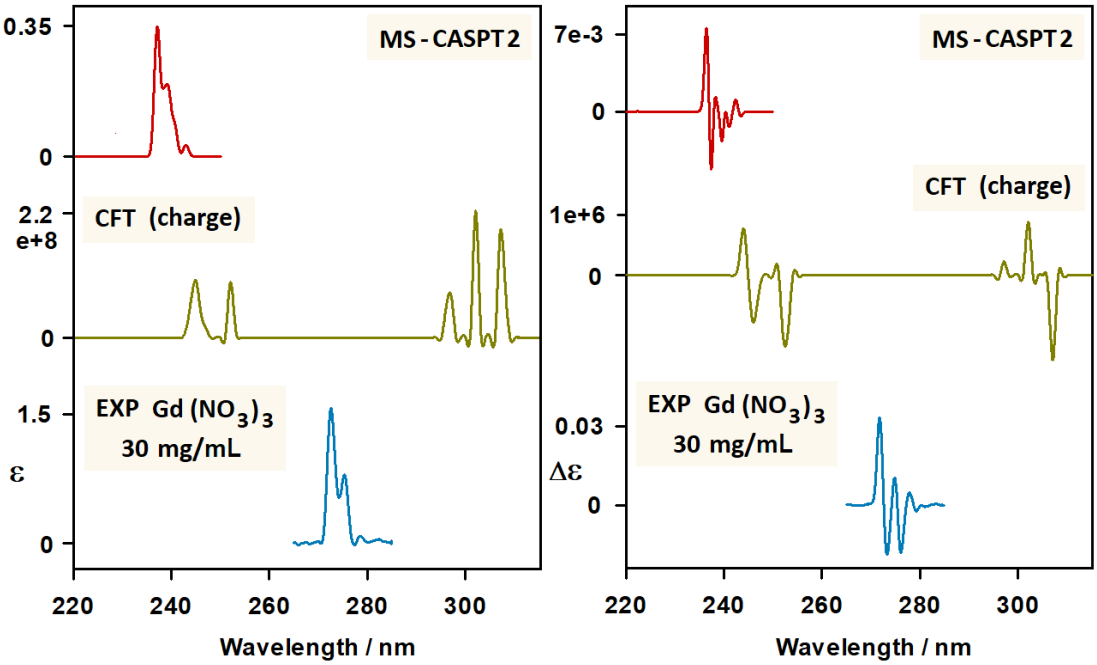

Figure 78. Experimental (bottom, B = 1.5 T) and simulated absorption (left) and MCD (right) spectra of hydrated Gd^{3+} ion. For MS-CASPT2 calculation (top), the average of 10 snapshots is reported; B = 1.5 T, T = 293.15 K, peak HWHM was set to 180 cm^{-1}. For CFT (middle), partial atomic charges were used to model the charge distribution around the Gd^{3+} ion; the average of 3000 snapshots is reported, peak HWHM was set to 100 cm^{-1}.

Conclusions

In this thesis, we described three projects exploring molecular chirality. In Chapter 2, we showed that vibrational circular dichroism and circularly polarized luminescence spectroscopies are advantageous in structural studies of various amyloid fibrils. Solid-state VCD and its application to the crystals of nucleosides was discussed in Chapter 3. Chapter 4 was dedicated to the magnetic circular dichroism of hydrated Ln^{3+} ions. The main results can be summarized as follows:

I. We optimized preparation protocols for formation of amyloid fibrils from several proteins: hen egg-white lysozyme, polyglutamic acids, and insulin. We also optimized the vibrational circular dichroism and circularly polarized luminescence measurements.

II. Vibrational circular dichroism spectra of amyloid fibrils in the amide I region were up to two orders of magnitude larger than for usual protein VCD. Using the combined DFT/TDC simulations, we linked this enhancement to the length and twist of the fibrils.

III. We prepared polymorphic fibrils by seeding the protein solutions with preformed fibrils of the same or other protein. We found that the shape of the VCD is sensitive to different fibril polymorphs. We identified a "sergeant-and-soldiers" mechanism in fibril formation due to the heterogeneous seeding, where the chirality of the minor component (i.e. seeds) determined the chirality of the whole aggregate.

IV. We developed a method of measuring circularly polarized luminescence of Eu^{3+} ion or complex with the fibrils in Raman optical activity experiment. While VCD is sensitive to the long-range structure of fibrils, CPL senses the local structure. By this method, we were able to track the growth of polyglutamic acid amyloid fibrils.

V. VCD spectroscopy was used to study the crystalline suspensions of nucleosides. We measured strong VCD spectra (*g*-factor up to 8×10^{-2}), but crystalline VCD

was very prone to artifacts; they were more common for larger adenosine crystals and less common for smaller guanosine crystals (size ~120 μm and ~10 μm, respectively).

VI. We studied hydration polymorphism of guanosine crystals. Guanosine exists as a dihydrate at relative humidity above 20 %. The dihydrate and anhydrous forms provided distinct VCD spectra. Reliable spectra can be measured in a very short time (15 min for 20 mg/mL guanosine). We find the possibility to study hydration of the crystals by VCD quite interesting.

VII. A combination of molecular dynamics simulations with parametric crystal field theory or multistate CASPT2 method was used to interpret the Ln^{3+} MCD spectra. MD simulations were used to model the solvation. Larger ions such as Ce^{3+}, Pr^{3+} and Nd^{3+} have usually 10 H_2O molecules in the first hydration shell. Other Ln^{3+} ions prefer configurations with 9 water molecules.

VIII. CFT provided reasonable transition energies, but failed to reproduce the experimental MCD intensities. A high number of Ln^{3+}/H_2O clusters had to be averaged for a converged spectral pattern.

IX. Transition energies calculated by the MS-CASPT2 method were too big, but the MCD spectral patterns were more reasonable. Moreover, the spectra were not so dependent on the configuration of waters around the Ln^{3+} ions, therefore fewer clusters needed to be averaged.

In summary, we showed that chiroptical spectroscopic methods are useful for structural studies of chiral molecules and supramolecular aggregates. Depending on the choice of spectroscopic technique, various aspects of the molecular structure could be studied. A combination of experimental and theoretical approaches was very advantageous for interpretation of the spectra and deeper understanding of structure and intramolecular interactions.

Bibliography

[1] F. Arago *Mém. Inst.* **1811**, 1, 93-134.

[2] J. W. F. Herschel *Trans. Cambridge Philos. Soc.* **1822**, 1, 43-52.

[3] L. Pasteur *C. R. Acad. Sci. Paris*. **1848**, 26, 535-539.

[4] A. Guijarro, M. Yus *The Origin of Chirality in the Molecules of Life: A Revision from Awareness to the Current Theories and Perspectives of this Unsolved Problem*, Royal Society of Chemistry, UK, London, **2009**.

[5] G. F. Joyce, G. M. Visser, C. A. A. Vanboeckel, J. H. Vanboom, L. E. Orgel, J. Vanwestrenen *Nature* **1984**, 310, 602-604.

[6] D. G. Blackmond *Cold Spring Harb. Perspect. Biol.* **2019**, 11.

[7] K. Soai, T. Shibata, H. Morioka, K. Choji *Nature* **1995**, 378, 767-768.

[8] N. A. Hawbaker, D. G. Blackmond *Nat. Chem.* **2019**, 11, 957-962.

[9] J. Fišer *Úvod do molekulové symetrie: aplikace teorie grup v chemii*, Státní nakladatelství technické literatury, Praha, **1980**.

[10] J. McMurry *Organic Chemistry 8th Edition*, Brooks/Cole, Cengage Learning, USA, **2011**.

[11] B. W. Pfennig *Principles of Inorganic Chemistry*, John Wiley & Sons, Inc., New Jersey, USA, **2015**.

[12] E. Hecht *Optics 5th Global Edition*, Pearson Education Limited, UK, **2017**.

[13] L. D. Barron, A. D. Buckingham *Chem. Phys. Lett.* **2010**, 492, 199-213.

[14] E. B. Bauer *Chem. Soc. Rev.* **2012**, 41, 3153-3167.

[15] C. W. Y. Chung, P. H. Toy *Tetrahedron Asymmetry* **2004**, 15, 387-399.

[16] E. N. Jacobsen *Acc. Chem. Res.* **2000**, 33, 421-431.

[17] R. Noyori, T. Ohkuma *Angew. Chem. Int. Ed.* **2001**, 40, 40-73.

[18] D. S. Bradshaw, J. M. Leeder, M. M. Coles, D. L. Andrews *Chem. Phys. Lett.* **2015**, 626, 106-110.

[19] J. W. Hubbard, D. Ganes, H. K. Lim, K. K. Midha *Clin. Biochem.* **1986**, 19, 107-112.

[20] E. L. Izake *J. Pharm. Sci.* **2007**, 96, 1659-1676.

[21] M. Krupová, J. Kessler, P. Bouř *ChemPlusChem* **2020**, 85, 561-575.

[22] G. Holzwarth, E. C. Hsu, H. S. Mosher, T. R. Faulkner, A. Moscowitz *J. Am. Chem. Soc.* **1974**, 96, 251-252.

[23] L. D. Barron, M. P. Bogaard, A. D. Buckingham *J. Am. Chem. Soc.* **1973**, 95, 603-605.

[24] W. Hug, G. Hangartner *J. Raman Spectrosc.* **1999**, 30, 841-852.

[25] T. R. Devine, T. A. Keiderling *J. Phys. Chem.* **1984**, 88, 390-394.

[26] T. A. Keiderling, P. Bouř *Phys. Rev. Lett.* **2018**, 121.

[27] L. D. Barron, J. Vrbancich *J. Raman Spect.* **1983**, 14, 118-125.

[28] L. D. Barron *Molecular light scattering and optical activity*, Cambridge University Press, UK, **2009**.

[29] N. Berova, L. Di Bari, G. Pescitelli *Chem. Soc. Rev.* **2007**, 36, 914-931.

[30] N. Berova, K. Nakanishi, R. W. Woody *Circular Dichroism: Principles and Applications, 2nd Edition*, Wiley-VCH, Germany, **2000**.

[31] V. I. Dodero, Z. B. Quirolo, M. A. Sequeira *Front. Biosc.* **2011**, 16, 61-73.

[32] N. J. Greenfield *Nat. Prot.* **2006**, 1, 2876-2890.

[33] S. M. Kelly, T. J. Jess, N. C. Price *Biochim. Biophys. Acta Proteins* **2005**, 1751, 119-139.

[34] A. J. Miles, B. A. Wallace *Protein Sci.* **2018**, 27, 1717-1722.

[35] L. Whitmore, B. A. Wallace *Nucleic Acids Res.* **2004**, 32, 668-673.

[36] C. Wiedemann, P. Bellstedt, M. Gorlach *Bioinformatics* **2013**, 29, 1750-1757.

[37] P. J. Stephens, F. J. Devlin, J. J. Pan *Chirality* **2008**, 20, 643-663.

[38] G. Magyarfalvi, G. Tarczay, E. Vass *Wiley Interdiscip. Rev. Comput. Mol. Sci.* **2011**, 1, 403-425.

[39] C. W. Deutsche, A. Moscowitz *J. Chem. Phys.* **1968**, 49, 3257-3272.

[40] C. W. Deutsche, A. Moscowitz *J. Chem. Phys.* **1970**, 53, 2630-2644.

[41] G. Holzwarth, I. Chabay *J. Chem. Phys.* **1972**, 57, 1632-1635.

[42] L. A. Nafie, T. B. Freedman *Chem. Phys. Lett.* **1987**, 134, 225-232.

[43] P. J. Stephens *J. Phys. Chem.* **1985**, 89, 748-752.

[44] G. Holzwart, E. C. Hsu, H. S. Mosher, T. R. Faulkner, A. Moscowitz *J. Am. Chem. Soc.* **1974**, 96, 251-252.

[45] E. C. Hsu, Holzwart.G *J. Chem. Phys.* **1973**, 59, 4678-4685.

[46] L. A. Nafie, J. C. Cheng, P. J. Stephens *J. Am. Chem. Soc.* **1975**, 97, 3842-3843.

[47] L. A. Nafie, M. Diem *Acc. Chem. Res.* **1979**, 12, 296-302.

[48] R. D. Singh, T. A. Keiderling *Biopolymers* **1981**, 20, 237-240.
[49] A. C. Sen, T. A. Keiderling *Biopolymers* **1984**, 23, 1519-1532.
[50] A. C. Sen, T. A. Keiderling *Biopolymers* **1984**, 23, 1533-1545.
[51] B. B. Lal, L. A. Nafie *Biopolymers* **1982**, 21, 2161-2183.
[52] P. Pančoška, S. C. Yasui, T. A. Keiderling *Biochemistry* **1989**, 28, 5917-5923.
[53] P. Pančoška, S. C. Yasui, T. A. Keiderling *Biochemistry* **1991**, 30, 5089-5103.
[54] R. K. Dukor, T. A. Keiderling *Biopolymers* **1991**, 31, 1747-1761.
[55] V. P. Gupta, T. A. Keiderling *Biopolymers* **1992**, 32, 239-248.
[56] A. Annamalai, T. A. Keiderling *J. Am. Chem. Soc.* **1987**, 109, 3125-3132.
[57] M. Gulotta, D. J. Goss, M. Diem *Biopolymers* **1989**, 28, 2047-2058.
[58] W. X. Zhong, M. Gulotta, D. J. Goss, M. Diem *Biochemistry* **1990**, 29, 7485-7491.
[59] L. Wang, T. A. Keiderling *Biochemistry* **1992**, 31, 10265-10271.
[60] L. Yang, T. A. Keiderling *Biopolymers* **1993**, 33, 315-327.
[61] L. Wang, L. Yang, T. A. Keiderling *Biophys. J.* **1994**, 67, 2460-2467.
[62] V. Andrushchenko, D. Tsankov, M. Krasteva, H. Wieser, P. Bouř *J. Am. Chem. Soc.* **2011**, 133, 15055-15064.
[63] V. Andrushchenko, Z. Leonenko, D. Cramb, H. van de Sande, H. Wieser *Biopolymers* **2001**, 61, 243-260.
[64] D. Kurouski *Anal. Chim. Acta* **2017**, 990, 54-66.
[65] T. A. Keiderling *Molecules* **2018**, 23.
[66] P. L. Polavarapu, C. X. Zhao *Fresen J. Anal. Chem*. **2000**, 366, 727-734.
[67] F. Devlin, P. J. Stephens *Appl. Spectrosc.* **1987**, 41, 1142-1144.
[68] A. Lakhani, P. Maloň, T. A. Keiderling *Appl. Spectrosc.* **2009**, 63, 775-785.
[69] P. Xie, M. Diem *Appl. Spectrosc.* **1996**, 50, 675-680.
[70] L. A. Nafie, H. Buijs, A. Rilling, X. L. Cao, R. K. Dukor *Appl. Spectrosc.* **2004**, 58, 647-654.
[71] Y. A. He, B. Wang, R. K. Dukor, L. A. Nafie *Appl. Spectrosc.* **2011**, 65, 699-723.
[72] U. Narayanan, T. A. Keiderling *J. Am. Chem. Soc.* **1983**, 105, 6406-6411.
[73] T. Xiang, D. J. Goss, M. Diem *Biophys. J.* **1993**, 65, 1255-1261.
[74] P. J. Stephens *J. Phys. Chem.* **1985**, 89, 748-752.

[75] F. J. Devlin, P. J. Stephens, C. F. Osterle, K. B. Wiberg, J. R. Cheeseman, M. J. Frisch *J. Org. Chem.* **2002**, 67, 8090-8096.
[76] G. te Velde, F. M. Bickelhaupt, E. J. Baerends, C. Fonseca Guerra, S. J. A. van Gisbergen, J. G. Snijders, T. Ziegler *J. Comput Chem*. **2001**, 22, 931-967.
[77] K. Aidas, C. Angeli, K. L. Bak, V. Bakken, R. Bast, L. Boman, O. Christiansen, R. Cimiraglia, S. Coriani, P. Dahle, E. K. Dalskov, U. Ekström, T. Enevoldsen, J. J. Eriksen, P. Ettenhuber, B. Fernández, L. Ferrighi, H. Fliegl, L. Frediani, K. Hald, A. Halkier, C. Hättig, H. Heiberg, T. Helgaker, A. C. Hennum, H. Hettema, E. Hjertenæs, S. Høst, I. M. Høyvik, M. F. Iozzi, B. Jansík, H. J. A. Jensen, D. Jonsson, P. Jørgensen, J. Kauczor, S. Kirpekar, T. Kjærgaard, W. Klopper, S. Knecht, R. Kobayashi, H. Koch, J. Kongsted, A. Krapp, K. Kristensen, A. Ligabue, O. B. Lutnæs, J. I. Melo, K. V. Mikkelsen, R. H. Myhre, C. Neiss, C. B. Nielsen, P. Norman, J. Olsen, J. M. H. Olsen, A. Osted, M. J. Packer, F. Pawlowski, T. B. Pedersen, P. F. Provasi, S. Reine, Z. Rinkevicius, T. A. Ruden, K. Ruud, V. V. Rybkin, P. Sałek, C. C. M. Samson, A. S. de Merás, T. Saue, S. P. A. Sauer, B. Schimmelpfennig, K. Sneskov, A. H. Steindal, K. O. Sylvester-Hvid, P. R. Taylor, A. M. Teale, E. I. Tellgren, D. P. Tew, A. J. Thorvaldsen, L. Thøgersen, O. Vahtras, M. A. Watson, D. J. D. Wilson, M. Ziolkowski, H. Ågren *Wires. Comput. Mol. Sci.* **2014**, 4, 269-284.
[78] A. Polyanichko, V. Andrushchenko, P. Bouř, H. Wieser *Vibrational Circular Dichroism Studies of Biological Macromolecules and their Complexes* in *Circular Dichroism: Theory and Spectroscopy*. Nova Science Publishers, New York, **2012**.
[79] T. B. Freedman, X. Cao, R. K. Dukor, L. A. Nafie *Chirality* **2003**, 15, 743-758.
[80] E. Burgueno-Tapia, P. Joseph-Nathan *Nat. Prod. Commun.* **2015**, 10, 1785-1795.
[81] S. Abbate, L. F. Burgi, E. Castiglioni, F. Lebon, G. Longhi, E. Toscano, S. Caccamese *Chirality* **2009**, 21, 436-441.
[82] P. Bouř, J. Sopková, L. Bednárová, P. Maloň, T. A. Keiderling *J. Comput Chem*. **1997**, 18, 646-659.
[83] N. S. Bieler, M. P. Haag, C. R. Jacob, M. Reiher *J. Chem. Theory Comput.* **2011**, 7, 1867-1881.
[84] S. Yamamoto, X. J. Li, K. Ruud, P. Bouř *J. Chem. Theory Comput.* **2012**, 8, 977-985.

[85] K. V. J. Jose, D. Beckett, K. Raghavachari *J. Chem. Theory Comput.* **2015**, 11, 4238-4247.

[86] K. V. J. Jose, K. Raghavachari *Chirality* **2016**, 28, 755-768.

[87] B. Thapa, D. Beckett, K. V. J. Jose, K. Raghavachari *J. Chem. Theory Comput.* **2018**, 14, 1383-1394.

[88] J. R. Aviles-Moreno, E. U. Horno, F. P. Urena, J. J. L. Gonzalez *Spectrochim. Acta A* **2011**, 79, 767-776.

[89] V. P. Nicu, E. J. Baerends, P. L. Polavarapu *J. Phys. Chem. A* **2012**, 116, 8366-8373.

[90] A. S. Perera, J. Cheramy, C. Merten, J. Thomas, Y. J. Xu *ChemPhysChem* **2018**, 19, 2234-2242.

[91] P. Wang, P. L. Polavarapu *J. Phys. Chem. A* **2000**, 104, 6189-6196.

[92] C. Cappelli *Int. J. Quantum Chem.* **2016**, 116, 1532-1542.

[93] T. Giovannini, M. Olszowka, C. Cappellit *J. Chem. Theory Comput.* **2016**, 12, 5483-5492.

[94] M. L. Sanchez, M. A. Aguilar, F. J. O. delValle *J. Comp. Chem.* **1997**, 18, 313-322.

[95] J. Tomasi, B. Mennucci, R. Cammi *Chem. Rev.* **2005**, 105, 2999-3093.

[96] K. M. Spencer, T. B. Freedman, L. A. Nafie *Chem. Phys. Lett.* **1988**, 149, 367-374.

[97] D. P. Che, L. Hecht, L. A. Nafie *Chem. Phys. Lett.* **1991**, 180, 182-190.

[98] L. A. Nafie, T. B. Freedman *Chem. Phys. Lett.* **1989**, 154, 260-266.

[99] G. S. Yu, L. A. Nafie *Chem. Phys. Lett.* **1994**, 222, 403-410.

[100] F. J. Zhu, N. W. Isaacs, L. Hecht, L. D. Barron *Structure* **2005**, 13, 1409-1419.

[101] L. Hecht, L. D. Barron *Appl. Spectrosc*. **1990**, 44, 483-491.

[102] L. Hecht, L. D. Barron, W. Hug *Chem. Phys. Lett.* **1989**, 158, 341-344.

[103] J. Hanzlikova, P. Praus, V. Baumruk *J. Mol. Struct*. **1999**, 481, 431-435.

[104] L. Hecht, L. D. Barron, E. W. Blanch, A. F. Bell, L. A. Day *J. Raman Spectrosc*. **1999**, 30, 815-825.

[105] L. Hecht, L. D. Barron, A. R. Gargaro, Z. Q. Wen, W. Hug *J. Raman Spectrosc*. **1992**, 23, 401-411.

[106] J. Kapitán, L. D. Barron, L. Hecht *J. Raman Spectrosc*. **2015**, 46, 392-399.

[107] S. Yamamoto, H. Watarai *J. Raman Spectrosc*. **2010**, 41, 1664-1669.

[108] W. Hug *Appl. Spectrosc.* **2003**, 57, 1-13.
[109] L. D. Barron *Biomed. Spectrosc. Imaging* **2015**, 4, 223-253.
[110] K. M. Spencer, R. B. Edmonds, R. D. Rauh, M. M. Carrabba *Anal. Chem.* **1994**, 66, 1269-1273.
[111] J. M. Batista, E. W. Blanch, V. D. Bolzani *Nat. Prod. Rep.* **2015**, 32, 1280-1302.
[112] P. L. Polavarapu *Molecules* **2016**, 21.
[113] K. van Dyke, C. van Dyke, K. Woodfork *Luminescence Biotechnology: Instruments and Applications, 1st Ed.*, CRC Press, Florida, USA, **2001**.
[114] F. S. Richardson, J. P. Riehl *Chem. Rev.* **1977**, 77, 773-792.
[115] G. Longhi, E. Castiglioni, J. Koshoubu, G. Mazzeo, S. Abbate *Chirality* **2016**, 28, 696-707.
[116] J. Autschbach *Chirality* **2009**, 21, 116-152.
[117] N. B. Chen, B. Yan *Molecules* **2018**, 23.
[118] S. Abbate, G. Longhi, F. Lebon, E. Castiglioni, S. Superchi, L. Pisani, F. Fontana, F. Torricelli, T. Caronna, C. Villani, R. Sabia, M. Tommasini, A. Lucotti, D. Mendola, A. Mele, D. A. Lightner *J. Phys. Chem. C* **2014**, 118, 1682-1695.
[119] G. Longhi, E. Castiglioni, C. Villani, R. Sabia, S. Menichetti, C. Viglianisi, F. Devlin, S. Abbate *J. Photochem. Photobiol. A* **2016**, 331, 138-145.
[120] E. M. Sanchez-Carnerero, A. R. Agarrabeitia, F. Moreno, B. L. Maroto, G. Muller, M. J. Ortiz, S. de la Moya *Chem. Eur. J.* **2015**, 21, 13488-13500.
[121] C. Citti, U. M. Battisti, G. Ciccarella, V. Maiorano, G. Gigli, S. Abbate, G. Mazzeo, E. Castiglioni, G. Longhi, G. Cannazza *J. Chromatogr. A* **2016**, 1467, 335-346.
[122] B. Doistau, J. R. Jimenez, C. Piguet *Front. Chem.* **2020**, 8.
[123] T. Y. Li, Y. M. Jing, X. Liu, Y. Zhao, L. Shi, Z. Y. Tang, Y. X. Zheng, J. L. Zuo *Sci. Rep.* **2015**, 5.
[124] T. R. Schulte, J. J. Holstein, L. Krause, R. Michel, D. Stalke, E. Sakuda, K. Umakoshi, G. Longhi, S. Abbate, G. H. Clever *J. Am. Chem. Soc.* **2017**, 139, 6863-6866.
[125] J. E. House *Inorganic Chemistry 3rd Edition*, Academic Press, USA, **2019**.
[126] G. Vicentini, L. B. Zinner, J. Zukerman-Schpector, K. Zinner *Coord. Chem. Rev.* **2000**, 196, 353-382.

[127] S. V. Eliseeva, J. C. G. Bunzli *Chem. Soc. Rev.* **2010**, 39, 189-227.
[128] J. C. G. Bunzli, C. Piguet *Chem. Soc. Rev.* **2005**, 34, 1048-1077.
[129] J. C. G. Bunzli, S. V. Eliseeva *Basics of Lanthanide Photophysics, Vol. 7*, Springer, Germany, **2010**.
[130] J. C. G. Bunzli *Eur. J. Inorg. Chem.* **2017**, 5058-5063.
[131] M. C. Heffern, L. M. Matosziuk, T. J. Meade *Chem. Rev.* **2014**, 114, 4496-4539.
[132] E. G. Moore, A. P. S. Samuel, K. N. Raymond *Acc. Chem. Res.* **2009**, 42, 542-552.
[133] J. E. Geusic, H. M. Marcos, L. G. Vanuitert *Appl. Phys. Lett.* **1964**, 4, 182.
[134] V. Balaram *Geosci. Front.* **2019**, 10, 1285-1303.
[135] J. L. Yuan, G. L. Wang *Trends Analyt. Chem.* **2006**, 25, 490-500.
[136] J. C. G. Bunzli *Chem. Rev.* **2010**, 110, 2729-2755.
[137] K. Staszak, K. Wieszczycka, V. Marturano, B. Tylkowski *Coord. Chem. Rev.* **2019**, 397, 76-90.
[138] H. Tsukube, S. Shinoda *Chem. Rev.* **2002**, 102, 2389-2403.
[139] R. Carr, N. H. Evans, D. Parker *Chem. Soc. Rev.* **2012**, 41, 7673-7686.
[140] G. Muller *Dalton Trans.* **2009**, 9692-9707.
[141] T. Wu, J. Kapitán, V. Mašek, P. Bouř *Angew. Chem. Int. Ed.* **2015**, 54, 14933-14936.
[142] T. Wu, J. Průša, J. Kessler, M. Dračinský, J. Valenta, P. Bouř *Anal. Chem.* **2016**, 88, 8878-8885.
[143] T. Wu, J. Kessler, J. Kaminský, P. Bouř *Chem. Asian J.* **2018**, 13, 3865-3870.
[144] T. Wu, P. Bouř, V. Andrushchenko *Sci. Rep.* **2019**, 9.
[145] M. Krupová, J. Kapitán, P. Bouř *ACS Omega* **2019**, 4, 1265-1271.
[146] T. Wu, J. Kessler, P. Bouř *Phys. Chem. Chem. Phys.* **2016**, 18, 23803-23811.
[147] J. L. Cruz, M. V. Andres, M. A. Hernandez *Appl. Opt.* **1996**, 35, 922-927.
[148] S. Mancuso, S. R. Spangler *Astrophys. J.* **2000**, 539, 480-491.
[149] D. Foster, F. S. Richardson *J. Less Common Met.* **1983**, 93, 236-236.
[150] S. Ghidinelli, S. Abbate, G. Mazzeo, L. Paoloni, E. Viola, C. Ercolani, M. P. Donzello, G. Longhi *Chirality* **2020**, 32, 808-816.
[151] T. Wu, J. Kapitán, V. Andrushchenko, P. Bouř *Anal. Chem.* **2017**, 89, 5043-5049.

[152] W. R. Mason *A Practical Guide to Magnetic Circular Dichroism Spectroscopy*, Wiley & Sons, Inc., New Jersey, USA, **2008**.
[153] P. J. Stephens *Ann. Rev. Phys. Chem.* **1974**, 25, 201-232.
[154] J. McMaster, V. S. Oganesyan *Curr. Opin. Struct. Biol.* **2010**, 20, 615-622.
[155] M. Seth, T. Ziegler *Adv. Inorg. Chem.* **2010**, 62, 41-109.
[156] H. Solheim, K. Ruud, S. Coriani, P. Norman *J. Chem. Phys.* **2008**, 128.
[157] K. M. Lee, K. Yabana, G. F. Bertsch *J. Chem. Phys.* **2011**, 134.
[158] S. C. Sun, R. A. Beck, D. Williams-Young, X. S. Li *J. Chem. Theory Comput.* **2019**, 15, 6824-6831.
[159] P. Štěpánek, P. Bouř *J. Comp. Chem.* **2013**, 34, 1531-1539.
[160] P. Štěpánek, P. Bouř *J. Comp. Chem.* **2015**, 36, 723-730.
[161] D. Ganyushin, F. Neese *J. Chem. Phys.* **2008**, 128.
[162] P. Bouř, J. Sopková, L. Bednárová, P. Maloň, T. A. Keiderling *J. Comp. Chem.* **1997**, 18, 646-659.
[163] C. Mensch, L. D. Barron, C. Johannessen *Phys. Chem. Chem. Phys.* **2016**, 18, 31757-31768.
[164] S. Luber *J. Chem. Theory Comput.* **2017**, 13, 1254-1262.
[165] A. Scherrer, F. Agostini, D. Sebastiani, E. K. U. Gross, R. Vuilleumier *J. Chem. Phys.* **2015**, 143.
[166] L. S. Lerman *Proc. Natl. Acad. Sci. USA*. **1971**, 68, 1886-1890.
[167] W. Dzwolak *Chirality* **2014**, 26, 580-587.
[168] S. L. Ma, X. L. Cao, M. Mak, A. Sadik, C. Walkner, T. B. Freedman, I. K. Lednev, R. K. Dukor, L. A. Nafie *J. Am. Chem. Soc.* **2007**, 129, 12364-12365.
[169] S. Jahnigen, A. Scherrer, R. Vuilleumier, D. Sebastiani *Angew. Chem. Int. Ed.* **2018**, 57, 13344-13348.
[170] D. Kurouski, J. D. Handen, R. K. Dukor, L. A. Nafie, I. K. Lednev *Chem. Commun.* **2015**, 51, 89-92.
[171] R. Berardozzi, E. Badetti, N. A. C. dos Santos, K. Wurst, G. Licini, G. Pescitelli, C. Zonta, L. Di Bari *Chem. Commun.* **2016**, 52, 8428-8431.
[172] S. Lo Piano, S. Di Pietro, L. Di Bari *Chem. Commun.* **2012**, 48, 11996-11998.
[173] P. Rizzo, E. Lepera, G. Guerra *Chem. Commun.* **2014**, 50, 8185-8188.
[174] E. Yashima, K. Maeda *Macromolecules* **2008**, 41, 3-12.
[175] J. Kessler, J. Kapitán, P. Bouř *J. Phys. Chem. Lett.* **2015**, 6, 3314-3319.

[176] S. Yamamoto, J. Kaminský, P. Bouř *Anal. Chem.* **2012**, 84, 2440-2451.
[177] K. J. Jalkanen, V. W. Jurgensen, A. Claussen, A. Rahim, G. M. Jensen, R. C. Wade, F. Nardi, C. Jung, I. M. Degtyarenko, R. M. Nieminen, F. Herrmann, M. Knapp-Mohammady, T. A. Niehaus, K. Frimand, S. Suhai *Int. J. Quantum Chem.* **2006**, 106, 1160-1198.
[178] C. Merten, H. G. Li, X. F. Lu, A. Hartwig, L. A. Nafie *J. Raman Spectrosc.* **2010**, 41, 1563-1565.
[179] C. Merten, H. G. Li, L. A. Nafie *J. Phys. Chem. A* **2012**, 116, 7329-7336.
[180] G. Zajac, A. Kaczor, S. Buda, J. Mlynarski, J. Frelek, J. C. Dobrowolski, M. Baranska *J. Phys. Chem. B* **2015**, 119, 12193-12201.
[181] M. Unno, T. Kikukawa, M. Kumauchi, N. Kamo *J. Phys. Chem. B* **2013**, 117, 1321-1325.
[182] P. Michal, R. Čelechovský, M. Dudka, J. Kapitán, M. Vůjtek, M. Berešová, J. Šebestík, K. Thangavel, P. Bouř *J. Phys. Chem. B* **2019**, 123, 2147-2156.
[183] F. Chiti, C. M. Dobson *Annu. Rev. Biochem.* **2006**, 75, 333-366.
[184] C. M. Dobson *Nature* **2003**, 426, 884-890.
[185] F. Chiti, C. M. Dobson *Ann. Rev. Biochem.* **2017**, 86, 27-68.
[186] S. T. Ferreira, M. N. N. Vieira, F. G. De Felice *IUBMB Life* **2007**, 59, 332-345.
[187] M. R. Chapman, L. S. Robinson, J. S. Pinkner, R. Roth, J. Heuser, M. Hammar, S. Normark, S. J. Hultgren *Science* **2002**, 295, 851-855.
[188] D. Claessen, R. Rink, W. de Jong, J. Siebring, P. de Vreugd, F. G. H. Boersma, L. Dijkhuizen, H. A. B. Wosten *Genes Dev.* **2003**, 17, 1714-1726.
[189] D. M. Fowler, A. V. Koulov, C. Alory-Jost, M. S. Marks, W. E. Balch, J. W. Kelly *PLOS Biol*. **2006**, 4, 100-107.
[190] D. Hamada, I. Yanagihara, K. Tsumoto *Trends Biotechnol.* **2004**, 22, 93-97.
[191] T. Scheibel, R. Parthasarathy, G. Sawicki, X. M. Lin, H. Jaeger, S. L. Lindquist *Proc. Natl. Acad. Sci. USA* **2003**, 100, 4527-4532.
[192] M. Sunde, L. C. Serpell, M. Bartlam, P. E. Fraser, M. B. Pepys, C. C. F. Blake *J. Mol. Biol.* **1997**, 273, 729-739.
[193] V. N. Uversky, J. Li, A. L. Fink *J. Biol. Chem.* **2001**, 276, 10737-10744.
[194] B. H. Toyama, J. S. Weissman *Ann. Rev. Biochem.* **2011**, 80, 557-585.
[195] S. K. Maji, L. Wang, J. Greenwald, R. Riek *FEBS Lett.* **2009**, 583, 2610-2617.

[196] S. Chimon, M. A. Shaibat, C. R. Jones, D. C. Calero, B. Aizezi, Y. Ishii *Nat. Struct. Mol. Biol.* **2007**, 14, 1157-1164.
[197] J. E. Gillam, C. E. MacPhee *J. Phys. Condens. Matter* **2013**, 25.
[198] T. Hard *J. Phys. Chem. Lett.* **2014**, 5, 607-614.
[199] J. D. Harper, P. T. Lansbury *Ann. Rev. Biochem.* **1997**, 66, 385-407.
[200] C. Soto, L. Anderes, S. Suardi, F. Cardone, J. Castilla, M. J. Frossard, S. Peano, P. Saa, L. Limido, M. Carbonatto, J. Ironside, J. M. Torres, M. Pocchiari, F. Tagliavini *FEBS Lett.* **2005**, 579, 638-642.
[201] C. Soto, G. P. Saborio, L. Anderes *Trends Neurosci.* **2002**, 25, 390-394.
[202] H. G. Li, L. A. Nafie *J. Raman Spectrosc.* **2012**, 43, 89-94.
[203] D. Kurouski, R. P. Van Duyne, I. K. Lednev *Analyst* **2015**, 140, 4967-4980.
[204] M. Biancalana, S. Koide *Biochim. Biophys. Acta Proteins Proteom.* **2010**, 1804, 1405-1412.
[205] M. Lindgren, K. Sorgjerd, P. Hammarstrom *Biophys. J.* **2005**, 88, 4200-4212.
[206] M. Groenning *J. Chem. Biol.* **2010**, 3, 1-18.
[207] S. Ma, X. Cao, M. Mak, A. Sadik, C. Walkner, T. B. Freedman, I. K. Lednev, R. K. Dukor, L. A. Nafie *J. Am. Chem. Soc.* **2007**, 129, 12364-12365.
[208] D. Kurouski, R. K. Dukor, X. F. Lu, L. A. Nafie, I. K. Lednev *Chem. Commun.* **2012**, 48, 2837-2839.
[209] D. Kurouski, R. A. Lombardi, R. K. Dukor, I. K. Lednev, L. A. Nafie *Chem. Commun.* **2010**, 46, 7154-7156.
[210] D. Kurouski, X. F. Lu, L. Popova, W. Wan, M. Shanmugasundaram, G. Stubbs, R. K. Dukor, I. K. Lednev, L. A. Nafie *J. Am. Chem. Soc.* **2014**, 136, 2302-2312.
[211] H. Sato *Phys. Chem. Chem. Phys.* **2020**, 22, 7671-7679.
[212] R. K. Dukor, T. A. Keiderling *Biopolymers* **1991**, 31, 1747-1761.
[213] J. Kessler, T. A. Keiderling, P. Bouř *J. Phys. Chem. B* **2014**, 118, 6937-6945.
[214] T. J. Measey, R. Schweitzer-Stenner *J. Am. Chem. Soc.* **2011**, 133, 1066-1076.
[215] R. Schweitzer-Stenner *J. Phys. Chem. B* **2012**, 116, 4141-4153.
[216] A. Fulara, A. Lakhani, S. Wojcik, H. Nieznanska, T. A. Keiderling, W. Dzwolak *J. Phys. Chem. B* **2011**, 115, 11010-11016.
[217] R. Vijay, P. L. Polavarapu *J. Phys. Chem. A* **2013**, 117, 14086-14094.
[218] J. Průša, P. Bouř *Chirality* **2018**, 30, 55-64.

[219] H. Chi, W. R. W. Welch, J. Kubelka, T. A. Keiderling *Biomacromolecules* **2013**, 14, 3880-3891.
[220] J. Kessler, V. Andrushchenko, J. Kapitán, P. Bouř *Phys. Chem. Chem. Phys.* **2018**, 20, 4926-4935.
[221] W. R. W. Welch, J. Kubelka, T. A. Keiderling *J. Phys. Chem. B* **2013**, 117, 10343-10358.
[222] J. Kubelka, J. Kim, P. Bouř, T. A. Keiderling *Vib. Spectrosc.* **2006**, 42, 63-73.
[223] K. Itoh, B. M. Foxman, G. D. Fasman *Biopolymers* **1976**, 15, 419-455.
[224] H. D. Keith, G. Giannoni, F. J. Padden *Biopolymers* **1969**, 7, 775-792.
[225] K. Binnemans *Coord. Chem. Rev.* **2015**, 295, 1-45.
[226] P. Job *Ann. Chim. Appl.* **1928**, 9, 113-203.
[227] M. H. M. Olsson, C. R. Sondergaard, M. Rostkowski, J. H. Jensen *J. Chem. Theory Comput.* **2011**, 7, 525-537.
[228] C. R. Sondergaard, M. H. M. Olsson, M. Rostkowski, J. H. Jensen *J. Chem. Theory Comput.* **2011**, 7, 2284-2295.
[229] W. Im, D. Beglov, B. Roux *Comp. Phys. Commun.* **1998**, 111, 59-75.
[230] S. Jo, T. Kim, V. G. Iyer, W. Im *J. Comput. Chem.* **2008**, 29, 1895-1865.
[231] S. Jo, M. Vargyas, J. Vasko-Szedlar, B. Roux, W. Im *Nucleic Acids Res.* **2008**, 36, 270-275.
[232] K. Annamalai, K. H. Guehrs, R. Koehler, M. Schmidt, H. Michel, C. Loos, P. M. Gaffney, C. J. Sigurdson, U. Hegenbart, S. Schoenland, M. Fandrich *Angew. Chem. Int. Ed.* **2016**, 55, 4822-4825.
[233] J. Madine, E. Jack, P. G. Stockley, S. E. Radford, L. C. Serpell, D. A. Middleton *J. Am. Chem. Soc.* **2008**, 130, 14990-15001.
[234] A. Sakalauskas, M. Ziaunys, V. Smirnovas *PEERJ* **2019**, 7.
[235] N. G. N. Milton, J. R. Harris *Micron* **2009**, 40, 800-810.
[236] M. Stefani *Curr. Protein Pept. Sci.* **2010**, 11, 343-354.
[237] V. Smirnovas, T. Sneideris, K. Milto *Prion* **2016**, 10, S49-S49.
[238] W. Surmacz-Chwedoruk, H. Nieznanska, S. Wojcik, W. Dzwolak *Biochemistry* **2012**, 51, 9460-9469.
[239] M. Fandrich, S. Nystrom, K. P. R. Nilsson, A. Bockmann, H. LeVine, P. Hammarstrom *J. Intern. Med.* **2018**, 283, 218-237.
[240] R. Tycko *Neuron* **2015**, 86, 632-645.

[241] L. A. Nafie *Chirality* **2020**, 32, 667-692.
[242] V. Declerck, A. Perez-Mellor, R. Guillot, D. J. Aitken, M. Mons, A. Zehnacker *Chirality* **2019**, 31, 547-560.
[243] H. Sato, I. Kawamura *Biochim. and Biophys. Acta* **2020**, 1868.
[244] I. Kawamura, H. Sato *Anal. Biochem.* **2019**, 580, 14-20.
[245] G. Shanmugam, P. L. Polavarapu *Chirality* **2009**, 21, 152-159.
[246] T. A. Keiderling *Chem. Rev.* **2020**, 120, 3381-3419.
[247] G. Shanmugam, P. L. Polavarapu *J. Am. Chem. Soc.* **2004**, 126, 10292-10295.
[248] A. C. Sen, T. A. Keiderling *Biopolymers* **1984**, 23, 1533-1545.
[249] A. G. Petrovic, P. K. Bose, P. L. Polavarapu *Carb. Res.* **2004**, 339, 2713-2720.
[250] C. Merten, A. Hartwig *Macromolecules* **2010**, 43, 8373-8378.
[251] C. Merten, T. Kowalik, A. Hartwig *Appl. Spectrosc.* **2008**, 62, 901-905.
[252] M. M. Quesada-Moreno, J. R. Aviles-Moreno, J. J. Lopez-Gonzalez, R. M. Claramunt, C. Lopez, I. Alkorta, J. Elguero *Tetrahedron Asymmetry* **2014**, 25, 507-515.
[253] M. M. Quesada-Moreno, A. Virgili, E. Monteagudo, R. M. Claramunt, J. R. Aviles-Moreno, J. J. Lopez-Gonzalez, I. Alkorta, J. Elguero *Analyst* **2018**, 143, 1406-1416.
[254] T. Sakai, Y. Akagi, H. Suzuki, M. Irie, T. Nakamura, H. Sato, I. Kawamura *Anal. Sci.* **2020**, 36, 1337-1343.
[255] H. Sato, K. Tamura, K. Takimoto, A. Yamagishi *Phys. Chem. Chem. Phys.* **2018**, 20, 3141-3147.
[256] I. Dolamic, B. Varnholt, T. Burgi *Nat. Commun.* **2015**, 6.
[257] C. Gautier, T. Burgi *J. Phys. Chem. C* **2010**, 114, 15897-15902.
[258] E. Castiglioni, P. Biscarini, S. Abbate *Chirality* **2009**, 21, E28-E36.
[259] W. Kaminsky, K. Claborn, B. Kahr *Chem. Soc. Rev.* **2004**, 33, 514-525.
[260] T. Buffeteau, F. S. Lagugne-Labarthet, C. Sourisseau *Appl. Spectrosc.* **2005**, 59, 732-745.
[261] L. A. Nafie *Appl. Spectrosc.* **2000**, 54, 1634-1645.
[262] X. L. Cao, R. K. Dukor, L. A. Nafie *Theor. Chem. Acc.* **2008**, 119, 69-79.
[263] H. D. Flack *Helv. Chim. Acta* **2003**, 86, 905-921.
[264] C. Dryzun, D. Avnir *Chem. Commun.* **2012**, 48, 5874-5876.

[265] A. G. Shtukenberg, Y. O. Punin, A. Gujral, B. Kahr *Angew. Chem. Int. Ed.* **2014**, 53, 672-699.
[266] W. I. F. David, K. Shankland, C. R. Pulham, N. Blagden, R. J. Davey, M. Song *Angew. Chem. Int. Ed.* **2005**, 44, 7032-7035.
[267] J. Tao, K. J. Jones, L. Yu *Cryst. Growth Des.* **2007**, 7, 2410-2414.
[268] L. Yu *Crystengcomm*. **2007**, 9, 847-851.
[269] J. J. L. Gonzalez, F. P. Urena, J. R. A. Moreno, I. Mata, E. Molins, R. M. Claramunt, C. Lopez, I. Alkorta, J. Elguero *New J. Chem.* **2012**, 36, 749-758.
[270] G. Q. Niu, Z. L. Li, P. J. Huang, H. R. Tan *J. Antibiot.* **2019**, 72, 906-912.
[271] H. Osada *J. Antibiot.* **2019**, 72, 855-864.
[272] T. Shiraishi, T. Kuzuyama *J. Antibiot.* **2019**, 72, 913-923.
[273] E. De Clercq *Nat. Rev. Drug Discov.* **2002**, 1, 13-25.
[274] E. De Clercq, A. Holý *Nat. Rev. Drug Discov.* **2005**, 4, 928-940.
[275] V. Vivet-Boudou, J. Didierjean, C. Isel, R. Marquet *Cell. Mol. Life Sci.* **2006**, 63, 163-186.
[276] P. L. Bonate, L. Arthaud, W. R. Cantrell, K. Stephenson, J. A. Secrist, S. Weitman *Nat. Rev. Drug Discov.* **2006**, 5, 855-U852.
[277] C. M. Galmarini, J. R. Mackey, C. Dumontet *Lancet Oncol.* **2002**, 3, 415-424.
[278] M. Guinan, C. Benckendorff, M. Smith, G. J. Miller *Molecules* **2020**, 25.
[279] J. Shelton, X. Lu, J. A. Hollenbaugh, J. H. Cho, F. Amblard, R. F. Schinazi *Chem. Rev.* **2016**, 116, 14379-14455.
[280] D. S. Wishart, Y. D. Feunang, A. Marcu, A. C. Guo, K. Liang, R. Vazquez-Fresno, T. Sajed, D. Johnson, C. R. Li, N. Karu, Z. Sayeeda, E. Lo, N. Assempour, M. Berjanskii, S. Singhal, D. Arndt, Y. J. Liang, H. Badran, J. Grant, A. Serra-Cayuela, Y. F. Liu, R. Mandal, V. Neveu, A. Pon, C. Knox, M. Wilson, C. Manach, A. Scalbert *Nucleic Acids Res.* **2018**, 46, 608-617.
[281] S. Kim, J. Chen, T. J. Cheng, A. Gindulyte, J. He, S. Q. He, Q. L. Li, B. A. Shoemaker, P. A. Thiessen, B. Yu, L. Zaslavsky, J. Zhang, E. E. Bolton *Nucleic Acids Res.* **2021**, 49, 1388-1395.
[282] H. E. Pence, A. Williams *J. Chem. Educ.* **2010**, 87, 1123-1124.
[283] A. X. Chen, S. W. Zito, R. A. Nash *Pharm. Res.* **1994**, 11, 398-401.
[284] S. Mohandoss, R. Atchudan, T. N. J. I. Edison, T. K. Mandal, S. Palanisamy, S. You, A. A. Napoleon, J. J. Shim, Y. R. Lee *Carbohydr. Polym.* **2019**, 224.

[285] T. Bhattacharyya, P. Saha, J. Dash *ACS Omega* **2018**, 3, 2230-2241.

[286] G. Gottarelli, G. P. Spada *Chem. Rec.* **2004**, 4, 39-49.

[287] J. T. Davis, G. P. Spada *Chem. Soc. Rev.* **2007**, 36, 296-313.

[288] E. Mezzina, P. Mariani, R. Itri, S. Masiero, S. Pieraccini, G. P. Spada, F. Spinozzi, J. T. Davis, G. Gottarelli *Chem. Eur. J.* **2001**, 7, 388-395.

[289] T. Simonsson *Biol. Chem.* **2001**, 382, 621-628.

[290] J. K. Bai, X. L. Sun, H. S. Wang, C. Li, R. Z. Qiao *J. Org. Chem.* **2020**, 85, 2010-2018.

[291] B. Gatto, M. Palumbo, C. Sissi *Curr. Med. Chem.* **2009**, 16, 1248-1265.

[292] B. R. Wood *Chem. Soc. Rev.* **2016**, 45, 1980-1998.

[293] B. Jayaram, T. Jain *Annu. Rev. Biophys.* **2004**, 33, 343-361.

[294] C. K. Reddy, A. Das, B. Jayaram *J. Mol. Biol.* **2001**, 314, 619-632.

[295] V. Patel, O. P. Sharma, T. Mehta *Expert Opin. Drug Deliv.* **2018**, 15, 351-368.

[296] F. H. Chen, Y. N. Liu, Y. X. Wang, Y. R. Ma, L. M. Qi *Cryst. Growth Des.* **2020**, 20, 2275-2282.

[297] Y. Sugawara, Y. Iimura, H. Iwasaki, H. Urabe, H. Saito *J. Biomol. Struct. Dyn.* **1994**, 11, 721-729.

[298] H. Urabe, Y. Sugawara, T. Kasuya *Phys. Rev. B* **1995**, 51, 5666-5672.

[299] U. Thewalt, C. E. Bugg, R. E. Marsh *Acta Crystal.* **1970**, B26, 1089-1101.

[300] T. F. Lai, R. E. Marsh *Acta Cryst.* **1972**, B28, 1982-1989.

[301] M. Banyay, M. Sarkar, A. Graslund *Biophys. Chem.* **2003**, 104, 477-488.

[302] Y. F. Liu, Y. G. Yang, K. Jiang, D. H. Shi, J. F. Sun *Chem. Phys. Lett.* **2012**, 528, 53-58.

[303] H. Dong, S. R. Du, X. Y. Zheng, G. M. Lyu, L. D. Sun, L. D. Li, P. Z. Zhang, C. Zhang, C. H. Yan *Chem. Rev.* **2015**, 115, 10725-10815.

[304] N. Ishikawa *Polyhedron* **2007**, 26, 2147-2153.

[305] B. M. van der Ende, L. Aarts, A. Meijerink *Phys. Chem. Chem. Phys.* **2009**, 11, 11081-11095.

[306] J. Becquerel *Z. Physik* **1929**, 58, 205-216.

[307] H. Bethe *Ann. Physik* **1928**, 392, 55-129.

[308] J. van Vleck *Phys. Rev.* **1932**, 41, 208-215.

[309] J. D. Rinehart, J. R. Long *Chem. Sci.* **2011**, 2, 2078-2085.

[310] S. Hamad, N. C. Hernandez, A. Aziz, A. R. Ruiz-Salvador, S. Calero, R. Grau-Crespo *J. Mater. Chem. A* **2015**, 3, 23458-23465.
[311] S. T. Liddle *Angew. Chem. Int. Ed.* **2015**, 54, 8604-8641.
[312] P. Dorenbos *ECS J. Solid State Sci. Technol.* **2013**, 2, R3001-R3011.
[313] B. R. Judd *Phys. Rev.* **1962**, 127, 750-&.
[314] G. S. Ofelt *J. Chem. Phys.* **1962**, 37, 511-&.
[315] F. S. Richardson, T. R. Faulkner *J. Chem. Phys.* **1982**, 76, 1595-1606.
[316] B. M. Walsh *Judd-Ofelt theory: Principles and practices, Vol. 231*, Springer, Netherlands, **2006**.
[317] C. Gorller-Walrand, K. Binnemans *Rationalization of Crystal-Field Parametrization, Vol. 23*, Elsevier, Amsterdam, Netherlands, **1996**.
[318] P. P. Hallmen, G. Rauhut, H. Stoll, A. O. Mitrushchenkov, J. van Slageren *J. Chem. Theory Comput.* **2018**, 14, 3998-4009.
[319] J. Jung, M. A. Islam, V. L. Pecoraro, T. Mallah, C. Berthon, H. Bolvin *Chem. Eur. J.* **2019**, 25, 15112-15122.
[320] L. Ungur, L. F. Chibotaru *Chem. Eur. J.* **2017**, 23, 3708-3718.
[321] K. Andersson, P. A. Malmqvist, B. O. Roos *J. Chem. Phys.* **1992**, 96, 1218-1226.
[322] J. Finley, P. A. Malmqvist, B. O. Roos, L. Serrano-Andres *Chem. Phys. Lett.* **1998**, 288, 299-306.
[323] K. Andersson, P. A. Malmqvist, B. O. Roos, A. J. Sadlej, K. Wolinski *J. Phys. Chem.* **1990**, 94, 5483-5488.
[324] K. Ruedenberg, M. W. Schmidt, M. M. Gilbert *Chem. Phys.* **1982**, 71, 51-64.
[325] B. O. Roos *Adv. Chem. Phys.* **1987**, 69, 399-445.
[326] RCSB PDB. 2HUB pH 7.5
[327] H. J. Werner, P. J. Knowles, G. Knizia, F. R. Manby, M. Schutz *Wiley Interdiscip. Rev. Comput. Mol. Sci.* **2012**, 2, 242-253.
[328] B. O. Roos, P. R. Taylor, P. E. M. Siegbahn *Chem. Phys.* **1980**, 48, 157-173.
[329] P. Pulay *Int. J. Quantum Chem.* **2011**, 111, 3273-3279.
[330] B. O. Roos, K. Andersson, M. P. Fulscher, P. A. Malmqvist, L. SerranoAndres, K. Pierloot, M. Merchan *Adv. Chem. Phys.* **1996**, 93, 219-331.
[331] P. A. Malmqvist, A. Rendell, B. O. Roos *J. Phys. Chem.* **1990**, 94, 5477-5482.

[332] J. Wen, T. Uto, J. Chalupský, D. L. Casher, G. Raabe, J. Fleischhauer, T. Yanai, H. Tsuji, K. Komatsu, J. Michl *J. Phys. Org. Chem.* **2018**, 31.
[333] D. A. Case, T. E. Cheatham, T. Darden, H. Gohlke, R. Luo, K. M. Merz, A. Onufriev, C. Simmerling, B. Wang, R. J. Woods *J. Comp. Chem.* **2005**, 26, 1668-1688.
[334] D. A. Case, T. A. Darden, T. E. Cheatham, C. L. Simmerling, J. Wang, R. E. Duke, R. Luo, M. Crowley, R. C. Walker, W. Zhang, K. M. Merz, B. Wang, S. Hayik, A. Roitberg, G. Seabra, I. Kolossváry, K. F. Wong, F. Paesani, J. Vanicek, X. Wu, S. R. Brozell, T. Steinbrecher, H. Gohlke, L. Yang, C. Tan, J. Mongan, V. Hornak, G. Cui, D. H. Mathews, M. G. Seetin, C. Sagui, V. Babin, P. A. Kollman *AMBER 10*, University of California, San Francisco, USA, **2008**.
[335] M. J. Frisch, G. W. Trucks, H. B. Schlegel, G. E. Scuseria, M. A. Robb, J. R. Cheeseman, G. Scalmani, V. Barone, G. A. Petersson, H. Nakatsuji, X. Li, M. Caricato, A. Marenich, J. Bloino, B. G. Janesko, R. Gomperts, B. Mennucci, H. P. Hratchian, J. V. Ortiz, A. F. Izmaylov, J. L. Sonnenberg, D. Williams-Young, F. Ding, F. Lipparini, F. Egidi, J. Goings, B. Peng, A. Petrone, T. Henderson, D. Ranasinghe, V. G. Zakrzewski, J. Gao, N. Rega, G. Zheng, W. Liang, M. Hada, M. Ehara, M. Toyota, R. Fukuda, J. Hasegawa, M. Ishida, T. Nakajima, Y. Honda, O. Kitao, H. Nakai, T. Vreven, K. Throssell, J. A. Montgomery, J. E. Peralta, F. Ogliaro, M. Bearpark, J. J. Heyd, E. Brothers, K. N. Kudin, V. N. Staroverov, T. Keith, R. Kobayashi, J. Normand, K. Raghavachari, A. Rendell, J. C. Burant, S. S. Iyengar, J. Tomasi, M. Cossi, J. M. Millam, M. Klene, C. Adamo, R. Cammi, J. W. Ochterski, R. L. Martin, K. Morokuma, O. Farkas, J. B. Foresman, D. J. Fox *Gaussian 09, Revision D01*, Gaussian, Inc., **2016**.
[336] A. D. Becke *J. Chem. Phys.* **1993**, 98, 1372-1377.
[337] P. J. Stephens, F. J. Devlin, C. F. Chabalowski, M. J. Frisch *J. Phys. Chem.* **1994**, 98, 11623-11627.
[338] D. Figgen, G. Rauhut, M. Dolg, H. Stoll *Chem. Phys.* **2005**, 311, 227-244.
[339] L. Troxler, M. Baaden, V. Bohmer, G. Wipff *Supramol. Chem.* **2000**, 12, 27-+.
[340] F. C. J. M. van Veggel, D. N. Reinhoudt *Chem. Eur. J.* **1999**, 5, 90-95.
[341] F. Yerly, K. I. Hardcastle, L. Helm, S. Aime, M. Botta, A. E. Merbach *Chem. Eur. J.* **2002**, 8, 1031-1039.
[342] S. Edvardsson, D. Aberg *Comput. Phys. Commun.* **2001**, 133, 396-406.

[343] W. T. Carnall, G. L. Goodman, K. Rajnak, R. S. Rana *J. Chem. Phys.* **1989**, 90, 3443-3457.
[344] B. R. Judd *Phys. Rev.* **1962**, 127, 750-761.
[345] B. O. Roos, R. Lindh, P. A. Malmqvist, V. Veryazov, P. O. Widmark *J. Phys. Chem. A* **2004**, 108, 2851-2858.
[346] B. O. Roos, R. Lindh, P. A. Malmqvist, V. Veryazov, P. O. Widmark, A. C. Borin *J. Phys. Chem. A* **2008**, 112, 11431-11435.
[347] P. O. Widmark, P. A. Malmqvist, B. O. Roos *Theor. Chim. Acta* **1990**, 77, 291-306.
[348] G. Ghigo, B. O. Roos, P. A. Malmqvist *Chem. Phys. Lett.* **2004**, 396, 142-149.
[349] N. Forsberg, P. A. Malmqvist *Chem. Phys. Lett.* **1997**, 274, 196-204.
[350] M. Douglas, N. M. Kroll *Ann. Phys.* **1974**, 82, 89-155.
[351] B. A. Hess *Phys. Rev. A* **1986**, 33, 3742-3748.
[352] G. Jansen, B. A. Hess *Phys. Rev. A* **1989**, 39, 6016-6017.
[353] B. Sandhoefer, F. Neese *J. Chem. Phys.* **2012**, 137.
[354] T. N. Lan, J. Chalupský, T. Yanai *Mol. Phys.* **2015**, 113, 1750-1767.
[355] J. Chalupský, T. Yanai *J. Chem. Phys.* **2013**, 139.
[356] P. A. Malmqvist, B. O. Roos, B. Schimmelpfennig *Chem. Phys. Lett.* **2002**, 357, 230-240.
[357] S. Hussain, X. N. Chen, W. T. A. Harrison, M. R. J. Elsegoods, S. Ahmad, S. J. Li, S. Muhammad, D. Awoyelu *Front. Chem.* **2019**, 7.
[358] K. Binnemans, K. VanHerck, C. GorllerWalrand *Chem. Phys. Lett.* **1997**, 266, 297-302.
[359] V. Andrushchenko, D. Padula, E. Zhivotova, S. Yamamoto, P. Bouř *Chirality* **2014**, 26, 655-662.
[360] E. I. Solomon, K. M. Light, L. V. Liu, M. Srnec, S. D. Wong *Acc. Chem. Res.* **2013**, 46, 2725-2739.
[361] T. Fujii, A. Uehara, T. Nagai, H. Yamana *Z. Naturforsch. A* **2007**, 62, 733-738.
[362] E. Ceci-Ginistrelli, C. Smith, D. Pugliese, J. Lousteau, N. G. Boetti, W. A. Clarkson, F. Poletti, D. Milanese *J. Alloys Compd.* **2017**, 722, 599-605.
[363] F. Ramos-Lara, A. Lira, M. O Ramirez, M. Flores, R. Arroyo, U. Caldino *J. Phys. Condens. Matter*. **2006**, 18, 7951-7959.
[364] L. Lepine, R. Gilbert, G. Belanger *Anal. Chem.* **1986**, 58, 1152-1156.

List of Figures

List of Tables

Abbreviations

A ..... adenosine

a.u. ..... atomic units

AFM ..... atomic force microscopy

BO ..... Born-Oppenheimer

CAS ..... complete active space

CASPT2 ..... complete active space with second order perturbation theory

CB ..... circular birefringence

CCT ..... Cartesian coordinate transfer

CD ..... circular dichroism

CFT ..... crystal field theory

CI ..... configuration interaction

CPL ..... circularly polarized luminescence

DCP ..... dual circular polarization

DFT ..... density functional theory

dG ..... 2'-deoxyguanosine

DKH ..... Douglas-Kroll-Hess Hamiltonian

DPA ..... pyridine-2,6-dicarboxylic acid

ECD ..... electronic circular dichroism

ECP ..... effective core potential

G ..... guanosine

HEWL ..... hen egg-white lysozyme

HWHM ..... half-width at half-maximum

ICP ..... incident circular polarization

INS ..... insulin

LB ..... linear birefringence

LD ..... linear dichroism

Ln ..... lanthanide

MCD ..... magnetic circular dichroism

MD ..... molecular dynamics

MO ..... molecular orbitals

MS-CASPT2 ..... multi-state CASPT2

NMR ..... nuclear magnetic resonance spectroscopy

ORD ..... optical rotatory dispersion

PDGA ..... *D*-enantiomer of polyglutamic acid

PGA ..... polyglutamic acid

PLGA ..... *L*-enantiomer of polyglutamic acid

PT ..... perturbation theory

RAS ..... restricted active space

RMSD ..... root-mean-square deviation

ROA ..... Raman optical activity

SCF ..... self-consistent field

SCP ..... scattered circular polarization

SD-VCD ..... solid-state vibrational circular dichroism

SOC ..... spin-orbit coupling

SSC ..... spin-spin coupling

TDC ..... transition dipole coupling

TEM ..... transmission electron microscopy

TGA ..... thermogravimetric analysis

ThT ……...……. Thioflavin-T

TL ……... total luminescence

UV ……... ultraviolet

VCD …...……... vibrational circular dichroism

VOA ……..…….. vibrational optical activity

List of Publications

This thesis is based on three published articles **I – III** and two manuscripts in preparation. I presented my work at 9 international conferences and workshops, giving 4 poster presentations and 5 talks.

[I]. Krupová, M.; Kessler, J.; Bouř, P.: Recent Trends in Chiroptical Spectroscopy: Theory and Application of Vibrational Circular Dichroism and Raman Optical Activity. *ChemPlusChem* **2020**, 85(3), 561-575

DOI: 10.1002/cplu.202000014, **IF:** 2.753, Cited 7×

My contribution: Preparation of the VCD part of the manuscript.

[II]. Krupová, M.; Kapitán, J.; Bouř, P.: Induced Lanthanide Circularly Polarized Luminescence as a Probe of Protein Fibrils. *ACS Omega* **2019**, 4(1), 1265-1271

DOI: 10.1021/acsomega.8b03175, **IF:** 2.87, Cited 4×

My contribution: Preparation of amyloid fibrils and all VCD, CPL and fluorescence experiments. Analysis of the results and partial preparation of the manuscript.

[III]. Krupová, M.; Kessler, J.; Bouř, P.: Polymorphism of Amyloid Fibrils Induced by Catalytic Seeding: A Vibrational Circular Dichroism Study. *ChemPhysChem* **2021**, 22(1), 83-91

DOI: 10.1002/cphc.202000797, **IF:** 3.144

My contribution: Preparation of amyloid fibrils, all VCD spectra experiments. Major contribution to the analysis of the results and partial preparation of the manuscript.

[IV]. Krupová, M. *et al.*: Vibrational Circular Dichroism Unravels Supramolecular Chirality and Hydration Polymorphism of Nucleoside Crystals. **2021**, manuscript in preparation.

My contribution: Partial preparation of nucleoside suspensions and measurement of some VCD spectra, analysis and discussion of the results and partial preparation of the manuscript.

[V]. Krupová, M. *et al.*: Towards Interpretation of Lanthanide Optical Spectra: MS-CASPT2 Relativistic Interpretation of Magnetic Circular Dichroism. **2021**, manuscript in preparation.

My contribution: Molecular dynamics simulations of Ln^{3+}/H_2O cluster geometries and all Gaussian and CFT calculations. Analysis and discussion of the results and partial preparation of the manuscript.